Ground State of Fermions in Quasi-1D Honeycomb Optical Lattices

Daniel Camilo Padilla González

Universidad Nacional de Colombia
Facultad de Ciencias
Departamento de Física
Bogotá, D.C.
Mayo de 2022

Ground State of Fermions in Quasi-1D Honeycomb Optical Lattices

Daniel Camilo Padilla González

Trabajo final de grado presentado como requisito parcial para optar al título de
Magister en Ciencias Física

Advisor
Jereson Silva Valencia, Ph.D.
Doctor en Física

Research line
Condensed Matter

Research group
Grupo de Sistemas Correlacionados SISCO

Universidad Nacional de Colombia
Facultad de Ciencias
Departamento de Física
Bogotá, D.C.
Mayo de 2022

Title in English

Ground State of Fermions in Quasi-1D Honeycomb Optical Lattices

Título en español

Estado Base de Fermiones en Redes Ópticas Cuasi-1D Tipo Panal

Abstract: Lattice models (tight-binding) for many-body systems give a good theoretical and experimental framework to study quantum phase transitions presented in several strongly correlated materials at low temperature. In general, those phase transitions are driven by a fine-tuning of non-thermal parameters such that each phase is determined by a fixed energy scale. In particular, the *Ionic Hubbard model* allows to study crystalline bipartite lattices where the possible phase transitions are induced by a competition between the on-site interaction U and the geometry of the lattice itself given by the staggered potential Δ. Furthermore, recent experimental and theoretical works on honeycomb lattice connect the model with phenomenon like unconventional superconductivity [Journal of the Physical Society of Japan 82 (2013) 034704] and topological correlated systems [PhysicaB 481 (2016) 53-58]. Motivated by this, we study the ground-state properties of the Ionic Hubbard model in two scenarios: a narrow honeycomb lattice regarding it as a quasi 1D lattice and a mass-imbalanced chain. To explore those systems, we use a density renormalization group (DMRG) finite algorithm with a matrix product state (MPS) method.

Resumen: Los modelos de redes (tight-binding) para sistemas de muchos cuerpos dan un buen marco teórico y experimental para estudiar transiciones de fases cuánticas presentes en diversos materiales fuertemente correlacionados a bajas temperaturas. En general, estas transiciones de fases pueden ocurrir debido a un ajuste fino de parámetros no térmicos tal que cada fase se determina por una escala fija de energía. En particular, el modelo *Iónico de Hubbard* permite estudiar una red cristalina bipartita donde dos fases son inducidas debido a la competencia entre la interacción local U y la geometría de la red misma dada por el potencial escalonado Δ. Además, trabajos experimentales y teóricos recientes sobre redes de tipo panal relacionan el modelo con fenómenos como superconductividad no convencional [Journal of the Physical Society of Japan 82 (2013) 034704] y sistemas topológicos correlacionados [PhysicaB 481 (2016) 53-58]. Motivados por esto, nosotros estudiamos las propiedades del estado base del modelo Iónico de Hubbard en dos escenarios: una red delgada tipo panal, estudiada a través de un mapeo cuasi 1D, y una cadena con imbalance de masas. Para explorar estos sistemas, usamos un algoritmo finito del grupo de renormalización de la matriz densidad (DMRG) y un método de producto de estados de matrices (MPS).

Keywords: Honeycomb lattice, Ionic Hubbard model, DMRG algorithml, Phase transitions

Palabras clave: Red tipo panal, modelo Iónico de Hubbard, algoritmo DMRG, Transición de fase.

Dedicated to

All people in my daily life who give me force to go on with my dreams. I'm really grateful with you. THANKS YOU!!

Contents

Contents **II**

List of Tables **IV**

List of Figures **V**

Introduction **X**

1. Hubbard Model **1**

1.1 Fermi-Hubbard model 1

1.2 Optical lattices and superfluid-insulator transition 6

1.3 Experimental realization of The Fermi-Hubbard model in optical lattices . . 10

1.4 Hubbard model in a honeycomb lattice 13

1.5 Mass-imbalanced Hubbard model 17

2. Ionic Hubbard Model **19**

2.1 Origins of Ionic Hubbard Model (IHM) 19

2.2 One-dimensional IHM 22

2.3 Two-dimensional IHM and Optical Lattices 25

2.4 IHM with Mass-imbalance 27

2.5 A DMRG Study: IHM for Narrow Honeycomb Lattice and Mass-imbalance Chain 29

2.5.1 Narrow honeycomb lattice $L_y = 2$ 31

2.5.2 Narrow honeycomb lattice $L_y = 4$ 39

2.5.3 Mass-imbalanced chain 42

Conclusions **48**

Some Notes about the DMRG algorithm for two dimensional systems **50**

Bibliography **54**

List of Tables

1.1 Overall MI transitions observed in various compounds. Adapted from [IFT98] 6

List of Figures

1.1 Sketch of MI transition in the plane n-U/t. The transition can occur by two ways: the filling-control metal-insulator transition (FC-MIT) and the bandwidth-control metal-insulator transition (BC-MIT). From [IFT98] 4

1.2 Optical lattice potential (for $z = 0$) produced by the interference between counter-propagating laser. (**a**) One dimensional lattice in y-direction given by (1.3), (**b**) Two dimensional lattice in the xy-plane given by (1.4). 7

1.3 Absorption image of the lattice after of a time-flight of 15 ms. The lattice potential depth is measured in units of the *recoil energy* $E_r = 2\pi^2\hbar^2/m\lambda^2$, being λ the wave-length of the lattice. The values of V_0 are: (**a**) 0, (**b**) $3E_r$, (**c**) $7E_r$, (**d**) $10E_r$, (**e**) $13E_r$, (**f**) $14E_r$, (**g**) $16E_r$, (**h**) $22E_r$. From [Gre02]. . 10

1.4 Elastic scattering cross-section of the collision between atoms of ^{40}K in $|9/2, -9/2\rangle$ and $|9/2, -7/2\rangle$ states loaded in an optical lattice as a function of the magnitude of an external uniform magnetic field. From [LRT$^+$02]. . . 10

1.5 Sketch of metallic and insulator phases near to MI transition: (**a**) Metallic phase where the particles are not localized moving between the lattice sites, (**b**) Mott-insulator phase where the particles are localized and an antiferromagnetic order is observed. The red and blue spheres represent the particles with spin up and down, respectively. 11

1.6 Double occupancy as a function of total atom numbers in the lattice for different values of on-site interaction U measured with respect to the hopping amplitude (here J). (**a**) Double occupancy for strong and weak coupling limit (black and white circles respectively), (**b**) Zoomed behavior for the strong coupling limit, here the solid red and blue lines represent the theoretical approach for D assuming full localization of atoms, i.e., neglecting the kinetic energy. From [JrSGn$^+$08]. 12

1.7 Slope $\partial D/\partial N$ as a function of U/h (here, h is Planck's constant). The compressibility $\partial D/\partial N$ was obtained from a least-squares fit of $D(N) = (\partial D/\partial N)N + D_0$ to the data in FIGURE 1.6. The solid line represents the expected value of $\partial D/\partial N$ in the atomic limit (neglected kinetic energy). From [JrSGn$^+$08]. 13

1.8 Crystallographic edge orientations in graphene nanoribbons fabricated by scanning tunnelling microscope lithography: (**a**) Armchair orientation, (**b**) Zigzag orientation. From [MJH$^+$14]. 14

1.9 Experimental and theoretical width dependence of the energy gap in graphene nanoribbons for the two possible edge orientation: (**a**) armchair, (**b**) zigzag. Theoretical data correspond to density functional theory for armchair ribbons depending on the number of rows in the ribbon ($3n$, $3n+1$ and $3n+2$, being $n = 1, 2, 3\cdots$), and from mean field Hubbard model approach for zigzag ribbons (solid lines are just a guide for the eye). From [MJH$^+$14]. 14

1.10 Mean field results for the spin density (red: spin up, blue: spin down) in ZGNR for a 5 nm strip (left) and 10 nm (right). From [MJH$^+$14]. 15

1.11 DMRG results for spin density (red: spin up, blue: spin down) in ZGNR: (**a**) $U/t = 0$, (**b**) $U/t = 4$. From [HL16]. 15

1.12 Spin and charge gaps at thermodynamic limit for a narrow ZGNR (with just one hexagon of wide) as a function of the on-site interaction parameter U of the model. From [HHLM03]. 16

2.1 Charge-Transfer complex example: (**a**) Molecular structure of TTF-Chloranil, (**b**) neutral phase of the CT complex, (**c**) ionic phase of the CT complex. Gray, green, red, yellow and white spheres represent C, Cl, O, S and H atoms respectively and the single and double lines represent the single and double bonds between the atoms. 20

2.2 Total energy of a DA pair in a CT complex as a function of ρ. The solid and dashed line corresponds to the energy in the neutral and ionic phase, respectively. 20

2.3 One-dimensional ionic Hubbard model phase diagram: Band insulator (BI) for $U < U_{c_1}$, spontaneously dimerized insulating phase (SDI) for $U_{c_1} < U < U_{c_2}$ and Mott-insulator for $U > U_{c_2}$. From [FGN99]. 22

2.4 The U dependence of gaps energy at the thermodynamic limit for an ionic Hubbard chain with $\Delta/t = 10$. The inset shows the behavior of gaps for a large range of U. From [MMNS04]. 23

2.5 Sketch of phases in the IHM in one-dimension: (**a**) band insulator phase for weak coupling limit, (**b**) spontaneous dimerized intermediate phase, (**c**) Mott-insulator for strong coupling limit. The red (resp. blue) spheres represent particles with spin up (resp. spin down). 24

2.6 Bond-order parameter at the thermodynamic limit as a function of local interaction in a one-dimensional lattice for a fix energy offset $\delta = 2\Delta = 20$. From [MMNS04]. 24

2.7 Optical lattice used by M. Messer *et al.* to explore the IHM in two dimension. (**a**) Laser beams disposition, (**b**) Honeycomb lattice with an energy offset between sites A and B of the unit cell. From [TGU$^+$12]. 25

2.8 Results of M. Messer's experiment. (**a**) Fraction of double occupied sites D as a function of local interaction U for a fix energy offset ($\Delta/t = 16.3(4)$), (**b**) Sketch of phase diagram of the IHM on a honeycomb lattice at half-filling. Hollow (resp. full) circles in figure (**a**) represent attractive (resp. repulsive) interaction between the atoms. From [MDU$^+$15]. 26

2.9 Lin HF's DMFT results for the IHM on a honeycomb lattice. (**a**) Double occupancy ($Docc = D$) as a function of local interaction for different values of energy offset, (**b**) staggered magnetization as a function of local interaction for different values of energy offset. From [LLTL15]. 27

2.10 Sketch of expected phases of the IHM with mass-imbalance on a one-dimensional lattice. (**a**) CDW phase for weak coupling limit ($U \ll \Delta$), (**b**) antiferromagnetic insulator phase for strong coupling limit ($U \gg \Delta$). The red and blue spheres represent the particles with spin up and down, respectively, and its radius represents the mass-imbalance between the two species of atoms in the lattice. From [PGFSV21]. 27

2.11 Mean-field density order parameters as a function of local interaction for different values of $t_\downarrow$. From [SBJJ17]. 29

2.12 Map of a honeycomb bipartite lattice, with L_x sites in the zigzag edge and L_y sites in the armchair edge, into an inhomogeneous chain with long hopping. (a) Honeycomb lattice with $L_x = 2$ and $L_y = 2$, (b) image of honeycomb lattice with $L_x = 2$ and $L_y = 2$ into a chain, (c) honeycomb lattice with $L_x = 2$ and $L_y = 4$, (d) image of honeycomb lattice with $L_x = 2$ and $L_y = 4$ into a chain. The solid red spheres and fuzzy blue circles represent the two type of sites in the bipartite lattice. The x and y axis in the figure (a) and (b) represent the coordinates of each (x, y)-site in the honeycomb lattice. The solid red lines (resp. dashed blue lines) in figure (b) y (d) represent the hopping of particles to its first neighbors (resp. second or fourth neighbors). 30

2.13 Charge gap of a narrow honeycomb lattice with $\Delta/t = 10$ and $L_y = 2$: (**a**) gap as a function of U for lattice sizes $L_x = 10, 13, 16, 19, 22$ and 25, (**b**) finite size scaling for some U values. The solid line in (**a**) is a visual guide, meanwhile the solid and dashed lines in (**b**) show a least-square fit to a second order polynomial $a + b/L^2$. 31

2.14 Spin gap of a narrow honeycomb lattice with $\Delta/t = 10$ and $L_y = 2$: (**a**) gap as a function of U for lattice sizes $L_x = 10, 13, 16, 19, 22$ and 25, (**b**) finite size scaling for some U values. The solid line in (**a**) is a visual guide, meanwhile the solid and dashed lines in (**b**) show a least-square fit to a second order polynomial $a + b/L^2$. 32

2.15 Excitation gap of a narrow honeycomb lattice with $\Delta/t = 10$ and $L_y = 2$: (**a**) gap as a function of U for lattice sizes $L_x = 10, 13, 16, 19, 22$ and 25, (**b**) finite size scaling for some U values. The solid line in (**a**) is a visual guide, meanwhile the solid and dashed lines in (**b**) show a least-square fit to a second order polynomial $a + b/L^2$. 33

2.16 Charge, spin, and excitation gap at thermodynamic limit for a narrow honeycomb lattice with $\Delta/t = 10$ and $L_y = 2$. Solid lines are a visual guide. . . 34

2.17 Susceptibility of fidelity for narrow honeycomb lattices with $\Delta/t = 10$, $L_y = 2$ and $dU = 0.01$. Solid lines are a visual guide. 35

2.18 Double occupancy as a function of U/t for a lattice with $L_x = 25$, $L_y = 2$ and $\Delta/t = 10$ 35

2.19 Density per site in a honeycomb lattice with $L_x = 25$, $L_y = 2$ and $\Delta/t = 10$. (**a**) Density profiles for $U/t = 10$, (**b**) Density profiles for $u/t = 30$. In the top of each figure is shown the profile of total density $n(i) = \langle n_i \rangle$ of the lattice, while in the bottom of each figure is shown the spin density profiles $n_\uparrow(i) = \langle n_{i,\uparrow} \rangle$ and $n_\downarrow(i) = \langle n_{i,\downarrow} \rangle$. Solid lines are a visual guide. 36

2.20 Spin correlation for a lattice with $L_y = 2$, $L_x = 25$ and $\Delta = 10$ for two values of local interaction parameter. (**a**) Correlation function along the top zigzag edge, (**b**) Correlation function along the sites in the top of edge (sites with x coordinate even). The inset of figure (**a**) shows the spin correlation between sites of different edge for $U/t = 30$, meanwhile the inset of figure (**b**) shows a semi-log plot of the correlation function for $U/t = 30$. Solid lines are a visual guide. 37

2.21 Gap energies and fidelity susceptibility as a function of U for a narrow honeycomb lattices with $L_y = 2$ and $\Delta/t = 0.4$: (**a**) charge, spin, and excitation gap energy at the limit $L_x \to \infty$, (**b**)Susceptibility for different lattice sizes. 38

2.22 Charge, spin, and excitation gap for a narrow honeycomb lattice with $\Delta/t = 10$, $L_x = 6$, $L_y = 4$. Solid lines are a visual guide. 39

2.23 Fidelity susceptibility for narrow honeycomb lattices with $\Delta/t = 10$, $L_x = 6$, $L_y = 4$ and $dU = 0.01$. Solid lines are a visual guide. 40

2.24 Double occupancy as a function of U/t for a lattice with $L_x = 6$, $L_y = 4$ and $\Delta/t = 10$ 40

2.25 Density per site in a honeycomb lattice with $L_x = 6$, $L_y = 2$ and $\Delta/t = 10$. (**a**) Density profiles for $U/t = 10$, (**b**) Density profiles for $u/t = 30$. In the top of each figure is shown the profile of total density $n(i) = \langle n_i \rangle$ of the lattice, while in the bottom of each figure is shown the spin density profiles $n_\uparrow(i) = \langle n_{i,\uparrow} \rangle$ and $n_\downarrow(i) = \langle n_{i,\downarrow} \rangle$. Solid lines are a visual guide. 41

2.26 Spin correlation for a lattice with $L_y = 4$, $L_x = 6$ and $\Delta = 10$ for two values of local interaction parameter. (**a**) Correlation function along first row of lattice (top zigzag edge), (**b**) Correlation function along second row of lattice, (**c**) Correlation function along the sites in the top of edge (sites with x coordinate such that $x \equiv 4 \; mod \; 8$). The inset of figure (**a**)-(**b**) shows the spin correlation between sites of different rows for $U/t = 30$, meanwhile the inset of figure (**c**) shows a semi-log plot of the correlation function for $U/t = 30$. Solid lines are a visual guide. 42

2.27 Charge and excitation gap in the thermodynamic limit as a function of local parameter for a lattice with $\Delta/t_\uparrow = 2.0$ and two values of imbalance parameter: (a) $t_\downarrow/t_\uparrow = 0.5$, (b) $t_\downarrow/t_\uparrow = 0.9$. The Extrapolated values of the gaps were obtained by a linear fit as a function of $1/L$, as the finite size scaling that it is shown in the inset of figure (a) for $U/t = 4.55$. The lines are visual guides. From [PGFSV21]. 43

2.28 Physical quantities of an ionic Hubbard chain as a function of local interaction for lattices with $\Delta/t_\uparrow = 2.0$ and $t_\downarrow/t_\uparrow = 0.9$: (a) Spin gap in the thermodynamic limit, (b) staggered magnetization for a lattice with $L = 144$ sites, (c) ground state energy for a lattice with $L = 144$ sites. The inset of figure (a) shows a finite-size scaling to a quadratic polynomial of $1/L$ (dashed lines) used to obtain the extrapolated spin gap value for $U/t_\uparrow = 5.8$. The inset of figure (b) shows the spin density profile for $U/t_\uparrow = 5.8$. The inset of figure (c) shows the first derivative of the ground state energy. The solid lines are visual guides. From [PGFSV21]. 44

2.29 von Neumann block entropy as a function of local interaction for a lattice with $L = 512$ sites, $\Delta/t_\uparrow = 2.0$ and $t_\downarrow/t_\uparrow = 0.9$. The inset shows the dependence of block entropy with respect to the inverse of the lattice size. From [PGFSV21]. 45

2.30 Phase diagram of the IHM with mass-imbalance. In figure (a) (resp. figure (b)), critical points obtained with MFT (blue empty squares, from [SBJJ17]) and DMRG (black circles corresponding to extrapoled values from maximum of entropy) are shown in the $\Delta - U^*$ plane (resp. $t_\downarrow - U^*$ plane). In figure (c), the critical point surface as a function of energy offset and imbalance parameter is shown. This surface divides the space into the CDW insulator phase (above the surface) and antiferromagnetic insulator phase (beneath the surface). From [PGFSV21]. 46

31 Scheme of a ladder lattice with local interactions. 50

32 Bipartite decomposition of a one dimensional lattice used to calculate the density matrix of whole system in the DMRG algorithm. 51

33 Two possible maps of a ladder lattice into an inhomogeneous chain: (**a**)-(**b**) first mapping, (**c**)-(**d**) second mapping. 52

Introduction

Several technological developments achieved during the twenty century like the laser and neutron spectroscopes [SWM, HSS71], the ion traps [Deh68, Deh69] or the laser cooling technique [CMDCT89] gave rise to powerful tools to explore a set of features of atoms and complex materials. The prediction and observation of phenomena such as the antiferromagnetism in MnO [SS49], the superfluity of helium-3 [ORL72, OGRL72], the Bose-Einstein condensation [AEM$^+$95] in a dilute gas of atoms of ^{87}Rb between others were some of the great achievements of that time. But at the end of the century, despite the increased knowledge about the structure of complex materials, it became evident that theoretical approaches like the band theory or the density functional theory were not enough to explain the observed phenomena. This failure highlighted the importance and nontrivial role of the interactions in the many-body systems.

On the other hand, the theoretical works and experiments with cold trapped atoms established a new way to study many-body physics. For instance, the paper of Jaksch *et al* [JBC$^+$98] and posterior experiment of Bloch-Hänsch group [Gre02] shown that materials where the interaction between its particles is relevant can be studied, or *simulated*, using an effective system of atoms stored in a periodical arrangement called *optical lattice*. In these systems, physical characteristics like the interaction strength between the atoms or the crystalline structure of the lattice can be controlled by fixing a few optical parameters which allows a careful exploration of the strong correlated matter physics.

Now, this new perspective about the interacting systems opened a wide research line in condensed matter physics not only in the experimental branch, but also in the theoretical and computational one. Tools like the Bethe ansatz, bosonization, conformal field theory (CFT), dynamical mean field theory (DMFT), quantum Monte-Carlo (QMC), numerical renormalization group (NRG) or density matrix renormalization group (DMRG) are some exact and approximated methods that appear in the context of optical lattices. The application of those methods together with the experimental realization of one and two dimensional lattices [GWO00, TGU$^+$12] has allowed the study of several phenomena such as the spin-charge separation, supersolid states, exotic insulator and magnetic phases, anisotropic superconductivity between others [FGKS05, JFG$^+$09, KHI$^+$09, KD07, CZLW10, GKR06, SE19a, GKR14, WI13, CBKG19, PH16a]. Due to the difficulty of describing this wide variety of interesting phenomena using an exact method, the theoretical investigation of many-body systems through numerical simulation of lattice models became more and more common.

One of the most recurrent models in this context is the *Hubbard model*, a simple model that includes the attractive or repulsive local interaction between particles in an optical lattice. Nowadays, the study of the competition between the characteristic energy scales

of the model together with the geometry and the dimension of lattice has allowed the description of numerous phenomena like the already mentioned. Turns out to be particularly interest the study of the *ionic Hubbard model*, a model which describes local interacting electrons in a bipartite lattice with an energy offset between neighbor sites. This model has been theoretically studied in one-dimension [FGN99, MMNS04, TAJN06] and two-dimension [PBH$^+$07, LLTL15, SE19b] where different types of transitions between a band insulator and an antiferromagnetic insulator have been reported, due to the competition between the energy offset Δ and the local interaction U between the electrons.

This transition was observed experimentally in 2015 by M. Messer *et al.* [MDU$^+$15]. In Messer's experiment, the ionic Hubbard model was realized on a honeycomb lattice using a two-component gas of ^{40}K load into an optical lattice. On the one hand, for weak interaction with respect to the energy offset ($U \ll \Delta$), they notice the atoms of ^{40}K with different spin tend to occupy a same site, leading to a band insulator phase with a charge density wave. On the other hand, for strong interaction between atoms ($U \gg \Delta$), they observe that each site is occupied by a single atom such that there is an antiferromagnetic order in the lattice.

In regard to the intermediate regime ($U \sim \Delta$), M. Messer and co-workers did not explore this regime, keeping open a question about the physics of this region which is a current controversial discussion. This because, according to theoretical studies in one-dimension, the ionic Hubbard model presents an intermediate dimerized insulating phase for $U \sim \Delta$ [MMNS04]. However, in two-dimensional lattices different type of insulator phases or even the absence of the intermediate phase has been predicted [PBH$^+$07, KD07, CZLW10, LLTL15, CBKG19].

Motivied by this open question, we explore the ionic Hubbard model in two scenarios using a density matrix renormalization group (DMRG) algorithm with a matrix product state (MPS) method. In the first scenario, we explore the ground state of the model on a narrow honeycomb lattice through a one-dimensional map. We explore narrow lattices due to the limitation of the DMRG algorithm to work with wide lattices [SW12]. In the second scenerio, we study the ground state of the model in a one-dimensional lattice, considering that the $SU(2)$ symmetry of the model is explicitly broken by a mass-imbalance in the system (mass-imbalanced ionic Hubbard model). For these scenarios, we want to know if there is a shift in the position of the critical points with respect to the one-dimensional ionic Hubbard model [MMNS04] and the previous numerical researches based in mean-field and dynamical mean-field theory [SBJJ17, LLTL15]. We use the MPS method in order to reduce the numerical complexity of our simulations, in particular for the honeycomb lattice.

This document is organized as follows: In Chapter I, the Hubbard model is described in the context of optical lattices and recent theoretical and numerical researches about this model in honeycomb and mass-imbalanced lattices are reviewed. In Chapter II, the physics of the ionic Hubbard model in one and two-dimensional lattices are briefly described and the results of the investigation are presented. Finally, in Conclusions, the conclusions of this investigation are presented.

CHAPTER 1

Hubbard Model

In this chapter, we give a detailed description of the Hubbard model from its origin around the metal-insulator transition. In order to highlight the relevance of the model nowadays, we present a wide discussion about this model in the context of ultracold atoms physics. Also, we give a review of recent theoretical and numerical researches in respect to the effects of interaction in periodical lattices described by the Hubbard model. In particular, we regard two systems: narrow honeycomb lattices and lattices with mass-imbalance.

1.1 Fermi-Hubbard model

The understanding of effects of correlations in an electron gas was one of the problems that rose to attention in the middle of the twentieth century [Pin53, SBFB57]. Since, the theoretical models for a free electron gas, implemented for a long time to describe the characteristics of conducting bands of metals and alloys, do not give a good explanation to the behavior of d- and f-electrons in materials composed by transition metals or rare-earth metals. For instance, the insulator nature of the nickel oxide (NiO) could not be explained those traditional models.

In that time, there were two approximations for the electric and magnetic properties of electrons in a material, the first one is known as *the valence bond model* [HL27, Mis12] where each atom in a molecule is considered to be in a bonding or antiboding state causing the electrons in a material to remain in the bond between two atoms, this theory describes the usual insulators like $NaCl$. The other model is known as *the band theory* [WD31] for metals, where the electrons of the conduction band are considered as a free gas. These approaches seem to be different approximations to the wave-function of a solid, however in 1949 *Nevill Mott* [Mot49] showed that both models are actually the same approximation, giving a possible explanation to the insulator state of NiO.

In fact, the band theory and valence bond model are the same approximation, since they both essentially neglect the electron-electron interaction energy in the solids to describe their properties. But in the particular case of the NiO, an inconsistency between these models seems to appear. According to the band theory, the nickel oxide must be a metal due to its partially filled d-band, however the pure state of this oxide is an insulator. At the same time, this insulator state can not be predicted by the valence bond model,

because there are unpared electrons in the d-band. This inconsistency suggests that the electron-electron correlation in the NiO must be relevant.

Following this argument, N. Mott asserted that NiO can not be a metal because the electrostatic interaction between electrons does not let them move at all. Despite this affirmation, the fundamental reason of the insulator state of NiO and the apparent contradiction between both theories was no yet explained clearly, until the proposal of *John Hubbard* in 1963 [hub63] of a model to study the effects of correlations in narrow bands. This model, called as *Hubbard model*, is described by the following Hamiltonian:

$$\mathcal{H} = \sum_{\mathbf{k}\sigma} \epsilon_{\mathbf{k}} c^{\dagger}_{\mathbf{k}\sigma} c_{\mathbf{k}\sigma} + \frac{1}{2} \sum_{\mathbf{k}_1\mathbf{k}_2\mathbf{k}'_1\mathbf{k}'_2\sigma_1\sigma_2} \langle \mathbf{k}_1\mathbf{k}_2 | \, V \, | \mathbf{k}'_1\mathbf{k}'_2 \rangle \, c^{\dagger}_{\mathbf{k}_1\sigma_1} c^{\dagger}_{\mathbf{k}_2\sigma_2} c_{\mathbf{k}'_2\sigma_2} c_{\mathbf{k}'_1\sigma_1}$$

$$- \sum_{\mathbf{k}\mathbf{k}'\sigma} \Big(2 \langle \mathbf{k}\mathbf{k}' | \, V \, | \mathbf{k}\mathbf{k}' \rangle - \langle \mathbf{k}\mathbf{k}' | \, V \, | \mathbf{k}'\mathbf{k} \rangle \Big) \nu_{\mathbf{k}'} c^{\dagger}_{\mathbf{k}\sigma} c_{\mathbf{k}\sigma}, \tag{1.1}$$

where $V = V(\mathbf{x}, \mathbf{x}')$ is the Coulomb interaction potential between the electrons of the system. Here, the electrons are regarded to be in a partially-filled narrowband with a Hartree potential. The first term corresponds to the kinetic energy $\epsilon_{\mathbf{k}}$ of the electrons in each level of the bands, the second is the interaction energy between them and the last term is the Hartee-Fock potential due to the electrons in the s-band particularly. The operators $c^{\dagger}_{\mathbf{k}\sigma}$ and $c_{\mathbf{k}\sigma}$ are the creation and annihilation operators of an electron of momentum $\mathbf{k}$ and spin $\sigma = \uparrow, \downarrow$ that belong to the first Brillouin zone and $\nu_{\mathbf{k}}$ is the occupation number of electrons with momentum $\mathbf{k}$. The matrix elements of the Coulomb potential are given by

$$\langle \mathbf{k}_1\mathbf{k}_2 | \, V \, | \mathbf{k}'_1\mathbf{k}'_2 \rangle = \alpha \int_V \frac{\psi^*_{\mathbf{k}_1}(\mathbf{x}) \psi_{\mathbf{k}'_1}(\mathbf{x}) \psi^*_{\mathbf{k}_2}(\mathbf{x}') \psi_{\mathbf{k}'_2}(\mathbf{x}')}{|\mathbf{x} - \mathbf{x}'|} d\mathbf{x} d\mathbf{x}',$$

being α the strength of Coulomb interaction and $\psi_{\mathbf{k}}(\mathbf{x})$ is the wave-function of an electron with momentum $\mathbf{k}$. The usual form of this model is found by introducing the creation and annihilation particle operators of an electron in a lattice site j with spin σ is given by:

$$c^{\dagger}_{j\sigma} = \frac{1}{\sqrt{Vol}} \sum_{\mathbf{k}} e^{-i\mathbf{k}\cdot\mathbf{R}_j} c^{\dagger}_{\mathbf{k}\sigma}, \qquad\qquad c_{j\sigma} = \frac{1}{\sqrt{Vol}} \sum_{\mathbf{k}} e^{i\mathbf{k}\cdot\mathbf{R}_j} c_{\mathbf{k}\sigma},$$

where Vol is the volume of the crystalline lattice. Here $\mathbf{R}_j$ is the vector of the lattice site j and V is the size of the system. Also, it is necessary to consider the Wannier functions $\phi(\mathbf{x})$ defined by

$$\phi(\mathbf{x}) = \frac{1}{\sqrt{Vol}} \sum_{\mathbf{k}} e^{-i\mathbf{k}\cdot\mathbf{x}} \psi_{\mathbf{k}}(\mathbf{x}).$$

Using those definitions, the Hubbard Hamiltonian can be written straightforward as

$$\begin{aligned}\mathcal{H} = &\sum_{ij} t_{ij} c^\dagger_{i\sigma} c_{j\sigma} + \frac{1}{2} \sum_{ijlm\sigma_1\sigma_2} \langle ij| V |lm\rangle \, c^\dagger_{i\sigma_1} c^\dagger_{j\sigma_2} c_{l\sigma_2} c_{m\sigma_1} \\ &- \sum_{ijlm\sigma} \left(2 \langle ij| V |lm\rangle - \langle ij| V |ml\rangle\right) \nu_{jm} c^\dagger_{i\sigma} c_{l\sigma},\end{aligned}$$

where

$$\begin{aligned}t_{ij} &= \frac{1}{V} \sum_{\mathbf{k}} \epsilon_{\mathbf{k}} e^{i\mathbf{k}\cdot(\mathbf{R}_i - \mathbf{R}_j)}, \\ \langle ij| V |lm\rangle &= \alpha \int \frac{\phi^*(\mathbf{x} - \mathbf{R}_i)\phi(\mathbf{x} - \mathbf{R}_m)\phi^*(\mathbf{x}' - \mathbf{R}_j)\phi(\mathbf{x}' - \mathbf{R}_l)}{|\mathbf{x} - \mathbf{x}'|} d\mathbf{x} d\mathbf{x}', \\ \nu_{ij} &= \frac{1}{Vol} \sum_{\mathbf{k}} \nu_{\mathbf{k}} e^{i\mathbf{k}\cdot(\mathbf{R}_i - \mathbf{R}_j)}.\end{aligned}$$

Since the electrons belong to a narrow s-band, the Wannier functions can be approximated as an atomic s-functions which are localized, i.e. that those functions do not overlap so much with its neighbor functions, if the bandwidth is small enough. This implies that the integral $\langle ii| V |ii\rangle = U$ has a magnitude much greater than the magnitude of any other integral, leading to the following approximation in the Hamiltonian:

$$\begin{aligned}\mathcal{H} &= \sum_{ij} t_{ij} c^\dagger_{i\sigma} c_{j\sigma} + \frac{1}{2} \sum_{ijlm\sigma_1\sigma_2} U \delta_{ij}\delta_{il}\delta_{im} c^\dagger_{i\sigma_1} c^\dagger_{j\sigma_2} c_{l\sigma_2} c_{m\sigma_1} - \sum_{ijlm\sigma} \left(U \delta_{ij}\delta_{im}\delta_{il}\right) \nu_{jm} c^\dagger_{i\sigma} c_{l\sigma} \\ &= \sum_{ij} t_{ij} c^\dagger_{i\sigma} c_{j\sigma} + \frac{U}{2} \sum_{i\sigma_1\sigma_2} c^\dagger_{i,\sigma_1} c^\dagger_{i,\sigma_2} c_{i,\sigma_2} c_{i,\sigma_1} - U \sum_{i\sigma} \nu_{ii} c^\dagger_{i,\sigma} c_{i,\sigma} \\ &= \sum_{ij} t_{ij} c^\dagger_{i\sigma} c_{j\sigma} + U \sum_i n_{i,\uparrow} n_{i,\downarrow} - U \sum_i \nu_{ii} n_i,\end{aligned}$$

where the anticommutation rules of the fermionic operators $c^\dagger_{i,\sigma}, c_{i,\sigma}$ and the definitions $n_{i,\sigma} = c^\dagger_{i,\sigma} c_{i,\sigma}$, $n_i = n_{i,\uparrow} + n_{i,\downarrow}$, were considered in the last line. Since $\nu_{ii} = \frac{1}{Vol} \sum_{\mathbf{k}} \nu_{\mathbf{k}} = \frac{N}{2Vol}$, being N the total number of electrons, then

$$\begin{aligned}\mathcal{H} &= \sum_{ij} t_{ij} c^\dagger_{i\sigma} c_{j\sigma} + U \sum_i n_{i,\uparrow} n_{i,\downarrow} - \frac{UN}{2Vol} \sum_i n_i \\ \mathcal{H} &= \sum_{ij} t_{ij} c^\dagger_{i\sigma} c_{j\sigma} + U \sum_i n_{i,\uparrow} n_{i,\downarrow} - \frac{UN^2}{2Vol}.\end{aligned}$$

The last term is a constant and can be dropped. Thus, as long as the condition over the integral $\langle ii|\, V\, |ii\rangle$ is valid, the Hamiltonian (1.1) can be approximated to the following Hamiltonian:

$$\mathcal{H} = \sum_{ij} t_{ij} c^{\dagger}_{i\sigma} c_{j\sigma} + U \sum_{i} n_{i,\uparrow} n_{i,\downarrow}, \tag{1.2}$$

called Hubbard's Hamiltonian. Although in this derivation done by Hubbard the electrons are supposed to be in an s-band, himself discusses [HF64a] that this approximation is valid even for $3d$-electrons in transition metals. Besides, the solution of this model provided a connection between the valence bond model and the band theory such that a metal-insulator (MI) quantum phase transition[1] is predicted [HF64b] and finally a theory for the insulating state of NiO was given.

A MI transition was discussed previously also by N. Mott who, as we already mentioned, highlighted the importance of the electrostatic interaction in this phenomenon [Mot49, Mot56, Mot61]. In the works of N. Mott, a phase transition from a metallic to a non-metallic in a crystalline lattice is supposed to be related with the increase of the lattice parameter at zero temperature. From the point of view of the Hubbard model, this hypothesis corresponds to the prediction of a quantum phase transition when the electrostatic coupling U is much larger than the hopping parameter t, $U \gg t$.

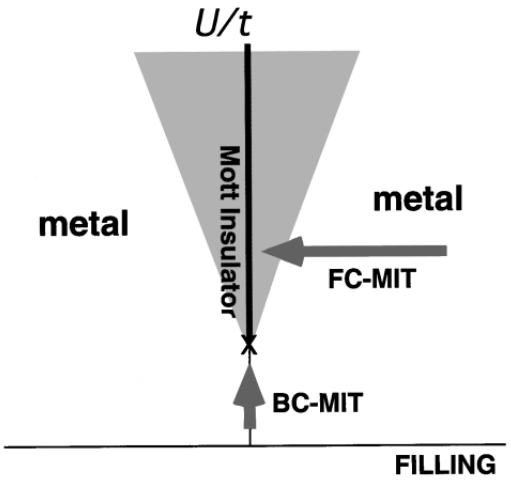

FIGURE 1.1. Sketch of MI transition in the plane n-U/t. The transition can occur by two ways: the filling-control metal-insulator transition (FC-MIT) and the bandwidth-control metal-insulator transition (BC-MIT). From [IFT98]

.

The Hubbard model particularly predicted the MI transition for a special case where the number of electrons in the lattice is one per site (half-filling) and there is not a ferromagnetic order in the lattice such that the number of electrons of spin up and spin down are the same. However, the MI transition can occur by tuning two parameters

[1] A *quantum phase transition* is a phase transition at zero temperature where the transition is given by tuning of non-thermal parameter as an external magnetic field in the quantum Hall effect [AMU75] or the electrostatic interaction energy U in the Hubbard model.

[IFT98], the electrostatic interaction strength U/t and the band filling n (ratio between the number of particles and the length of lattice). In FIGURE 1.1 a sketch of the MI transition by two routes is shown. On one hand, the transition described by Hubbard, a bandwidth-control metal-insulator transition (BC-MIT) where the transition is given by the shifting of the U/t parameter and a fix vale of the filling ($n = 1$ for half-filling case). On the other hand, the transition caused by a filling-control (FC-MIT). This transition is particularly interesting by its relation[2] with the high-T_c cuprate superconductors discovered in 1986 [BM86] which motivated the studies about the Hubbard model in two-dimensional lattices.

Additionally, the MI transitions can be broadly classified according to various aspects of the metal and insulator side of the transition as well as the dimensionality. Principally, the spin and orbital components and its *degrees of freedom* are important for this classification. Either in the metal or insulator side, three types of phases are possible near to the transition, all those depending on its excitation spectrum and whether there are broken symmetries.[IFT98].

In a first kind of insulators, a symmetry breaking[3] leads to a density wave in the system. For instance, if the symmetry related with the spin component is broken, an antiferromagnetic or a ferromagnetic state is expected for the ground state. Similarly, a lifting of degeneracy in d orbitals (t_{2g} orbitals) cause a staggered orbital order or a uniform orbital order in the phase. An example of this kind of insulators is the antiferromagnetic phase observed in the oxide V_2O_3 where the MI transition is a FC-MIT [MRR$^+$71].

Now, if no symmetry is broken, the insulator ground state is expected to be in the spin sector with projection $S_z = 0$[LM62], which can be degenerated or not. When the state with $S_z = 0$ is not degenerated, there is an energy difference (spin gap) between the state with total spin $S = 1$ and the state with total spin $S = 0$ of the system. Some examples of this kind of insulators are doped cuprates like $Sr_{14-x}Ca_xCu_{24}O_{41}$ [QBXFQ$^+$08, KSK96], organic salts like $TTF\text{-}TCNQ$ [Leo81], Kondo insulators between others [Mot90, IFT98]. The MI transition related to those insulators is in general also a FC-MIT and the insulator phase is characterized by a small spin gap compared with the charge gap [Hid92, KI93, KI94]. This insulator phase without symmetry breaking must be differentiated from the band insulator phase (full-filled band insulator, for example) where the spin and charge gap are both finite and have the same electron-hole excitation gap. These phases will be important later in the development of this thesis.

Finally, the third type of insulator is an insulator where neither of the symmetries are broken nor a spin gap exits. This phase is presented in the one-dimension Hubbard model at half-filling. Due to the large quantum fluctuations natural for low dimensional systems and the algebraic decay of antiferromagnetic correlation, the MI transition have not a spontaneous symmetry breaking (Mermin-Wagner theorem) neither a gap in the spin excitation spectrum. However, despite the absence of a symmetry breaking, this insulator phase has an antiferromagnetic order in the chain [LW68] which is a very amazing feature that turned it into the center of the research around MI transition in the last 50 years.

In regard to the metal phases near to MI transition, those can be classified also according to symmetry breaking in their components. For the symmetry breaking phase a spin or orbital density wave is expected, for example the weakly first order BC-MIT from an antiferromagnetic metal toward an antiferromagnetic insulating phase observed in $NiS_{2-x}Se_x$ pyrite [MTS$^+$00]. In the other case, again the most interesting one, the

[2] Typical compounds of cuprate superconductors are Mott insulators.

[3] Here we refer to an explicit symmetry breaking or a spontaneous one.

MI transition occurs in low dimensional systems where the symmetry breaking is not possible due to the large quantum fluctuations. In this case, two different phases emerge [KTK98, TLN$^+$92, NYKS96]: a superconductor phase and a metallic Fermi-liquid phase.

METAL \ INSULATOR	I_1 (symmetry breaking)	I_2 (spin gap)
M_1 (symmetry breaking)	V_2O_3, $NiS_{2-x}Se_x$	$La_{1-x}Sr_xCoO_3$ [KES$^+$96]
M_2 (superconductor)	$BEDT\text{-}TTF$ salts [KTK98]	$Sr_{14-x}Ca_xCu_{24}O_{41}$
M_3 (Fermi-liquid metal)	RNiO_3 [TLN$^+$92]	$La_{1.17-x}Sr_xVS_{3.17}$ [NYKS96]

TABLE 1.1. Overall MI transitions observed in various compounds. Adapted from [IFT98]

.

Although, the Mott-insulator phase is usually defined as an insulator caused by the local Coulomb repulsion, the classification discussed above shows that there is not a unique kind of insulator related with this interaction. Due to this, we will refer in general to the insulating phases related to the MI transition as correlated insulating phases (see a summary of these phases and its related transitions in TABLE 1.1) and as *Mott-insulator* to the engaging phase presented in the one-dimensional Hubbard model at half-filling.

1.2 Optical lattices and superfluid-insulator transition

Due to all these engaging phenomena observed around of the MI transitions, a great interest arose on the role of electric interactions in the physics of many-body systems. However, as we just saw, the emergence of those phenomena strongly depends on the structural properties of the materials. And even though in the twentieth century, these properties were widely studied by experimental techniques like laser and neutron spectroscopy [SWM, HSS71], ion traps [Deh68, Deh69], laser cooling technique [CMDCT89], between others, the inability of tuning the lattice parameters of the materials revealed the necessity of a new technique for a complete exploration of the physics of many-body systems.

Fortunately, these same technological developments did not just open new possibilities for ultrahigh-precision spectroscopy, but also allowed the study of crystalline solids in a controlled way [GWO00]. The formation of ordered structures in stored laser-cooled ions [Wal93] and the experimental relation of Bose-Einstein condensation using magnetic optical traps (MOT) [AEM$^+$95] started a wide research line in the condensed matter physics around of *ultracold atoms* and *optical lattices*.

Formally, an optical lattice is understood as a system formed by atoms stored in a crystalline lattice using optical traps and diverse cooling methods. The more typical optical traps are the *optical dipole traps* where neutral atoms are stored using the interference between counter-propagating laser beams with a Gaussian profile. Depending on the propagation direction of the beams and how many beams are used to create the trap, the atoms can be load into the resulting one, two or three-dimensional lattices.

For instance, when two laser beams are counter-propagating in the y-direction, the interference between them generates a three-dimensional potential given by [WS13]:

$$V(x,y,z) = -V_0 exp\left\{-2\frac{x^2+z^2}{w^2(y)}\right\}\cos^2(ky), \tag{1.3}$$

where

$$w(y) = w_0\sqrt{1+\left(\frac{y}{y_R}\right)^2}, \quad y_R = \frac{\pi w_0^2}{\lambda},$$

being λ the wave-length of the laser, $k = 2\pi/\lambda$ is the wave number, w_0 is the so-called the beam waist and V_0 is the maximum potential depth of the trap. This potential corresponds to a one dimensional lattice with a periodicity of $d = \lambda/2$ as we can see in FIGURE 1.2-**a**. The lattice periodicity can be shifted by introducing an angle α between the beams such that $d = \frac{\lambda}{2}\sin(\alpha/2)$.

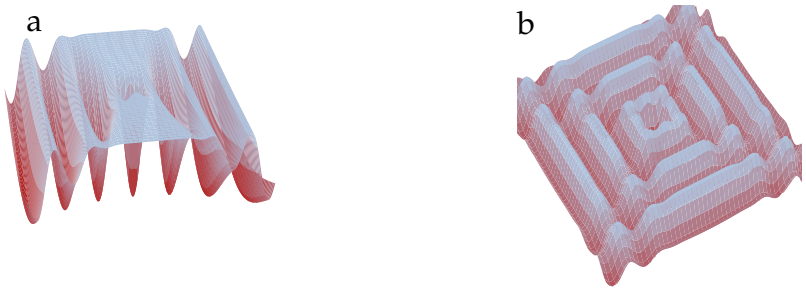

FIGURE 1.2. Optical lattice potential (for $z = 0$) produced by the interference between counter-propagating laser. (**a**) One dimensional lattice in y-direction given by (1.3), (**b**) Two dimensional lattice in the xy-plane given by (1.4).

Optical lattices of higher dimensions can be produced by using three or more laser beams[4]. For example, a regular square lattice in the xy plane can be generated by the interference of four laser beams, two in the y-direction and two in the x-direction (see FIGURE 1.2-**b**). The resulting potential is given by:

$$V(x,y,z) = -V_0 exp\left\{-2\frac{x^2+z^2}{w^2(y)}\right\}\cos^2(ky) - V_0 exp\left\{-2\frac{y^2+z^2}{w^2(x)}\right\}\cos^2(kx), \tag{1.4}$$

In order to load the atoms into the lattice, a MOT is used. First, the atoms are trapped in the MOT with a red detuning[5] near to resonance [RPC+87]. Then, before the magnetic trap be turned off, the dipole trap is simply overlapped with the atomic cloud captured in

[4] A regular triangular lattice is generated by the interference of three coplanar lasers beams with an angle of 120° between them [WS13].

[5] A red detuning means that the laser frequency is tuning below of the resonant frequency of the atomic system.

the MOT. Nowadays, an optical lattice can trap about $10^5 \sim 10^8$ atoms at temperatures from 10nK to 1μK and densities of $10^{10} \sim 10^{12}\text{cm}^{-3}$ [MCH93].

The low densities achieved in the loading process cause that the interaction[6] between atoms to be binary with a characteristic interaction distance r_0. In this regime, the trapped atomic gas is said to be *dilute* which means that the interaction range r_0 is much smaller than the mean particle separation, i.e. $nr_0^3 \ll 1$ where n the density of the gas.

Also, due to the low temperature of the system, the thermal de Broglie wavelength $\Lambda = \sqrt{2\pi\hbar^2/mk_BT}$ is much larger that the r_0, $\Lambda \gg r_0$. In this condition, called *ultracold limit*, the quantum behavior dominates the classical one, being this the principal reason because the optical lattices are an appropriate system to explore quantum phenomena of matter[7].

The most used atoms in this kind of traps are alkali atoms like ${}^6Li$, ${}^{40}K$, ${}^{87}Rb$ or isotopes of them because their transition wavelength lie within a convenient spectral range. Since the atoms loaded in an optical lattice constitute a dilute ultracold gas, the scattering inside the atomic gas does not depend on the shape of the potential. In fact, when two atoms of an ultracold gas collide within a potential $V_I(r)$, being r the radial distance between the atoms, the scattering amplitude does not depend on the scatter angle [LL59]. This means that the collision in the utracold limit just occurs when the relative angular momentum ℓ between the atoms is zero (s-regime).

Due to this, the potential $V_I(r)$ can be replaced by an effective hard-sphere with radius a which is described by a pseudo-potential $\mathcal{V}(\mathbf{r})$ given by[HY57]:

$$\mathcal{V}(\mathbf{r}) = \frac{4\pi\hbar^2 a}{m}\delta(\mathbf{r}) = g\delta(\mathbf{r}),$$

where m is the mass of the atoms loaded in the optical lattice[8] and a is called the *scattering length* which can be determined from the phase shift caused by the potential. Thus, ultracold atoms trapped in an optical lattice can be described by the following Hamiltonian [JBC$^+$98]:

$$\begin{aligned} H &= \int \psi^\dagger(\mathbf{x})\left(\frac{-\hbar^2}{2m}\nabla^2 + V(\mathbf{x})\right)\psi(\mathbf{x})d^3\mathbf{x} + \frac{1}{2}\int\int \psi^\dagger(\mathbf{x})\psi^\dagger(\mathbf{x}')\mathcal{V}(\mathbf{x}-\mathbf{x}')\psi(\mathbf{x})\psi(\mathbf{x}')d^3\mathbf{x}d^3\mathbf{x}' \\ &= \int \psi^\dagger(\mathbf{x})\left(\frac{-\hbar^2}{2m}\nabla^2 + V(\mathbf{x})\right)\psi(\mathbf{x})d^3\mathbf{x} + \frac{g}{2}\int \psi^\dagger(\mathbf{x})\psi^\dagger(\mathbf{x})\psi(\mathbf{x})\psi(\mathbf{x})d^3\mathbf{x}. \end{aligned} \tag{1.5}$$

where $\psi(\mathbf{x})$ is the field operator for the atoms. The atoms can be bosons or fermions, depending on internal nuclear structure. Expanding the field operator in the lattice site operators a_i, $\psi(\mathbf{x}) = \sum_i w(\mathbf{x}-\mathbf{x}_i)a_i$ with $w(\mathbf{x})$ the Wannier functions, the Hamiltonian can be rewritten as follows:

[6] Typically a Van der Waals short-range interaction.

[7] Due to the thermal de Broglie wavelength has the same order that the mean particle separation, the quantum statistics are also relevant in optical lattices. Quantum gases where this occurs ($n\Lambda^3 \gtrsim 1$) are referred as a *degenerate gases*.

[8] If the atoms that collides in the optical lattice have different masses, the *coupling constant* g in the pseudo potential is given by $g = 2\pi\hbar^2 a/\mu$, where μ is the reduced mass.

$$H = -\sum_{<i,j>} t_{ij} a_i^\dagger a_j + \frac{U}{2}\sum_i n_i(n_i - 1), \tag{1.6}$$

being a_i ($a_i^\dagger$) the annihilation (creation) operator of a particle at lattice site i which obeys bosonic or fermionic commutation or anti-commutation rules depending on the case, $U = g\int |w(\mathbf{x})|^4 d^3\mathbf{x}$ the strength of local interaction between two atoms, and $t_{i,j} = t = \int w(\mathbf{x} - \mathbf{x}_i)\left(\frac{-\hbar^2}{2m}\nabla^2 + V(\mathbf{x})\right) w(\mathbf{x} - \mathbf{x}_j)$ the hopping matrix element between neighbor site $< i, j >$.

The latter Hamiltonian is very similar to the Hubbard Hamiltonian discussed in the previous section. Indeed, for a fermionic gas, we have that $n_i(n_i - 1) = 2n_{i,\uparrow}n_{i,\downarrow}$[9], such that the Hamiltonian for fermions trapped in an optical lattice is exactly the Hubbard's Hamiltonian (1.2). For a bosonic gas, the Hamiltonian (1.6) is commonly called as the Bose-Hubbard Hamiltonian which exhibits a very interesting quantum phase transition, likewise its fermion counterpart. As we discussed in the previous section, this transition depends on the interaction strength U/t that, in this optical lattice scenario, can be smoothly tuned by fixing either the potential depth or the scattering length. The former quantity is related with the value of the hopping amplitude, while the latter is related with the on-site interaction between the atoms.

The Hubbard's transition in a bosonic ultracold gas is similar to the fermionic one, but in the bosonic case, the metallic phase for the weak interaction limit ($U/t << 1$) actually corresponds to a superfluid phase [FWGF89, Leg98]. This was firstly observed by M. Greiner *et al.*[Gre02] in 2002 where a Bose-Einstein condensate of ^{87}Rb atoms loaded in a three-dimensional optical lattice was studied. In this experiment, they observed the transition from the superfluid phase to an insulator phase controlling the lattice potential depth, V_0. As this quantity was increased in the experiment, the hopping amplitude decreased exponentially such that a Mott-insulator phase was observed for low values of V_0.

In fact, in FIGURE 1.3, it is shown a series of absorption images of the interference pattern in the lattice for different values of V_0. Here, we can observe that a coherent insulator phase appears for low values of V_0, since there is a clear maximum of interference localized (see FIGURE 1.3-**a**) in a lattice site which is characteristic of the Mott-insulator phase. For high values of V_0, this maximum of interference decrease causing the interference pattern of the lattice to disappear (FIGURE 1.3g-**h**) such that the system enters toward the superfluid phase.

This experiment undoubtedly showed that optical lattices and the Hubbard model are a perfect scenario to study or *simulate* the physics of condensed matter. However, in the last decades, the exploration of the Hubbard model in optical lattices has been also relevant in other branches of the physics. In particular, the transition toward the Mott-insulator phase is supposed to be a good initial state for quantum computing [JBC+99]. Nevertheless, the initialization is not the unique challenge to realize a real quantum computer. For instance,

[9] In a fermionic system we have that $n_i = n_{i,\uparrow} + n_{i,\downarrow}$ and $n_{i,\sigma}^2 = n_{i,\sigma}$ for $\sigma = \uparrow, \downarrow$, then:

$$n_i(n_i - 1) = n_i^2 - n_i = n_{i,\uparrow}^2 + n_{i,\downarrow}^2 + 2n_{i,\uparrow}n_{i,\downarrow} - n_{i,\uparrow} - n_{i,\downarrow} = 2n_{i,\uparrow}n_{i,\downarrow}.$$

achieve long decoherence times or find an *universal* set of quantum gates is also important to quantum computing [DiV00].

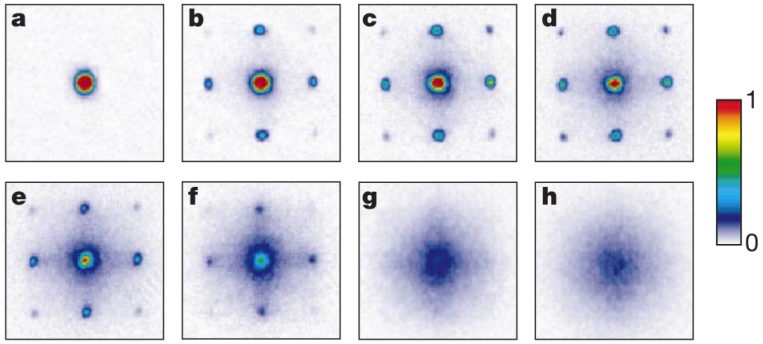

FIGURE 1.3. Absorption image of the lattice after of a time-flight of 15 ms. The lattice potential depth is measured in units of the *recoil energy* $E_r = 2\pi^2\hbar^2/m\lambda^2$, being λ the wavelength of the lattice. The values of V_0 are: (**a**) 0, (**b**) $3E_r$, (**c**) $7E_r$, (**d**) $10E_r$, (**e**) $13E_r$, (**f**) $14E_r$, (**g**) $16E_r$, (**h**) $22E_r$. From [Gre02].

1.3 Experimental realization of The Fermi-Hubbard model in optical lattices

In regard to the realization of Hubbar's Hamiltonian in an optical lattice, in 2008 R. Jördens *et al.* [JrSGn$^+$08] achieved to explore this model in a three-dimensional lattice load with a Fermi-Fermi balanced mixture of ^{40}K in two states of the hyper-fine $F = 9/2$ manifold. In this experiment, unlike to the Greiner's experiment, the effect of interaction in the fermionic gas was studied directly tuning the on-site interaction parameter. This is possible due to a phenomenon called *Feshbach resonance* where two atoms that collide in a magnetic field can be trapped in a resonant bound molecular state, causing a shift in the scattering length at low energies.

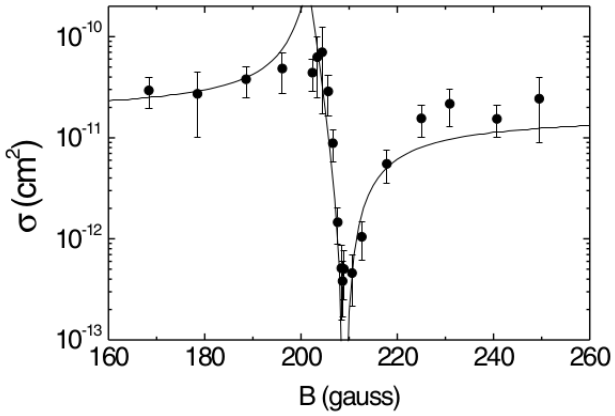

FIGURE 1.4. Elastic scattering cross-section of the collision between atoms of ^{40}K in $|9/2, -9/2\rangle$ and $|9/2, -7/2\rangle$ states loaded in an optical lattice as a function of the magnitude of an external uniform magnetic field. From [LRT$^+$02].

Feshbach resonance occurs when two states in different collision channels[10] are energetically close. This resonance has been observed in ultracold gases of ^{40}K [LRT^{+}02] or ^{6}Li [BAR^{+}05] as well as in several heteronuclear mixtures like ^{87}Rb -^{88}Sr [BCP^{+}18], ^{87}Rb -^{40}K [IGO^{+}04], ^{6}Li -^{173}Yb [GLST^{+}20]. Since the state energy of the atoms depends on its internal structure (nuclear and spin structure), the resonance between the two states can be carefully controlled by the applied magnetic field thanks to the Zeeman effect. For example, in a spin-mixture of ^{40}K atoms in the $|9/2, -9/2\rangle$ and $|9/2, -7/2\rangle$ states, the scattering cross-section depends on the magnetic field (see FIGURE 1.4). This directly implies a shift in the scattering length and in the on-site interaction between the atoms caused by the magnetic field [CGJT10].

The Fermi-mixture of ^{40}K in the R. Jördens's experiment can be created from an ultracold fermionic gas in two stages: an evaporation stage and a transfer stage [LRT^{+}02, DJ99]. First, the initial gas is polarized in the $|9/2, 9/2\rangle$ state by removing the other spin states of the gas applying a frequency-swept microwave field (evaporative cooling). Then, the polarized gas is loaded into the optical lattice where a radio-frequency field is applied in order to transfer the atoms in the $|9/2, 9/2\rangle$ state to the $|9/2, -9/2\rangle$-$|9/2, -7/2\rangle$ mixture state. In both steps, the magnetic field is generated between the two coils of the MOT.

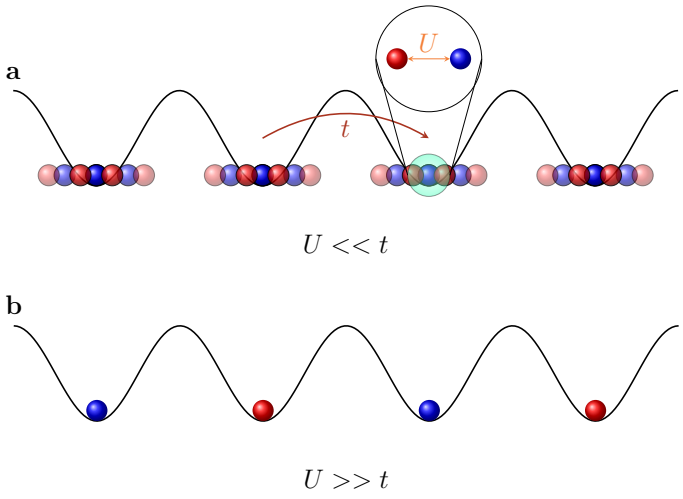

FIGURE 1.5. Sketch of metallic and insulator phases near to MI transition: (**a**) Metallic phase where the particles are not localized moving between the lattice sites, (**b**) Mott-insulator phase where the particles are localized and an antiferromagnetic order is observed. The red and blue spheres represent the particles with spin up and down, respectively.

The effects of correlation in the R. Jördens's experiment was studied from the fraction of double occupied sites, D. This quantity can be measured by an absortion image of the lattice after increasing rapidly the depth of the optical lattice in order to prevent any tunneling of the atoms. According to our previous discussion about MI transition in the Hubbard model, when the system is in the strong correlation limit ($U >> t$), the atoms can not move between the lattice sites leading to an antiferromagnetic ordering with no

[10] When two atoms collides in a potential, the scatter state can be trapped in the potential o not depending on the spin and nuclear structure of the atoms itself. The states trapped in the potential are regarded to be in the close channel of the potential, while the free scattered states are said to be in the open channel of the potential.

double occupied sites (see FIGURE 1.5-(b)). Conversely, in the weak regime ($U << t$), the system must be in a metallic phase such that the atoms are not localized (see FIGURE 1.5-(a)). In this case, if the depth of the lattice is increased, a non-null double occupancy must be observed. Taking into account this, R. Jördens *et al.* predicted a MI transition in their experiment, since a high double occupancy was observed for the non-interacting case (see white circles in FIGURE 1.6-**a**), meanwhile this quantity is less than 6% for a non-null value of the coupling energy (see FIGURE 1.6-**b**). Furthermore, the insulator phase was recognized as the Mott insulator phase, due to this phase corresponds to an incompressible phase.

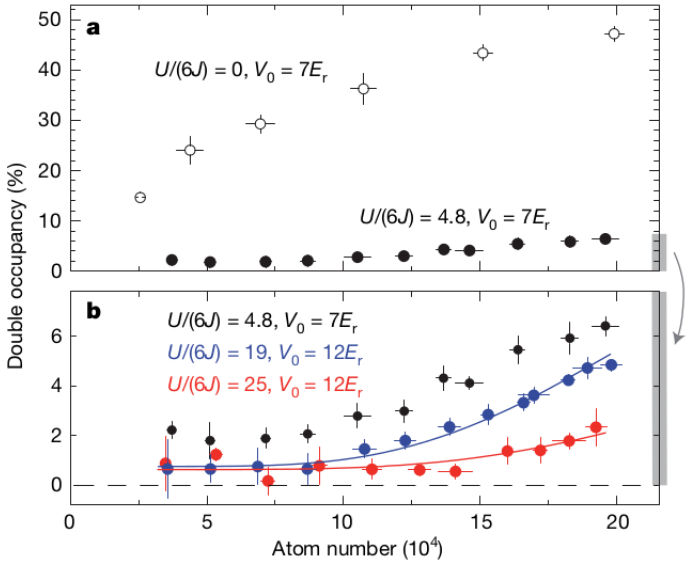

FIGURE 1.6. Double occupancy as a function of total atom numbers in the lattice for different values of on-site interaction U measured with respect to the hopping amplitude (here J). (**a**) Double occupancy for strong and weak coupling limit (black and white circles respectively), (**b**) Zoomed behavior for the strong coupling limit, here the solid red and blue lines represent the theoretical approach for D assuming full localization of atoms, i.e., neglecting the kinetic energy. From [JrSGn$^+$08].

In fact, this can be seen from the slope of the double occupancy $\partial D/\partial N$ in the FIGURE 1.6. This quantity is an indirect measure of compressibility $\kappa = \partial n/\partial \mu$, since the filling n increase with D. More than the antiferromagnetic order in the insulator phase, a Mott-insulator have several unique characteristics as a null compressibility[GFW$^+$06]. In the weak regime, the system is compressible due to the slope $\partial D/\partial N$ is positive, but in the strong coupling limit ($U/h > 5kHz$), the slope vanish indicating that the system has entered to the Mott insulator phase (see FIGURE 1.7). This behavior agrees well with the result expected from the Hubbard model in the atomic limit, i.e., when the kinetic energy is neglected (see solid lines in FIGURE 1.6-**b** and FIGURE 1.7).

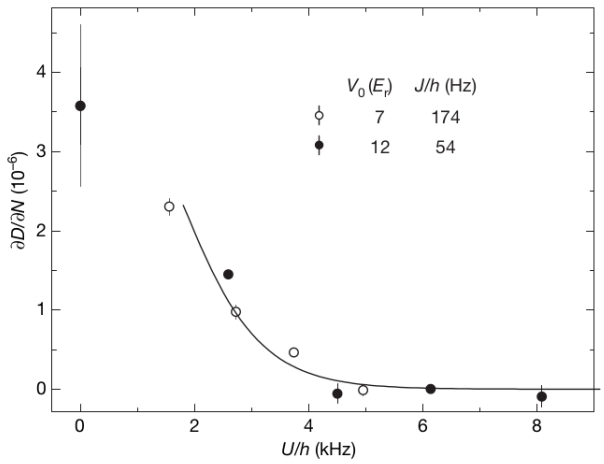

FIGURE 1.7. Slope $\partial D/\partial N$ as a function of U/h (here, h is Planck's constant). The compressibility $\partial D/\partial N$ was obtained from a least-squares fit of $D(N) = (\partial D/\partial N)N + D_0$ to the data in FIGURE 1.6. The solid line represents the expected value of $\partial D/\partial N$ in the atomic limit (neglected kinetic energy). From [JrSGn+08].

Although the smooth decay of the $\partial D/\partial N$ in the FIGURE 1.7 indicates a continuous phase transition in the system, the criticality of this transition depends strongly on the dimension and geometry of the lattice. For instance, a phase transition belonging to the Heisenberg universality class was predicted in the three-dimensional model at half filling [Kar13], meanwhile for the two-dimensional model several researches suggest that the transition can belong to the $3D$ XY universality class in a triangular lattice [Sen08], $2D$ Ising universality class [ME12] in a square anisotropic lattice or even Gross-Neveu-Heisenberg universality class in a honeycomb lattice [PTHAH15]. Besides, in the one-dimensional model, the phase transition corresponds to the Berezinskii-Kosterlitz-Thouless (BKT) transition [BLSS07].

Despite there is not an exact solution for the Hubbard model in two or higher dimensions, which will allow a fundamental description of the phases near a MI transition and the criticality of this transition, the study interacting spin mixtures in optical lattices with different geometries provide a good framework to explore the Hubbard model physics and other engaging phenomena. In the following sections, we will remark this idea in two particular examples: the Hubbard model in honeycomb lattices and the mass-imbalanced Hubbard model.

1.4 Hubbard model in a honeycomb lattice

About the study of complex geometries in optical lattices, an interesting system is the honeycomb lattice. This kind of lattice has been widely studied since the discovery of graphene [NGM+04] due to current applications of this material in electronics [FBI+14], spintronics [HKGF14], development of high-frequency and logic transistors [MMF+18, MRPM+20], among others [RVPS15, XWX+14]. However, although the pure graphene presents engaging topological features like Dirac points, the absence of a gap energy is an obstacle for some already mentioned applications.

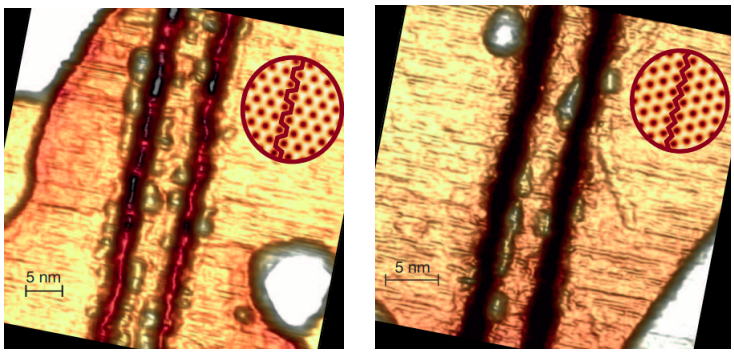

FIGURE 1.8. Crystallographic edge orientations in graphene nanoribbons fabricated by scanning tunnelling microscope lithography: (**a**) Armchair orientation, (**b**) Zigzag orientation. From [MJH+14].

One way to get a non-zero gap in graphene consists of achieve an electronic confinement in narrow strips. These strips, called as graphene nanoribbons, can be fabricated by techniques based on scanning tunneling obtaining ribbons with nanometric widths and well-defined edge orientation [TDLB08, MJH+14], as we can see in FIGURE 1.8. Due to the narrow width of these ribbons, an electronic gap up to 0.5 eV emerges in both possible orientations of the edge (armchair and zigzag).

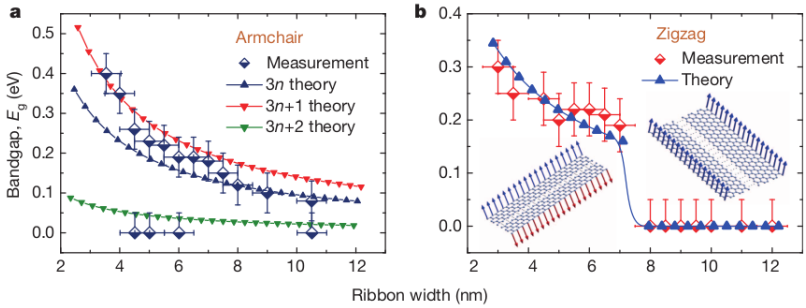

FIGURE 1.9. Experimental and theoretical width dependence of the energy gap in graphene nanoribbons for the two possible edge orientation: (**a**) armchair, (**b**) zigzag. Theoretical data correspond to density functional theory for armchair ribbons depending on the number of rows in the ribbon ($3n$, $3n+1$ and $3n+2$, being $n = 1, 2, 3\cdots$), and from mean field Hubbard model approach for zigzag ribbons (solid lines are just a guide for the eye). From [MJH+14].

Indeed, in the FIGURE 1.9, we can observe the experimental and theoretical results of G. Z. Magda *et al.* about the dependence of the energy gap with respect to the width in nanoribbons fabricated by scanning tunneling microscopy (STM) [MJH+14]. For armchair as well as zigzag nanoribbons, the electronic gap decreases with the width of the ribbon. However, this behavior is different depending on the edge orientation. Meanwhile, the gap continuously decreases in armchair graphene nanoribbons (AGNR), there is a discontinuity in the gap function for zigzag graphene nanoribbons (ZGNR). This indicates a transition between a semiconductor phase and a metal phase (zero gap phase) when the edges have a zigzag orientation.

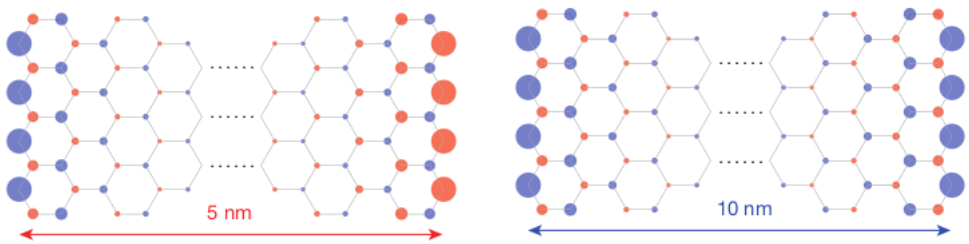

FIGURE 1.10. Mean field results for the spin density (red: spin up, blue: spin down) in ZGNR for a 5 nm strip (left) and 10 nm (right). From [MJH+14].

This transition observed by Magda and its coworkers is also predicted correctly by themselves from a mean field approach of the Hubbard model (blue triangles in FIGURE 1.9**b**). This forecast relates directly the gap opening in ZGNR with the correlation between the confined electrons in the ribbons, since this correlation is the fundamental reason for the insulator phase in the Hubbard model. Besides, from the same mean field calculations, a magnetic order in the semiconductor phase as well as in the metallic phase of the ZGNR was predicted by means of analyzing the spin density along the ribbons given by the following expression:

$$\langle S_z(\mathbf{r})\rangle = \frac{1}{2}\left(\langle n_\uparrow(\mathbf{r})\rangle - \langle n_\downarrow(\mathbf{r})\rangle\right),$$

where $\mathbf{r}$ is a position vector lying to the lattice and $n_\uparrow(\mathbf{r})$ ($n_\downarrow(\mathbf{r})$) is the particle density with spin up (spin down) at the site $\mathbf{r}$. Specifically, an antiferromagnetic order is predicted for semiconductor ribbons (narrow ribbons in left side of FIGURE 1.10), meanwhile a ferromagnetic order is predicted for the metallic ones (wide ribbons in right side of FIGURE 1.10).

The existence of an antiferromagnetic order in the gapped phase of ZGNR is also related with the interaction between the confined electrons in the ribbon. In fact, numerical approaches beyond the mean field of G. Z. Magda *et al.*, demonstrate that an antiferromagnetic insulator phase is presented in narrow ribbons of a honeycomb lattice with Hubbard's interaction [HHLM03, HL16]. For instance, the FIGURE 1.11 shows the spin density in a narrow ribbon calculed by Density Matrix Renormalization Group (DMRG) algorithm performed by I. Hagymási and Ö. Legeza [HL16], where a clear antiferromagnetic order is observed for a non-null interaction parameter (FIGURE 1.11**b**).

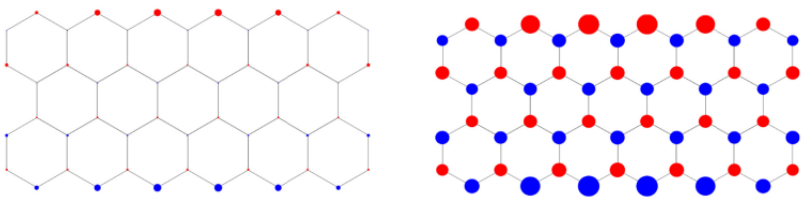

a **b**

FIGURE 1.11. DMRG results for spin density (red: spin up, blue: spin down) in ZGNR: (**a**) $U/t = 0$, (**b**) $U/t = 4$. From [HL16].

Moreover, this antiferromagnetic ground state in ZGNR is consistent with the Lieb's Theorem[Lie89] about the repulsive Hubbard model at half-filling for bipartite lattices which states that *the ground state is unique*[11] *and has a total spin* $S = \frac{1}{2}||B| - |A||$*, where* $|B|$ $(|A|)$ *is the number of sites in the B (A) sublattice.* Since $|B| = |A| = 3$ for the honeycomb lattice, the theorem predict a unique ground state with $S = 0$. According to this, the insulator phase in ZGNR must be a singlet state with a finite spin gap, which is an example of the second type of insulators near to the MI transition discussed in the Section 1.1.

Indeed, this feature also was predicted by numerical approaches as the DMRG exploration done by T. Hikihara *et al.* [HHLM03] in 2003. In this investigation, the ground-state properties of ZGNR with Hubbard interaction were studied by analyzing the spin density, spin correlations functions as well as the spin and charge gaps. The spin and charge gaps, denoted by Δ_S and Δ_C respectively, are defined as follows:

$$\Delta_S = E_0(N_\uparrow + 1, N_\downarrow - 1) - E_0(N_\uparrow, N_\downarrow), \tag{1.7}$$

$$\Delta_C = E_0(N_\uparrow + 1, N_\downarrow) + E_0(N_\uparrow - 1, N_\downarrow) - 2E_0(N_\uparrow, N_\downarrow). \tag{1.8}$$

where $E_0(N_\uparrow, N_\downarrow)$ is the ground state energy of the system with $N_\uparrow$ spin up electrons and $N_\downarrow$ spin down electrons. In FIGURE 1.12, we can see that there is non-zero spin gap (white squares) for positive on-site interaction parameter.

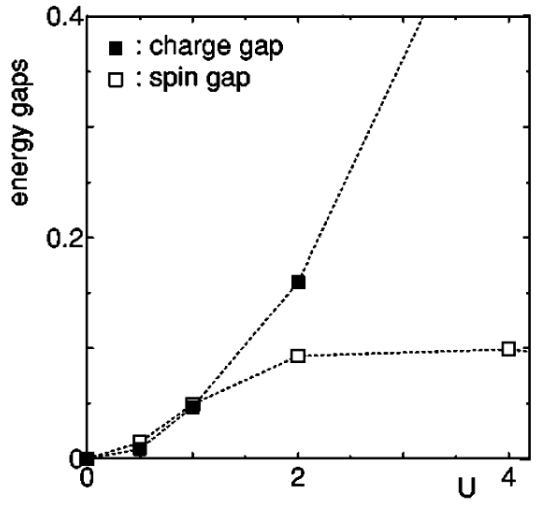

FIGURE 1.12. Spin and charge gaps at thermodynamic limit for a narrow ZGNR (with just one hexagon of wide) as a function of the on-site interaction parameter U of the model. From [HHLM03].

To conclude, the magnetic properties of the insulator/semiconductor ground state of ZGNR are very interesting quantum characteristics that could be important to future applications in spintronics [HKGF14] and other fields already mentioned at the beginning of this section. Also, the implementation of honeycomb geometry in tunable geometry optical lattice [TGU+12] allows for a detailed exploration of this magnetic properties.

[11] except for the typical $2S + 1$ degeneracy

1.5 Mass-imbalanced Hubbard model

In regard to the emerged physics of systems with spin mixtures, currently the possibility of trap different types of atoms in an optical lattice [TVA$^+$08, STN$^+$09, TGL$^+$10] allows for the study several phenomena. In particular, phenomena like Fulde, Ferrell, Larkin, and Ovchinnikov (FFLO) superconductivity [TU08, CP18], fermionic superfluity [OPS08] or atom-dimer attraction [JZC$^+$14] can be studied in lattices loaded with an interacting Fermi mixtures. According to the recent researches, all these phenomena seem to be related with an imbalance in the spin mixtures.

As we mentioned in Section 1.3, a spin mixture can be a heteronuclear mixture, where the difference between the total number of atoms loaded into the optical lattice or the difference between the masses of them leads respectively to a population-imbalance or a mass-imbalance in the system. On the one hand, in a population-imbalanced ultracold gas, the finite magnetization of the ground state cause that an s-wave superconductor state would not be possible[12] [FF64, LO64], giving place to engaging phenomena like the already mentioned FFLO superconductivity. On the other hand, a spin mixture with mass-imbalance exhibits an asymmetry in the kinetic energy of particles with different spin, which favors energetically a superfluid state when the confining potential of one of the atomic species in the mixture goes out [OPS08].

Moreover, mass-imbalanced mixtures are related with localization phenomena like the localized magnetic moments in *samarium hexaboride* (SmB_6) which are connected with the semiconductor-metal transition in this material[MBG69, FK69]. As well as the metal-insulator transition in others transition-metal oxides, the transition in SmB_6 can be studied by a Hubbard model. However, the model that describe this material corresponds to a modification of the Hubbard model.

In the model proposed by L. M. Falicov and J.C. Kimball [FK69] to describes the samarium hexaboride, it is assumed that the localized magnetic moments interact with spinless electrons. This is equivalent to consider interacting electrons where for example the electrons with spin $\uparrow$ has an infinite mass (a limit case of mass-imbalance). According to this, the Falicov-Kimball Hamiltonian can be written as follows [GIJL90, KL86]:

$$H_{MI} = \sum_{\langle i,j\rangle,\sigma} t_\sigma \left(c^\dagger_{i,\sigma} c_{j,\sigma} + c^\dagger_{j,\sigma} c_{i,\sigma} \right) + U \sum_i n_{i,\uparrow} n_{i,\downarrow}, \tag{1.9}$$

with $t_\uparrow = 0$ and $t_\downarrow = t$. The ground state of this Hamiltonian exhibits interesting properties [KL86] as a positive gap at half-filling for all $U \neq 0$ (as well as in the insulator phase of the Hubbard model) and a long range order for all dimensions d at zero temperature, which persists for $d \geq 2$ at finite small temperature. This long range order is related with the phenomena of crystallization of the matter that gives an alternative explanation of why a periodic arrangement of nuclei is the configuration of minimum energy.

Although the insulator phase of the Falicov-Kimball model (FK model) is very similar to the insulator phase to the Hubbard model, these phases are fundamentally different in one dimension. Even more, the correlated insulator of any mass-imbalanced chain differs

[12] Since the cooper paring between particles with opposite spin can not occur for an arbitrary weak coupling.

from Mott insulator phase of the Hubbard model, since that insulator exhibits a finite spin gap [FDanLan95]. In fact, for the strong coupling limit the Hamiltonian (1.9) can be mapped to an anisotropic XXZ Heisenberg chain given by the following Hamiltonian [GMJ16]:

$$H_{XXZ} = J \sum_i S_i^x S_{i+1}^x + S_i^y S_{i+1}^y + \gamma S_i^z S_{i+1}^z,$$

being S_i^x (resp. S_i^y, S_i^z) the x (resp. y, z) component of an effective $\frac{1}{2}$-spin operator[13] at site i, $J = 4t_\uparrow t_\downarrow/U$ and $\gamma = (t_\uparrow^2 + t_\downarrow^2)/2t_\uparrow t_\downarrow$. Since $J > 0$ and $\gamma > 1$[14] when there is mass-imbalance, the ground state of the system is antiferromagnetic and has a finite spin gap cause by the asymmetry parameter γ [DCG66].

This particular difference, in the spectrum of the ground state of the Hubbard model and mass-imbalanced Hubbard model at one dimension, suggest that a phase transition between the two correlated insulators occurs. According to Bethe Ansatz approach of the XXZ Heisenberg chain, the spin gap open right when there is not mass-imbalance, i.e. at $\gamma = 1$ ($t_\uparrow = t_\downarrow$). Moreover, this gap opens exponentially slow near to the phase transition point as follows [DCG66]:

$$\Delta_S = 4\pi J \exp\left\{-\pi^2/[2(2(\gamma-1))^{1/2}]\right\},\ 1 < \gamma \leq 2,$$

which is characteristic of a BKT transition. For the weak coupling limit, this transition remains, but does not occur at the balanced point $t_\uparrow = t_\downarrow$ [CG08]. Finally, the quantum criticality of the mass-imbalance model at two or higher dimensions is a very interesting topic[SCH12, GUJ$^+$13]. Mostly, away from the half-filling, there are rich phase diagrams of the model that include charge and spin density wave orders, phase separation, super solid phase, between others engaging phases [SVFF07, Mat07, Fcv08, BCD$^+$10, Far12].

[13] The spin operators are given by:

$$S_i^\alpha = \sum_{\mu,\nu} c_{i,\mu}^\dagger \sigma_{\mu,\nu}^\alpha c_{i,\nu},$$

where $\sigma_{\mu,\nu}^\alpha$ are the Pauil matrices with $\alpha = x, y, z$.

[14] As $(t_\uparrow - t_\downarrow)^2 = t_\uparrow^2 + t_\downarrow^2 - 2t_\uparrow t_\downarrow > 0$

CHAPTER 2

Ionic Hubbard Model

In the previous chapter, we have seen how the experimental realization of a fermionic Mott-insulator on optical lattices motivated the theoretical and numerical research of several many-body phenomena in the context of the Hubbard Hamiltonian. In this chapter, we focus in a particular Hubbard Hamiltonian called the ionic Hubbard model (IHM) which describes interacting electrons in a staggered potential. We give a brief theoretical and experimental review of the model in one and two-dimensional lattices, centering our attention in the honeycomb lattice that is the main frame of this thesis. Also, we present the results of a transversal research about the mass-imbalanced IHM made during the development of this project.

2.1 Origins of Ionic Hubbard Model (IHM)

The ionic Hubbard model is a modification of the Hubbard model proposed by Paul J. Strebel and Zoltán G. Soos in 1970 [SS70] to describe the effects of charge transfer (CT) interaction in stacks of electron donors and acceptors in aromatic crystals. This interaction has an electrostatic origin, caused by a transferred fraction of electric charge between two or more molecules.

Donor (D) molecules are characterized by a low ionicity potential, meanwhile an acceptor (A) ones are characterized by a high electron affinity. Those features lead the D and A molecules, like Tetrathiafulvalene (TTF) and chloranil respectively, to stack together face to face (see FIGURE 2.1-**a**) due to two kinds of interactions [Mul54, Soo74]. The first one corresponds to the typical intermolecular forces, i.e., forces caused by some electrostatic interaction between multipole moments (London dispersion forces for example). The other interaction (the CT interaction) is caused when a fraction of the electronic charge is transfered from D to A leading to an attractive electrostatic force between the molecules. According to this, a DA complex can take two possible states: one where the molecule has not a net electric charge (neutral state, see FIGURE 2.1-**b**) and other where a pair DA is ionized D^+A^- due to the charge transfer (ionic state, see FIGURE 2.1-**c**).

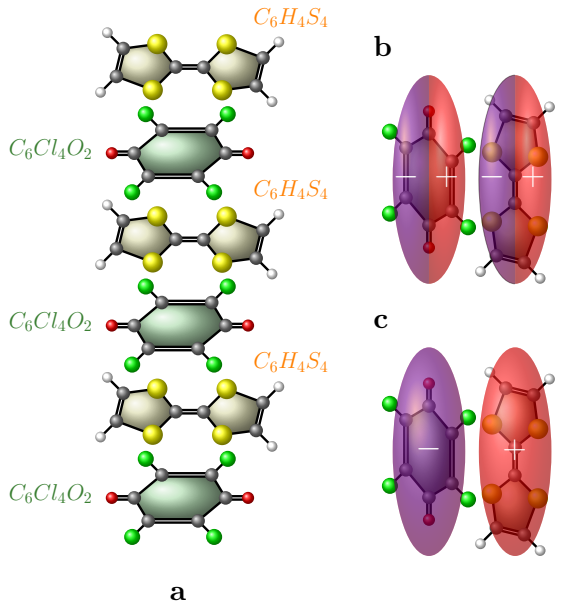

FIGURE 2.1. Charge-Transfer complex example: (**a**) Molecular structure of TTF-Chloranil, (**b**) neutral phase of the CT complex, (**c**) ionic phase of the CT complex. Gray, green, red, yellow and white spheres represent C, Cl, O, S and H atoms respectively and the single and double lines represent the single and double bonds between the atoms.

The occurrence of those states in an organic charge-transfer complex suggest the presence of a phase transition between a neutral phase and an ionic phase. In fact, J.B. Torrance *et al.* in 1981 [TVML81] reported the first observation of a neutral-to-ionic transition in organic charge-transfer solids. This transition is characterized by a competition between the ionizing energy of a DA pair, and the electrostatic repulsion between two electrons in the same molecule.

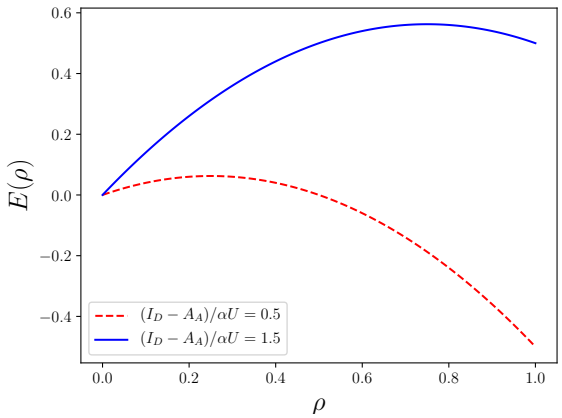

FIGURE 2.2. Total energy of a DA pair in a CT complex as a function of ρ. The solid and dashed line corresponds to the energy in the neutral and ionic phase, respectively.

Indeed, let I_D be the ionizing potential of the D molecule, A_A be the electron affinity of the A molecule and U the Coulomb attractive interaction energy. Then, the total energy of the DA pair is given by [Soo74]

$$E(\rho) = (I_D - A_A)\rho - \alpha U \rho^2, \tag{2.1}$$

where ρ is the degree of CT and α is the Madelung constant of ionic pair D^+A^-. Thus, if $I_D - A_A > \alpha U$, the ionized DA pair is not a stable state, causing the solid to fall into the neutral phase ($\rho = 0$). Otherwise, if $I_D - A_A < \alpha U$, the ionized state ($\rho = 1$) minimized the pair energy (2.1) causing the solid to be in the ionic phase. We can observe this from a plot of the DA energy (2.1) as a function of ρ (see FIGURE 2.2).

As we mentioned, this phenomenon was described theoretically by Strebel and Soos in 1970. They describe the CT complex as a quantum mechanical systems characterized by a modified Hubbard model:

$$H_{ionic} = -t \sum_i c^\dagger_{i\sigma} c_{i+1\sigma} + U \sum_i n_{i,\uparrow} n_{i,\downarrow} + H_{site} + H_\alpha, \tag{2.2}$$

where H_{site} and H_α are a phenomenological description of the on-site energy representing the inequivalence of D and A molecules and the energy difference between the three-dimensional lattice of D^+, A^- ions and of D, A molecules respectively. On the one hand, the first term introduces an energy difference (sometimes called *staggered energy offset*) between odd and even sites of the chain as follows:

$$H_{site} = \Delta \sum_{i,\sigma} (-1)^i n_{i\sigma}. \tag{2.3}$$

Since all the electrons are paired on the D molecule in the neutral phase, H_{site} gives a -2Δ energy for a DA pair, meanwhile in the ionic phase this site contribution vanishes. Thus, the excitation energy to create an ionic pair from the neutral phase is 2Δ. Such energy can be estimated as [NSM66, SS70]

$$2\Delta = (I_D - A_A) + U,$$

because it is exactly the energy to transfer one electron from the donor to the acceptor molecule. According to this and equation (2.1), the neutral phase occurs for $2\Delta > (1+\alpha)U$, meanwhile the ionic phase occurs for $2\Delta < (1+\alpha)U$. On the other hand, the H_α term is given by:

$$H_\alpha = -\frac{2\alpha}{L} \left\langle \sum_{i,\sigma}{}' n_{i,\sigma} \right\rangle^2, \tag{2.4}$$

where the sum goes over the acceptor sites and L is the total number of molecules in the chain. This term represents the total molecular Madelung energy in the ionic phase [SS70, KMM64].

2.2 One-dimensional IHM

The Madelung term (2.4) is just included to take into account the three-dimensional distribution of the D^+A^- pair in the ionic phase. Due to this, the main cause of the neutral-to-ionic phase transition is related to the competition between U and Δ energies. Thus, the Hamiltonian that describes the phase transition in the IHM is the following :

$$H_{ionic} = -t\sum_i c^\dagger_{i\sigma}c_{i+1\sigma} + U\sum_i n_{i,\uparrow}n_{i,\downarrow} + \Delta\sum_{i,\sigma}(-1)^i n_{i\sigma}. \tag{2.5}$$

The competition between energy scales in the IHM gives rise to very interesting phenomena: an insulator-insulator transition, which had been one of the hardest and engaging problems in condensed matter physics[TAJN06, MCFSV16]. For example in a one-dimensional lattice, according to bosonization calculations[FGN99], two critical points of U were predicted for a fixed value of Δ such that an ionic Hubbard chain has first a band insulator phase for $U < U_{c_1}$ characterized by a non-zero band gap, followed by an Ising-like phase transition to an intermediate phase for $U_{c_1} < U < U_{c_2}$ where the band gap is zero and some kind of dimerization appears in the lattice, and finally a BKT transition to a correlated Mott-insulator $U > U_{c_2}$ characterized by a peculiar particle ordering (see FIGURE 2.3).

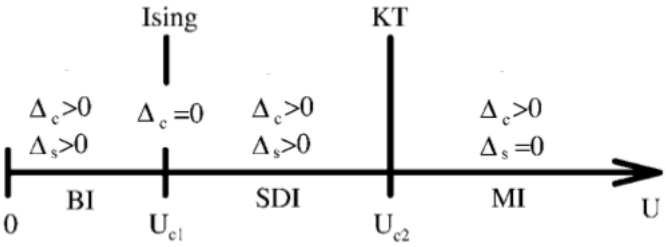

FIGURE 2.3. One-dimensional ionic Hubbard model phase diagram: Band insulator (BI) for $U < U_{c_1}$, spontaneously dimerized insulating phase (SDI) for $U_{c_1} < U < U_{c_2}$ and Mott-insulator for $U > U_{c_2}$. From [FGN99].

In 2004 S. R. Manmana *et al.* [MMNS04] studied numerically the insulator-insulator phase transition of the ionic Hubbard model in one dimension. In this work, the authors calculated the charge ($\Delta_1 = \Delta_C$), spin and excitation gap[1] (Δ_E) determining the exact critical points of the two phases transitions. In the figure 2.4 is shown the gap energies for an ionic Hubbard chain as a function of U/t for a fixed value of $\Delta/t = 10$ at the

[1]the excitation gap is given by:

$$\Delta_E = E_1(N_\uparrow, N_\downarrow) - E_0(N_\uparrow, N_\downarrow),$$

where $E_1(N_\uparrow, N_\downarrow)$ is the first excited state energy.

thermodynamic limit. The band insulator phase is characterized by a non-zero value of the excitation gap Δ_E. The phase transition to the intermediate phase occurs when $\Delta_E = 0$, the authors report $U_{c_1}/t = 21.39$ for this transition. The second transition to Mott-insulator phase is characterized by a null value of the spin gap at $21.55 < U_{c_2}/t < 21.69$.

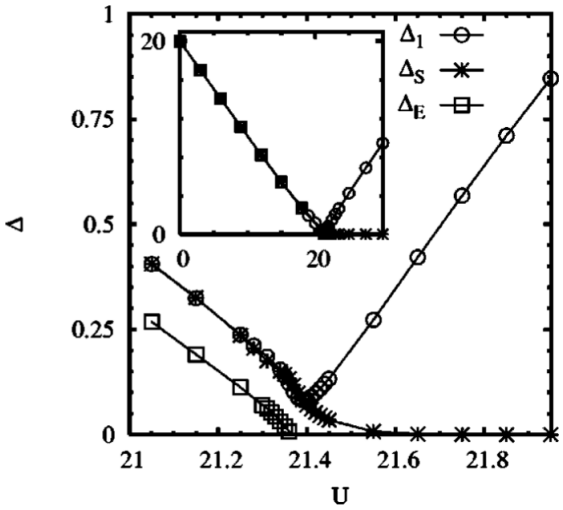

FIGURE 2.4. The U dependence of gaps energy at the thermodynamic limit for an ionic Hubbard chain with $\Delta/t = 10$. The inset shows the behavior of gaps for a large range of U. From [MMNS04].

The band insulator and Mott-insulator phases can be described considering two limit cases of the IHM: the limit of weak coupling ($U \ll \Delta, t$) and the limit of strong coupling ($U \gg \Delta, t$). In the first limit, which belongs to the band insulator phase, the ground state exhibits a charge modulation as it is shown in FIGURE 2.5-**a**, where particles with different spin tend to stay together in deeper potential well sites. This modulation, called charge density wave (CDW), occurs since the particles can not tunnel to shallow potential well sites, due to the high value of energy offset. We must note that this phase corresponds to the neutral phase of the system, where there is no charge transfer between donors and acceptors[2].

Now, in the other limit (which corresponds to the Mott-insulator), the strong on-site interaction causes that particles with different spin can not be in the same site, leading to a charge transfer in the system (characteristic of ionic phase). Due to this, there is an occupation of one particle per site along the lattice with an antiferromagnetic order, as we can see in the FIGURE 2.5-**c**. In fact, the lattice presents an antiferromagnetic order since the IHM in the strong coupling limit is equivalent to an effective Heisenberg model with an antiferromagnetic ground state [GMJ16]:

$$H_{eff} = J \sum_i \mathbf{S}_i \cdot \mathbf{S}_{i+1},$$

where $\mathbf{S}_i = (S_i^x, S_i^y, S_i^z)$ is the spin operator at site i, and $J = 4t^2U/(U^2 - \Delta^2)$.

[2]Here, the donors are in the sites with more deep potential well.

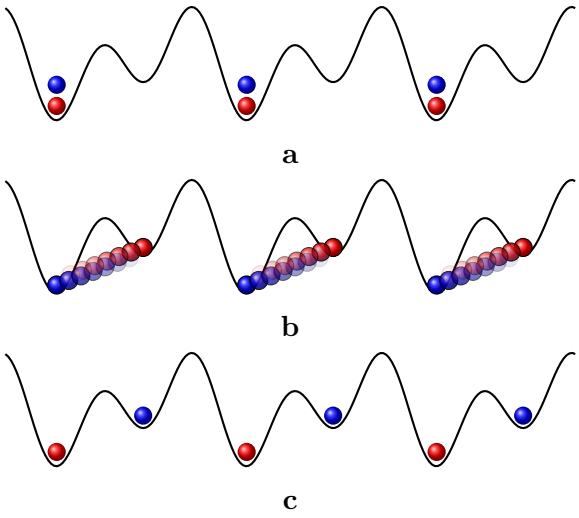

FIGURE 2.5. Sketch of phases in the IHM in one-dimension: (**a**) band insulator phase for weak coupling limit, (**b**) spontaneous dimerized intermediate phase, (**c**) Mott-insulator for strong coupling limit. The red (resp. blue) spheres represent particles with spin up (resp. spin down).

In regard to the intermediate phase, according to the previous mentioned theoretical and numerical studies [FGN99, MMNS04], this is a phase different to the neutral and ionic phases of the CT complexes which is characterized by a dimerization in the chain. For instance, in the work of S. R. Manmana *et al.*, the intermediate phase is described by the so called *bond-order* (BO) parameter, given by:

$$\langle B \rangle = \frac{1}{L-1} \sum_{i,\sigma} (-1)^i \left\langle c^\dagger_{i+1,\sigma} c_{i,\sigma} + c^\dagger_{i,\sigma} c_{i+1,\sigma} \right\rangle,$$

being L the total number of sites in the lattice. This quantity has been used to study dimerized phases in other systems [WA96], and in particular for the IHM, allows to determine if there exists an asymmetry in the hopping probability between sites with deep and shallow potential well.

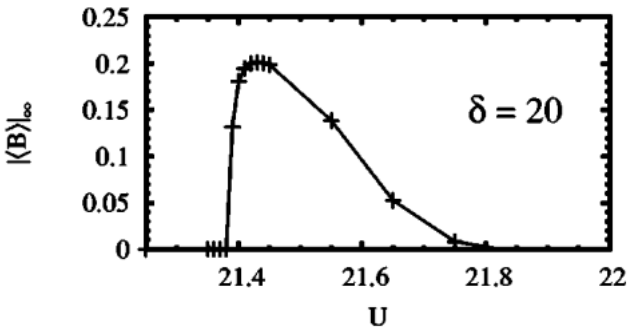

FIGURE 2.6. Bond-order parameter at the thermodynamic limit as a function of local interaction in a one-dimensional lattice for a fix energy offset $\delta = 2\Delta = 20$. From [MMNS04].

As we can see in the FIGURE 2.6, the BO parameter is positive in the limit $L \to \infty$ for the intermediate phase studied by S. R. Manmana *et al.* for a fixed energy offset $(\Delta/t = 10)$[3]. Thus, the intermediate phase corresponds to a dimerized state of the chain, as it is shown in the FIGURE 2.5-**b**. We must note that the BO parameter is zero in the band insulator phase as well as in the Mott-insulator phase, since for those phases the particles occupy a fix site.

2.3 Two-dimensional IHM and Optical Lattices

About of current researches around of IHM, in 2015 M. Messer *et al.* [MDU$^+$15] successfully studied the IHM model in an optical lattice loaded with a balanced mixture of ^{40}K atoms. In this experiment, the two-component fermionic gas is confined into a honeycomb lattice created using three laser beams $X, Y, \bar{X}$ of wavelength $\lambda = 1064$nm. The beams X and Y are perpendicular, meanwhile the beam $\bar{X}$ is collinear with X but detuned by a frequency δ (see FIGURE 2.7-**a**). The bipartite honeycomb lattice displayed in the FIGURE 2.7-**b** is obtained by fixing the relative intensities of beams, which create the honeycomb geometry, and varying the detuning frequency δ in order to introduce the energy offset Δ between the two sites A and B of the unit cell.

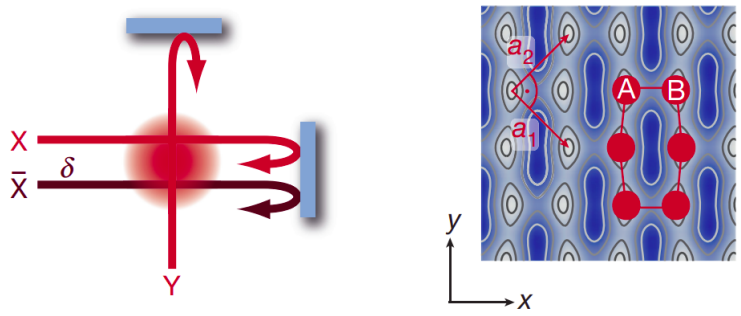

a **b**

FIGURE 2.7. Optical lattice used by M. Messer *et al.* to explore the IHM in two dimension. (**a**) Laser beams disposition, (**b**) Honeycomb lattice with an energy offset between sites A and B of the unit cell. From [TGU$^+$12].

As one result of this investigation, M. Messer *et al.* observed that the double occupancy D in the lattice is suppressed as the local interaction increases, as we can see in FIGURE 2.8-**a**. The fraction of double occupied sites was measured, like in the previous work of R. Jördens *et al.* [JrSGn$^+$08] by radio-frequency spectroscopy for attractive and repulsive interaction between the atoms loaded into the lattice. For attractive and weak repulsive interaction, the double occupancy is positive, as expected for the CDW phase of the IHM. However, the value of D decreases as a function of U/t until it vanishes for strong repulsive interaction, indicating a transition from the CDW phase to another insulator phase (Mott-insulator phase or similar). Although, in the M. Messer's experiment the CDW phase and a metallic phase for $U = 4.85(9)t$ and $\Delta = 0.00(4)t$ (see FIGURE 2.8-**b**) was confirmed in the system, by analyzing the correlations of fluctuations (noise correlations), they can not determine the existences of an intermediate phase like in the one-dimensional IHM.

[3] $\delta = 2\Delta$ in FIGURE 2.6.

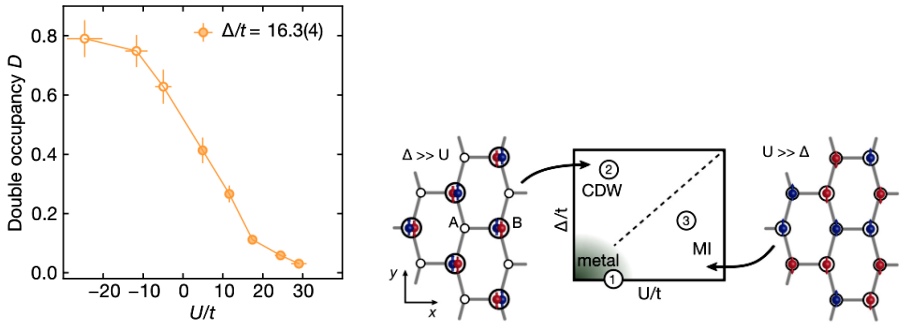

a **b**

FIGURE 2.8. Results of M. Messer's experiment. (**a**) Fraction of double occupied sites D as a function of local interaction U for a fix energy offset ($\Delta/t = 16.3(4)$), (**b**) Sketch of phase diagram of the IHM on a honeycomb lattice at half-filling. Hollow (resp. full) circles in figure (**a**) represent attractive (resp. repulsive) interaction between the atoms. From [MDU+15].

The nature of an intermediate phase between the CDW phase and the Mott-insulator phase in two dimension has been theoretically debated. For square lattices[4], studies of IHM using dynamical mean-field theory (DMFT) and quantum Monte Carlo (QMC) predict a metallic intermediate phase [PBH+07, SE19b]. However, others numerical approaches suggests a different nature of this phase including a spin density wave (SDW) [CZLW10], a metastable d-wave superconductor [CBKG19] or even an insulating phase with a bond order similar to the one-dimensional lattice [KD07].

In regard with the honeycomb lattice, a DMFT study done by Lin HF *et al.* [LLTL15] in 2015 suggests that there is no intermediate phase at half-filling. In this research, they study the phase transition of the IHM on a honeycomb at half-filling and out of it, considering a hole doping case. About the half-filling phase transition, they identify a phase transition between a band insulator and an antiferromagnetic insulator by analyzing the double occupancy and staggered magnetization given by:

$$D = \frac{1}{L} \sum_{\mu=(i,j)\in A,B} \langle n_{\mu,\uparrow} n_{\mu,\downarrow} \rangle, \tag{2.6}$$

$$M_s = \frac{1}{L} \sum_{\mu=(i,j)\in A,B} sgn(\mu)(n_{\mu,\uparrow} - n_{\mu,\downarrow}), \tag{2.7}$$

where L is the total number of sites in the lattice, and $sgn(\mu) = 1$ (resp. $sgn(\mu) = -1$) if the site $\mu = (i,j) \in B$ (resp. $\mu = (i,j) \in A$). These two quantities as a function of local interaction for different energy offset are shown in FIGURE 2.9. On the one hand, the fraction of double occupied sites is always decreasing as a function of local interaction indicating a CDW phase for weak interaction, as expected for the phase transition from band insulator toward Mott-insulator in the IHM. On the other hand, the staggered magnetization is zero for some U values depending on the energy offset and becomes positive for a critical value of U_c/t. This predicts that for strong local interaction ($U > U_c$), the system presents an antiferromagnetic order. Since, the staggered magnetization turns pos-

[4] A similar metallic intermediate phase was predicted in Bethe lattices [GKR06, BGK15]

itive suddenly, there is no evidence of an intermediate phase between the band insulator phase and the antiferromagnetic insulator phase.

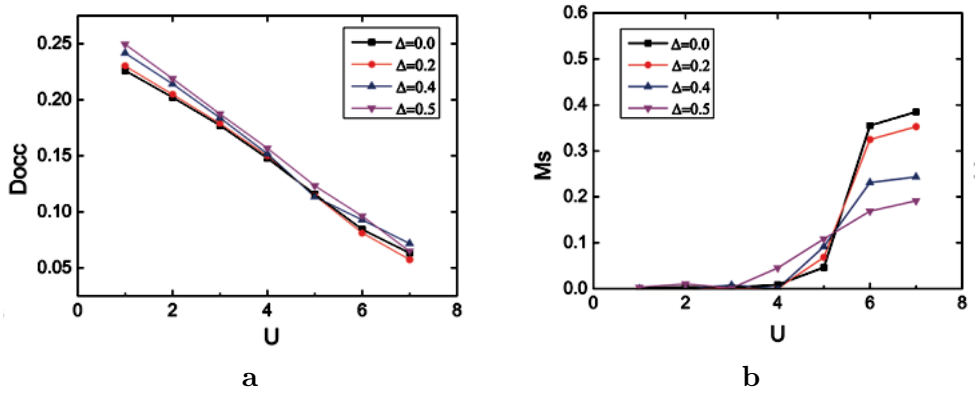

FIGURE 2.9. Lin HF's DMFT results for the IHM on a honeycomb lattice. (**a**) Double occupancy ($Docc = D$) as a function of local interaction for different values of energy offset, (**b**) staggered magnetization as a function of local interaction for different values of energy offset. From [LLTL15].

2.4 IHM with Mass-imbalance

Another scenario of the IHM that it is currently interesting is the mass-imbalanced case. As we mentioned in the Section 1.5, the possibility to load different types of atoms into an optical lattice allows to study engaging phenomena like superconductivity, fermionic superfluity or atom-dimer attraction. In the mass-imbalanced IHM, particularly, it is interesting to inquire about the insulator-insulator transition of the model and the nature of the possible intermediate phase.

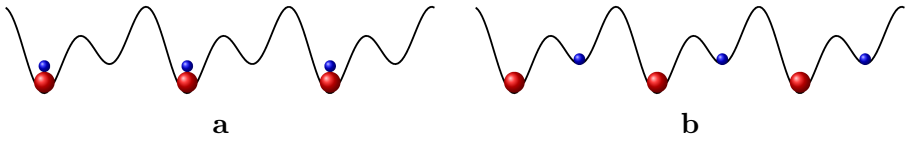

FIGURE 2.10. Sketch of expected phases of the IHM with mass-imbalance on a one-dimensional lattice. (**a**) CDW phase for weak coupling limit ($U \ll \Delta$), (**b**) antiferromagnetic insulator phase for strong coupling limit ($U \gg \Delta$). The red and blue spheres represent the particles with spin up and down, respectively, and its radius represents the mass-imbalance between the two species of atoms in the lattice. From [PGFSV21].

The mass-imbalanced IHM is defined by the Hamiltonian:

$$H_{IMI} = -\sum_{\langle i,j\rangle,\sigma} t_\sigma \left(c^\dagger_{i,\sigma}c_{j,\sigma} + c^\dagger_{j,\sigma}c_{i,\sigma}\right) + U\sum_i n_{i,\uparrow}n_{i,\downarrow} + \Delta\sum_{i,\sigma}(-1)^i n_{i\sigma}. \tag{2.8}$$

As in the balanced version of the model at half-filling, a band insulator with a CDW and an antiferromagnetic insulator is expected for the weak and strong coupling limit respectively. Indeed, for the limit where $U \ll \Delta$, the particles in the system can not tunnel to sites

with shallow potential well, due to the high value of the energy offset. We must note that this fact is true independently of the spin of the particles, since in this limit the particles with spin up, as well as with spin down, tend to occupy the sites with deep potential well (see FIGURE 2.10-**a**). For the limit where $U \gg \Delta$, particles with different spin can not occupy the same site leading to an insulator phase with one particle per site (see FIGURE 2.10-**b**).

Although in one-dimension, the insulator phase for the strong coupling limit seems to be similar to the Mott-insulator of the ionic Hubbard chain. The mass-imbalance introduces an asymmetry in the spin sector (since the $SU(2)$ symmetry of the model is broken) causing a difference in the spectrum of these phases. We can see this from a perturbative treatment of the Hamiltonian (2.8), where like the mass-imbalance Hubbard model (1.9), the IHM with mass-imbalance is equivalent to the following effective Heisenberg Hamiltonian [GMJ16]:

$$H_{ionic-eff} = J \sum_i S_i^x S_{i+1}^x + S_i^y S_{i+1}^y + \gamma S_i^z S_{i+1}^z - h \sum_i (-1)^i S_i^z, \tag{2.9}$$

where

$$J = \frac{4t_\uparrow t_\downarrow U}{(U^2 - \Delta^2)},\ \gamma = \frac{t_\uparrow^2 + t_\downarrow^2}{2t_\uparrow t_\downarrow},\ h = \frac{2(t_\uparrow - t_\downarrow)\Delta}{(U^2 - \Delta^2)}.$$

As in the Hubbard model with mass-imbalance, the γ parameter causes the spin gap of the system to be finite, in contrast to the null spin gap in the Mott-insulator for the IHM chain. Also, we must note that the last term of Hamiltonian (2.9) breaks explicitly the translational symmetry. Thus, it is expected that the ground state of the IHM with mass-imbalance in the strong coupling limit would be an antiferromagnetic insulator with a charge modulation with or without a finite spin gap.

About the existence of an intermediate phase, a previous research based on mean-field theory (MFT) [SBJJ17] of the model suggests that there is a weak first-order transition between the band insulator and the antiferromagnetic phase at one-dimension, without any intermediate phase. In this work, the two phases are characterized by charge (δ_C) and spin (δ_S) order parameters defined by:

$$\delta_C = -\frac{1}{L} \sum_{i,\sigma} (-1)^i \langle n_{i,\sigma} \rangle,$$
$$\delta_S = -\frac{1}{L} \sum_{i,\sigma} (-1)^i \sigma \langle n_{i,\sigma} \rangle.$$

The charge (resp. spin) order parameter allows to determine if there is a charge (resp. spin) order in the chain. When there is a CDW in the lattice $|\delta_C| = 1$ and $|\delta_S| = 0$, while in an antiferromagnetic phase $|\delta_C| = 0$ and $|\delta_S| = 1$. Thus, if $|\delta_C| > |\delta_S|$, a charge order leads in the system, meanwhile a spin order dominates in the lattice, if $|\delta_C| < |\delta_S|$.

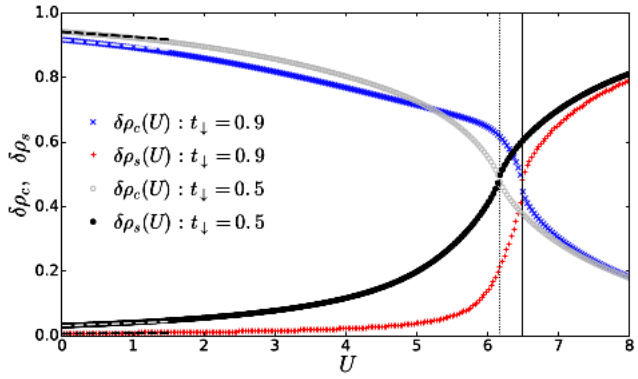

FIGURE 2.11. Mean-field density order parameters as a function of local interaction for different values of $t_\downarrow$. From [SBJJ17].

The charge and spin order parameter obtained by MFT as function of local interaction for different values of $t_\downarrow$ are shown in FIGURE 2.11. For $t_\downarrow = 0.9t_\uparrow$ as well as $t_\downarrow = 0.5t_\uparrow$, we can observe that the charge order parameter δ_C is near to one for $U = 0.0$, while $\delta_S = 0$ in this point. This fact indicates that the system is in the CDW phase in the absence of interaction. As the local interaction increases, the charge order parameter decreases and the spin order parameter increases, and $|\delta_C| > |\delta_S|$ until a threshold value U^* after which the spin order prevails in the system. According to MFT calculations, the critical point of the weak first-order transition between the charge order phase and spin order one is given by [SBJJ17]:

$$U^* = \Delta \left[1 + \left(\frac{2t_\downarrow}{\Delta} \right)^2 \right],$$

for the limit of Δ large.

2.5 A DMRG Study: IHM for Narrow Honeycomb Lattice and Mass-imbalance Chain

In order to explore the ground state properties of the IHM in a honeycomb lattice and in a mass-imbalanced chain beyond the previous DMFT and MFT approaches, we employed a DMRG algorithm with a matrix product state algorithm (MPS), based in the ITensor library [FWS20]. We use the MPS algorithm due to this technique allow us to reduce the computational complexity of our simulations, notably for the honeycomb lattice. For this kind of lattice, we simulated two narrow lattices with zigzag edge orientation using a quasi one-dimensional mapping from the original lattice to an inhomogeneous chain, as it is shown in FIGURE 2.12.

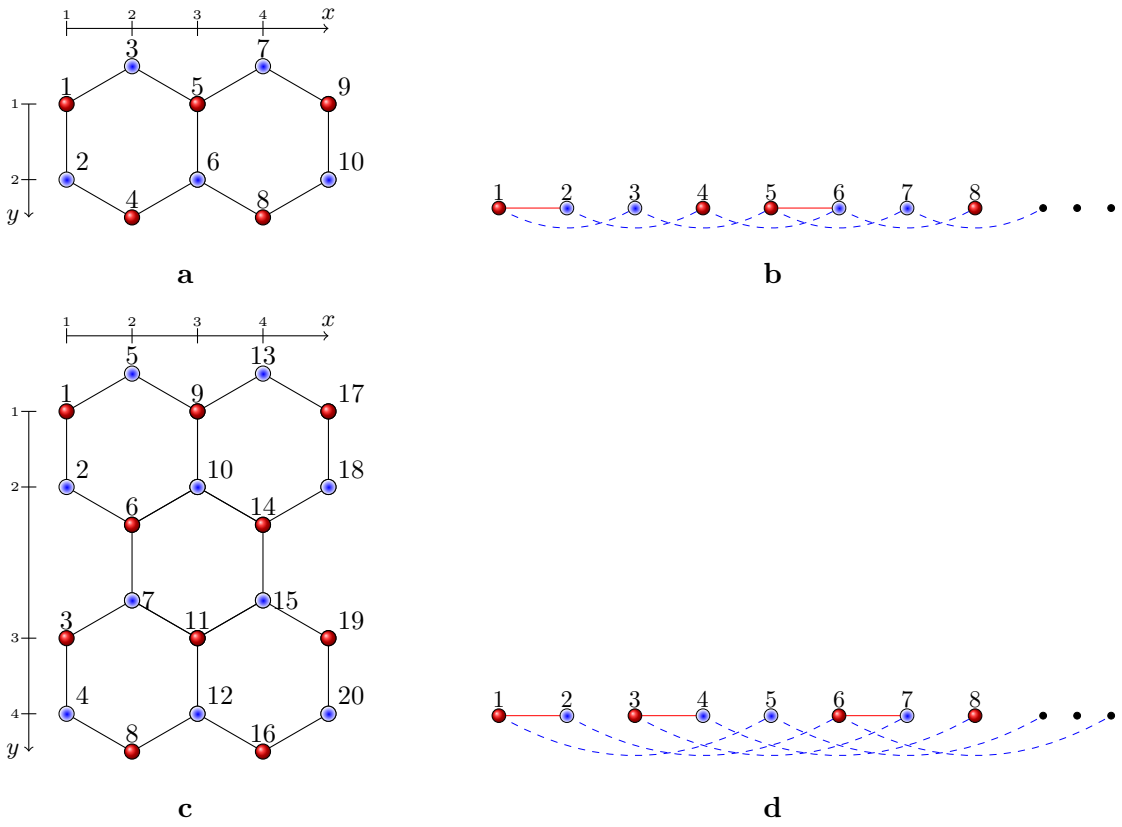

FIGURE 2.12. Map of a honeycomb bipartite lattice, with L_x sites in the zigzag edge and L_y sites in the armchair edge, into an inhomogeneous chain with long hopping. (a) Honeycomb lattice with $L_x = 2$ and $L_y = 2$, (b) image of honeycomb lattice with $L_x = 2$ and $L_y = 2$ into a chain, (c) honeycomb lattice with $L_x = 2$ and $L_y = 4$, (d) image of honeycomb lattice with $L_x = 2$ and $L_y = 4$ into a chain. The solid red spheres and fuzzy blue circles represent the two type of sites in the bipartite lattice. The x and y axis in the figure (a) and (b) represent the coordinates of each (x, y)-site in the honeycomb lattice. The solid red lines (resp. dashed blue lines) in figure (b) y (d) represent the hopping of particles to its first neighbors (resp. second or fourth neighbors).

The total number of sites of the honeycomb lattice is given by $L = 2L_xL_y + L_y$, where L_x (resp. L_y) is the total number of sites L_x in the top of zigzag edge (resp. left of armchair edge). The resulting chain from this map presents a long hopping term in its Hamiltonian and has a peculiar order of the sites of the bipartite lattice, say type A and type B sites (red solid spheres and fuzzy blue circles in FIGURE 2.12). For example, in a honeycomb lattice with $L_x = 2$ and $L_y = 2$ (FIGURE 2.12-**a**), there is a second neighbor hopping term in the Hamiltonian for all sites and an $ABBA$ ordering of sites along the lattice[5] (see FIGURE 2.12-**b**). We explore just two narrow lattices (with $L_y = 2$ and $L_y = 4$) due to simulate wider lattices involves huge tensorial products which are computational expensive (see Appendix A).

For the honeycomb lattices, in order to ensure a truncation error of around $10^{-7} \sim 10^{-6}$ of our simulations, we keep up to 900 states per block for the narrowest lattice and up to

[5]Similarly, for a honeycomb lattice with $L_y = 4$, there is a fourth neighbor hopping term in the Hamiltonian for all sites and $ABABBABA$ ordering of sites along the lattice (see FIGURE 2.12-**c,d**).

4000 for the widest lattice. The error in the ground state energy was $10^{-3} \sim 10^{-2}$ in the worst cases, but around of 10^{-5} or better in most cases. Also, we use a noise parameter $a = 10^{-12} \sim 10^{-5}$ to avoid meta-stable states. For the mass-imbalanced chain, we use the same noise parameter that for the honeycomb lattices, and keep up to 800 $\sim$ 1000 state per block in order to ensure a truncation error of around 10^{-9}. For this system, the error in the ground state energy was 10^{-6} in the worst case, but around 10^{-8} or better in the most cases.

2.5.1 Narrow honeycomb lattice $L_y = 2$

For the honeycomb lattice with $L_y = 2$, we set $t = 1$ eV as our scale energy and consider lattices with $L_x = 10, 13, 16, 19, 22$ and 25, all lattices with open boundary conditions. All quantities were calculated for an energy offset of $\Delta/t = 10$ in order to compare directly our results with the previous DMRG research of S. R. Manmana *et al.* of IHM in one-dimension.

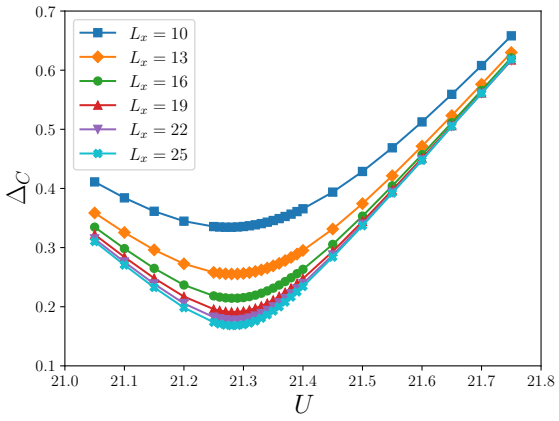

a

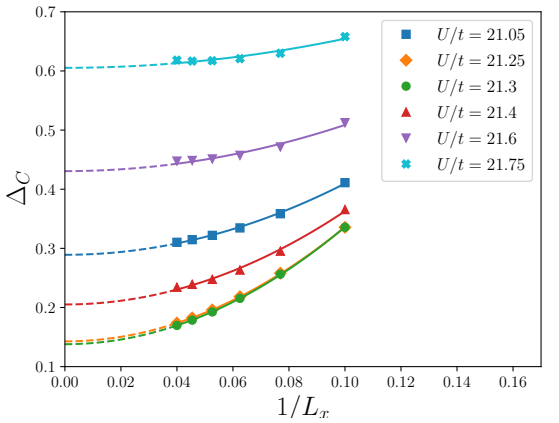

b

FIGURE 2.13. Charge gap of a narrow honeycomb lattice with $\Delta/t = 10$ and $L_y = 2$: (**a**) gap as a function of U for lattice sizes $L_x = 10, 13, 16, 19, 22$ and 25, (**b**) finite size scaling for some U values. The solid line in (**a**) is a visual guide, meanwhile the solid and dashed lines in (**b**) show a least-square fit to a second order polynomial $a + b/L^2$.

In FIGURE 2.13-a, the charge gap Δ_C as a function of the on-site interaction parameter U is shown for different lattice sizes. We observe that this gap is always finite which is characteristic of an insulator state, this suggests that any phase in the system is an insulator like in the previous studies of IHM. For all lattice sizes, we note that the charge gap present a minimum similar to the minimum reported by S. R. Manmana *et al.* [MMNS04] for the one-dimensional IHM. Also, we examine the dependence of Δ_C as a function of $1/L_x$ in the FIGURE 2.13-b for some U values in the studied region, here the gap shows a quadratic behavior in $1/L_x$ for all the explored U values.

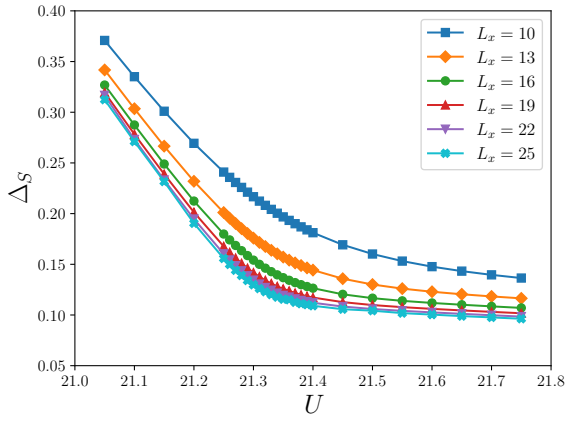

a

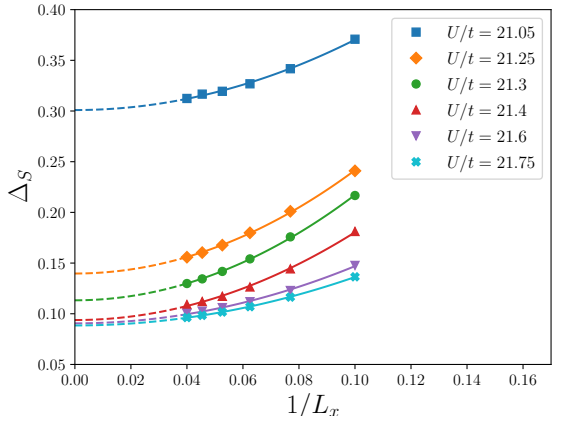

b

FIGURE 2.14. Spin gap of a narrow honeycomb lattice with $\Delta/t = 10$ and $L_y = 2$: (**a**) gap as a function of U for lattice sizes $L_x = 10, 13, 16, 19, 22$ and 25, (**b**) finite size scaling for some U values. The solid line in (**a**) is a visual guide, meanwhile the solid and dashed lines in (**b**) show a least-square fit to a second order polynomial $a + b/L^2$.

In regard with the spin gap Δ_S, the FIGURE 2.14-a shows the U dependence of this quantity for different lattice sizes. From this plot, we observe that for all lattice sizes the gap decreases linearly as a function of U for $U/t \lesssim 21.2$, then remains almost constant (in particular for large lattice size, $L_x = 19, 22, 25$) as U/t increases. This change of behavior on Δ_S with respect to U suggests a possible change in the ground state of the system (phase transition). Moreover, the region where the spin gap remains almost constant could

correspond to an antiferromagnetic phase similar to the insulator phase of the Hubbard model on narrow honeycomb lattices discussed in Section 1.4. As well as the charge gap, we explore the dependence of the spin gap as a function of $1/L_x$ and we observe again a quadratic scaling as the solid and dashed lines show in FIGURE 2.14-b. It is important to note that for all the explored values of U, the spin gap remains finite at the limit $L_x \to \infty$.

Now, about of the excitation gap Δ_E, this quantity also is finite for all explored lattice sizes as we can see from the FIGURE 2.15-a. As the charge and spin gap, the excitation gap decreases linearly for $U/t \lesssim 21.2$ and then presents a change of its behavior as a function of the local interaction parameter, which suggests a possible change in the ground state of the system depending on U. For large lattices ($L_x = 25$ for example), we note that the excitation gap presents a minimum as the charge gap for later increases up to a local maximum and finally decreases slowly to remain almost constant for $U/t \gtrsim 21.4$, similar to the spin gap. Again, the finite size scaling, shown in the FIGURE 2.15-b, indicates a quadratic dependence of Δ_E with respect to $1/L_x$.

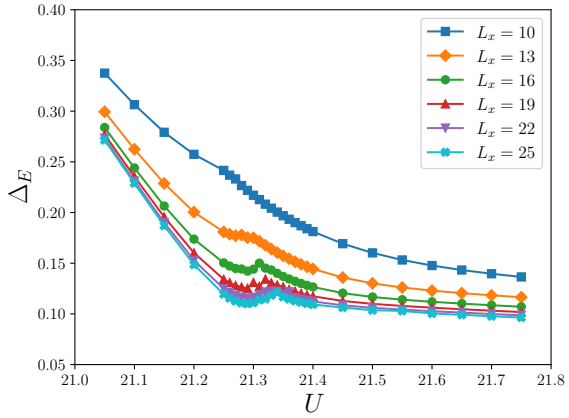

a

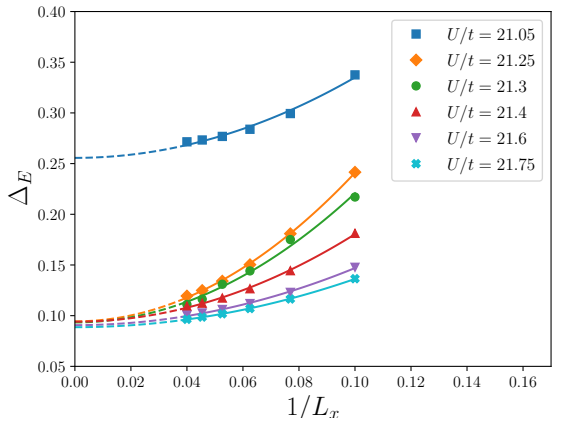

b

FIGURE 2.15. Excitation gap of a narrow honeycomb lattice with $\Delta/t = 10$ and $L_y = 2$: (**a**) gap as a function of U for lattice sizes $L_x = 10, 13, 16, 19, 22$ and 25, (**b**) finite size scaling for some U values. The solid line in (**a**) is a visual guide, meanwhile the solid and dashed lines in (**b**) show a least-square fit to a second order polynomial $a + b/L^2$.

At the limit $L_x \to \infty$, we found that all explored gaps are finite, but there is a clear change in the behavior of the gaps as a function of U, as we can see in FIGURE 2.16. For $U/t \lesssim 21.2$, the charge and spin gaps are equal and decrease linearly as U/t increases. For these values of U/t, the excitation gap also decreases linearly as a function of U/t, but its value is slightly smaller than the others gap energies. Then, for $21.2 \lesssim U/t \lesssim 21.4$, the charge and excitation gap present a minimum value for later increase. In this region, the excitation gap reaches a maximum matching with the spin gap energy. Finally, for $U/t \gtrsim 21.4$, the spin and excitation gap decreases slowly remaining equal and almost constant, while the charge gap increases linearly. In this last range, the fact that the first excited state corresponds to a spin excitation suggests a fundamental change in the ground state of the system such that a quantum phase transition could occur for $21.2 \lesssim U/t \lesssim 21.4$

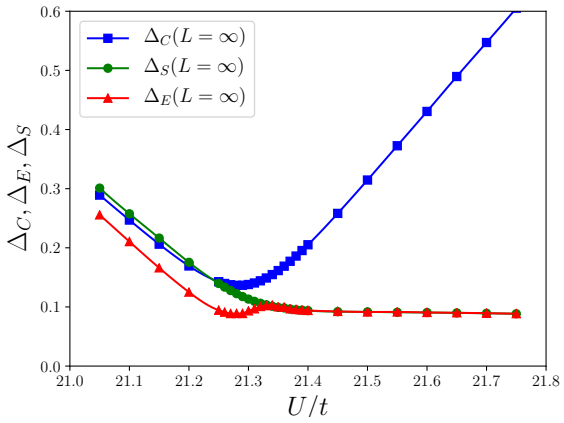

FIGURE 2.16. Charge, spin, and excitation gap at thermodynamic limit for a narrow honeycomb lattice with $\Delta/t = 10$ and $L_y = 2$. Solid lines are a visual guide.

In order to determine if there is a quantum phase transition in the system, we calculated the fidelity susceptibility of the state as a function of the local interaction parameter. This quantity measures the change in the overlapping of the ground state wave functions as a function of a given parameter and has been used to study quantum phase transitions [ZPac06, GU10, CWHW08]. For a lattice with L sites, the susceptibility as a function of U is given by:

$$\chi(U) = -\frac{2}{L} \lim_{dU \to 0} \frac{\log F(U, U+dU)}{dU^2},$$

where $F(U, U+dU) = \langle \Psi(U) | \Psi(U+dU) \rangle$ is the fidelity, the ground state wave function Ψ overlapping. Note that those quantities are useful to identify a critical point where there is a fundamental change of the ground state of the system. In fact, if there is no dependence of the ground state with respect to the parameter U, the inner product $\langle \Psi(U_1) | \Psi(U_2) \rangle = 1$ for any U_1, U_2, then $\chi(U) = 0$ for all U. However, if $\chi(U) \neq 0$ for some $U = U_c$, we can conclude that the state $\Psi(U_c)$ is different to the state $\Psi(U_c + dU)$ for any small dU $(F(U_c, U_c + dU) \neq 1)$, i.e. there is a change in the ground state near to U_c.

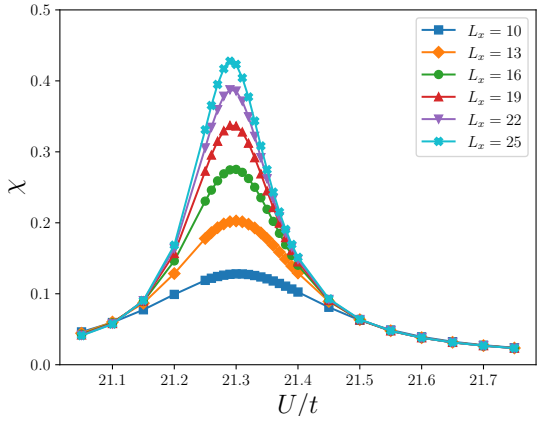

FIGURE 2.17. Susceptibility of fidelity for narrow honeycomb lattices with $\Delta/t = 10$, $L_y = 2$ and $dU = 0.01$. Solid lines are a visual guide.

In FIGURE 2.17, the fidelity susceptibility for different lattice size as a function of U/t is shown. From this plot, we confirm a quantum phase transition in the system, since the susceptibility is not null for some values of U. In particular, for $U_c = 21.3t$, the susceptibility presents a peak indicating the critical point of transition. Although, the maximum value of susceptibility increases with the lattice size, we do not observe an appreciable dependence of the critical point with respect to $1/L_x$. Unlike the IHM in a one-dimensional lattice, we do not observe an intermediate phase, a result that is consistent with the previous DMFT study of IHM on a honeycomb lattice.

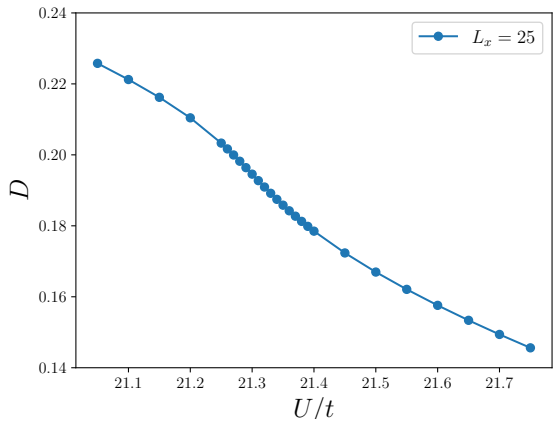

FIGURE 2.18. Double occupancy as a function of U/t for a lattice with $L_x = 25$, $L_y = 2$ and $\Delta/t = 10$

As we mentioned above, the fact that the spin gap remains finite in the system suggests the insulator phase for $U > 21.3$ is antiferromagnetic, according to the effective Heisenberg model for strong coupling limit. Indeed, we can observe this from the double occupancy and density plots of the lattice. In FIGURE 2.18, the double occupancy as a function of U/t is shown. Here, we can see that this quantity is a decreasing function of U/t which is characteristic in the transition from a band insulator with a CDW to an antiferromagnetic insulator in the IHM. When $U \ll \Delta$, the particles with different spin tends to occupy a

same site, due to its repulsion interaction is not so strong and the probability of tunneling is low, cause the high energy offset. For $U \gg \Delta$, the strong repulsion interaction between particles with different spin cause that two particles can not be in the same site, so that must be one particle per site in the lattice.

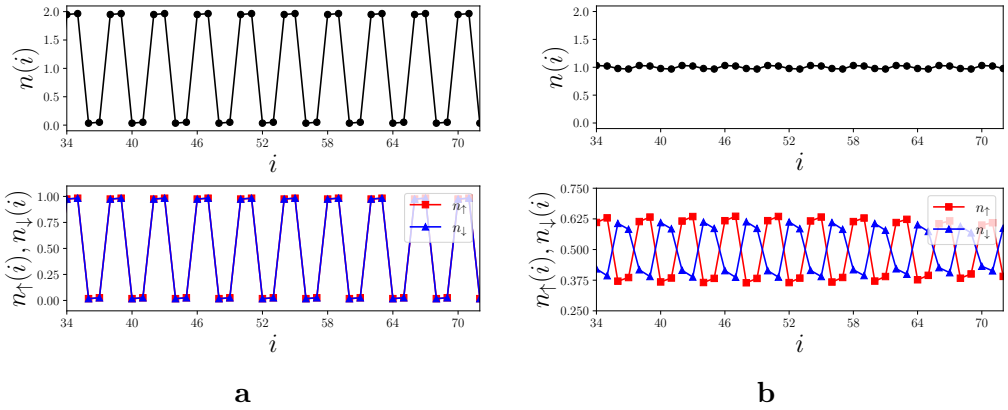

FIGURE 2.19. Density per site in a honeycomb lattice with $L_x = 25$, $L_y = 2$ and $\Delta/t = 10$. (**a**) Density profiles for $U/t = 10$, (**b**) Density profiles for $u/t = 30$. In the top of each figure is shown the profile of total density $n(i) = \langle n_i \rangle$ of the lattice, while in the bottom of each figure is shown the spin density profiles $n_\uparrow(i) = \langle n_{i,\uparrow} \rangle$ and $n_\downarrow(i) = \langle n_{i,\downarrow} \rangle$. Solid lines are a visual guide.

In the FIGURE 2.19, the density profile of the system is shown for two values of U/t, one for each phase in the system. For $U \ll U_c$ ($U/t = 10$), we find that $D = 0.48$ and observe that there is a CDW in the system with a periodicity of two sites, i.e. two sites with two particles and then two sites without particles (top of FIGURE 2.19-**a**). This peculiar charge modulation is due to the quasi-one dimensional map used in this investigation (see FIGURE 2.12). For $U \gg U_c$ ($U/t = 30$), we find that $D = 0.01$ and observe that there is one particle per site (top of FIGURE 2.19-**b**). In this phase, we also observe that there is a braid in the spin density profile of the lattice (see bottom of FIGURE 2.19-**b**), where it is more probable to found a particle with spin up (resp. spin down) on an odd site (resp. even site).

This density profile in the lattice suggests an antiferromagnetic ordering in the phase for $U > U_c$. In fact, we observe an antiferromagnetic order in this phase by analyzing the spin correlation function $S(x, y; x', y') = \langle S^z(x, y) S^z(x', y') \rangle - \langle S^z(x, y) \rangle \langle S^z(x', y') \rangle$. In FIGURE 2.20-**a** is shown the spin correlation along the top zigzag edge[6] for two different U values. For $U/t = 10$ (CDW phase), the correlation is always zero, hence there is no magnetic order in the top edge as well as in the bottom edge[7]. However, for $U/t = 30$, the correlation alternates between positive and negative for neighbor sites, indicating an antiferromagnetic order in the edges. Moreover, as we can see in the inset of the FIGURE 2.20-**a**, the spin correlation between sites of different edges is always negative for $U/t = 30$, a feature consistent with an antiferromagnetic order in the whole lattice for $U > U_c$.

[6]Here, we refer to the correlation function between the site $(1, 1)$ and sites $(x, 1)$ of the original honeycomb lattice.

[7]Since the honeycomb lattice has reflection symmetry, we obtain the same results for the bottom zigzag edge.

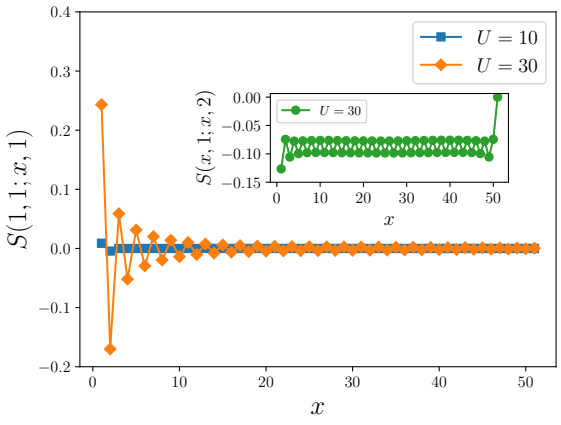

a

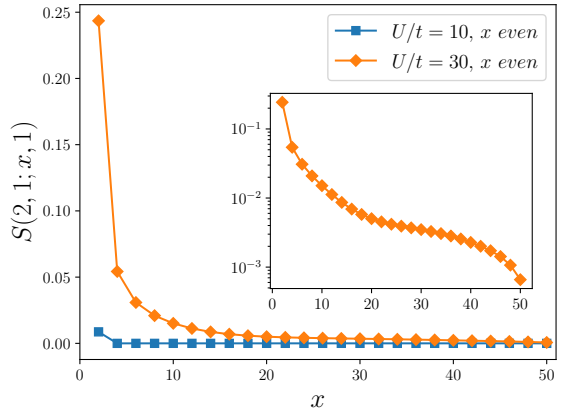

b

FIGURE 2.20. Spin correlation for a lattice with $L_y = 2$, $L_x = 25$ and $\Delta = 10$ for two values of local interaction parameter. (**a**) Correlation function along the top zigzag edge, (**b**) Correlation function along the sites in the top of edge (sites with x coordinate even). The inset of figure (**a**) shows the spin correlation between sites of different edge for $U/t = 30$, meanwhile the inset of figure (**b**) shows a semi-log plot of the correlation function for $U/t = 30$. Solid lines are a visual guide.

Finally, we also find an interesting phenomenon in the top of the zigzag edge of the lattice. For the sites in this part of the lattice, we observe a ferromagnetic order in the antiferromagnetic insulator phase. For $U/t = 30$, we note that the spin correlation function along the top of the edge is always positive, as we can see in the FIGURE 2.20-**b** and in its inset. This feature of the ground state is similar to the previous researches about the Hubbard model in zigzag graphene nanoribbons discussed in the Section 1.4. In regard with the CDW phase, we again observe that there is no magnetic order in the lattice (see square blue points in FIGURE 2.20-**b**).

To conclude, according to our DMRG study of the IHM on a zigzag narrow honeycomb lattice with $L_y = 2$, there is a quantum phase transition between a CDW phase and an antiferromagnetic insulator phase with a finite spin gap. We find that the transition occurs at $U_c = 21.3t$ for a energy offset of $\Delta = 10t$. This point is identical to the critical point of the transition from the bond-order insulator to the Mott-insulator in the IHM in one-

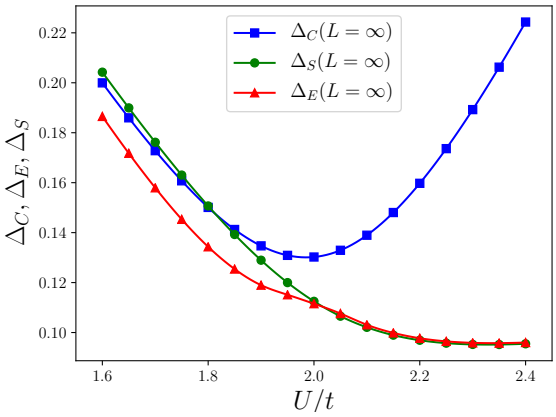

a

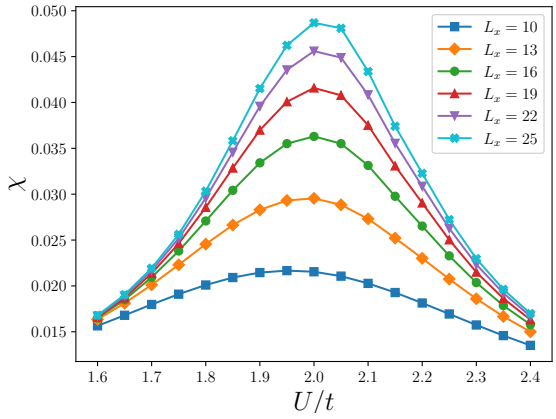

b

FIGURE 2.21. Gap energies and fidelity susceptibility as a function of U for a narrow honeycomb lattices with $L_y = 2$ and $\Delta/t = 0.4$: (**a**) charge, spin, and excitation gap energy at the limit $L_x \to \infty$, (**b**)Susceptibility for different lattice sizes.

dimension for the same energy offset. Then, in the honeycomb with $L_y = 2$, the band insulator region is larger than the band insulator region in the one-dimensional lattice such that the intermediate region disappears.

Comparing our results with the previous DMFT calculations, we noticed that there is a difference for the honeycomb lattice with $L_y = 2$, since our DMRG calculation predicts $U_c = 2t$ for $\Delta = 0.4t$, while $U_c = 4t$ according to the DMFT results for that value of energy offset. Indeed, in FIGURE 2.21, we show our results about the dependence of the gap energies and fidelity susceptibility with respect to the local interaction for a lattice with an energy offset of $\Delta/t = 0.4$. The behavior of the gap energies is the same that we described before, where the gap energies decrease as a function of U/t until the charge gap reaches a minimum value and the spin and excitation gap take the same value at $U_c/t = 2.0$ (see FIGURE 2.21-**a**). As we show in the FIGURE 2.21-**b**, at this point the susceptibility of fidelity reaches a maximum in all explored lattices [8], indicating that the phase transition occurs there.

[8] As before, we do not observe any finite size effect in the maximum of the susceptibility.

2.5.2 Narrow honeycomb lattice $L_y = 4$

Now, in regard with the lattice with $L_y = 4$, we set also our scale energy as $t = 1$ and explore the largest lattice ($L_x = 6$) that we could simulate with open boundary conditions. According to the previous DMRG study about narrow zigzag nanoribbons [HL16], lattices with $L_x = 10$ and $L_y = 4$ require keeping around of $15000 \sim 20000$ states per block in the DMRG algorithm, a number of states per block larger than the one we achieve with our code and resources.

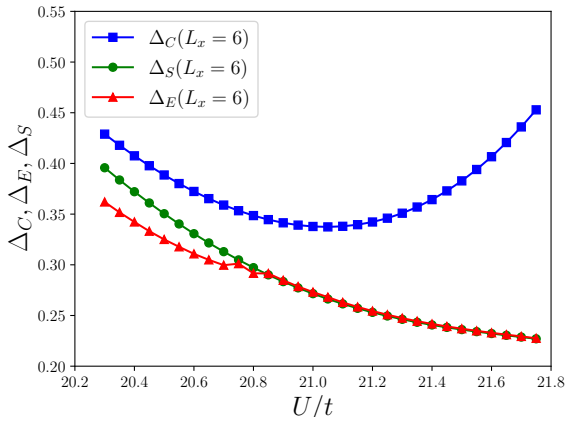

FIGURE 2.22. Charge, spin, and excitation gap for a narrow honeycomb lattice with $\Delta/t = 10$, $L_x = 6$, $L_y = 4$. Solid lines are a visual guide.

In FIGURE 2.22 is shown the charge, spin and excitation gap as a function of U/t. As before, we observe two regions in the system. On the one hand, a region where all gaps are different and decrease linearly as U/t increases. On the other hand, a region where the spin and excitation gap are equal, and the charge gap reaches a minimum value for then increases. For this lattice, we do not observe that the spin and excitation gap remains almost constant for large value of U/t. However, the fact that the first excitation state of the system changes with the parameter U/t suggest a possible phase transition in the lattice. This transition is confirmed by analyzing the fidelity susceptibility for this lattice. In FIGURE 2.23, we observe that this quantity is not zero, reaching a maximum value. Nevertheless, this value is very small and can not be used to determine a critical phase transition point.

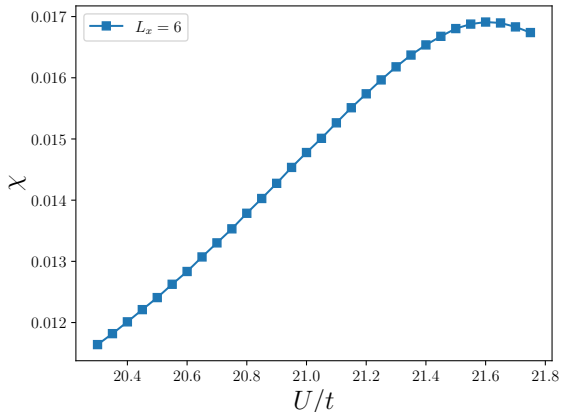

FIGURE 2.23. Fidelity susceptibility for narrow honeycomb lattices with $\Delta/t = 10$, $L_x = 6$, $L_y = 4$ and $dU = 0.01$. Solid lines are a visual guide.

About the double occupancy in the lattice, in the FIGURE 2.24, we observe that this quantity is decreasing as a function of U/t indicating a transition from a phase with double occupancy (CDW phase) and a phase without charge modulation. In fact, from the density plots of FIGURE 2.25, we can note that for the weak coupling phase ($U/t = 10$, see FIGURE 2.25-**a**), there is a charge modulation in the lattice which has a peculiar periodicity due to the quasi-one dimensional map (FIGURE 2.12). For the strong coupling phase ($U/t = 30$, see FIGURE 2.25-**b**), there is no charge modulation, and we again observe a braid in the spin density (bottom of FIGURE 2.25-**b**). As before, this braid suggests an antiferromagnetic order in the lattice.

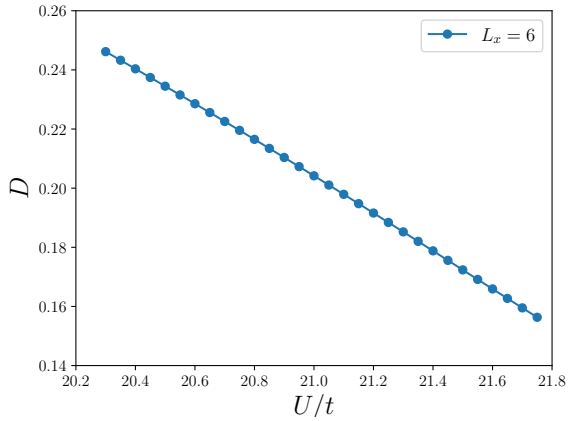

FIGURE 2.24. Double occupancy as a function of U/t for a lattice with $L_x = 6$, $L_y = 4$ and $\Delta/t = 10$

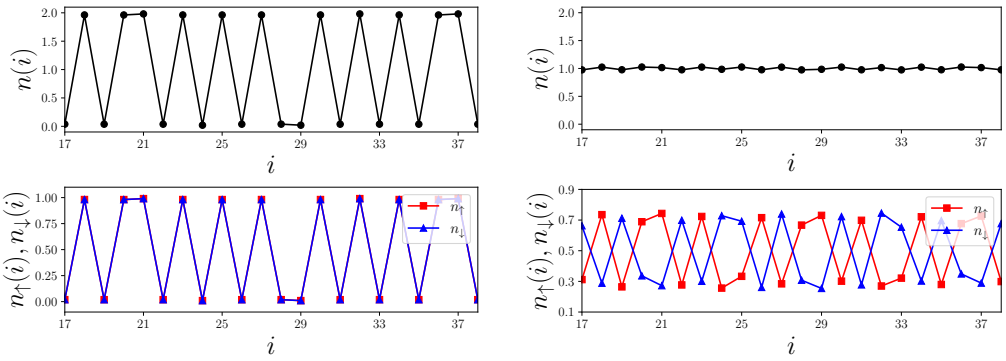

FIGURE 2.25. Density per site in a honeycomb lattice with $L_x = 6$, $L_y = 2$ and $\Delta/t = 10$. (**a**) Density profiles for $U/t = 10$, (**b**) Density profiles for $u/t = 30$. In the top of each figure is shown the profile of total density $n(i) = \langle n_i \rangle$ of the lattice, while in the bottom of each figure is shown the spin density profiles $n_\uparrow(i) = \langle n_{i,\uparrow} \rangle$ and $n_\downarrow(i) = \langle n_{i,\downarrow} \rangle$. Solid lines are a visual guide.

The antiferromagnetic order in the system is confirmed by analyzing the spin correlation $S(x, y; x', y')$ along the lattice. The spin correlation along the two first rows of the honeycomb lattice for the two phases is shown in FIGURE 2.26-**a**,**b**. For $U/t = 30$, we observe an alternating spin correlation along the x axis in both rows, which is expected in an antiferromagnetic ground state. Also, in the inset of FIGURE 2.26-**a**, **b**, we see that the spin correlation between sites of different rows is always negative for $U/t = 30$, a result consistent with an antiferromagnetic order in whole lattice. As in the previous subsection, we just analyze the first two rows of the lattice due to the reflection symmetry of the honeycomb lattice. Besides, as before, we observe an interesting magnetic order in the zigzag edge of lattice where the sites in the top of the edge has a ferromagnetic order, since its spin correlation is always positive (see FIGURE 2.26-**c** and its inset). In regard to the CDW phase ($U/t = 10$), we do not observe any correlation in the system.

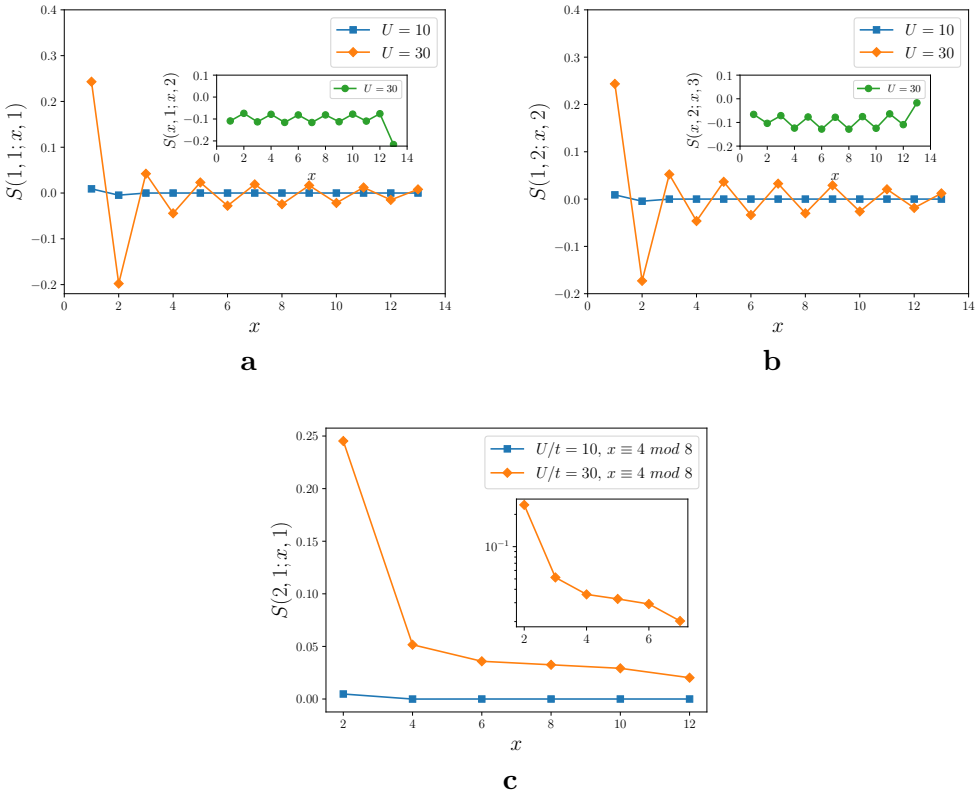

FIGURE 2.26. Spin correlation for a lattice with $L_y = 4$, $L_x = 6$ and $\Delta = 10$ for two values of local interaction parameter. (**a**) Correlation function along first row of lattice (top zigzag edge), (**b**) Correlation function along second row of lattice, (**c**) Correlation function along the sites in the top of edge (sites with x coordinate such that $x \equiv 4\ mod\ 8$). The inset of figure (**a**)-(**b**) shows the spin correlation between sites of different rows for $U/t = 30$, meanwhile the inset of figure (**c**) shows a semi-log plot of the correlation function for $U/t = 30$. Solid lines are a visual guide.

As the conclusion of this subsection, we identify the same insulator phases that in the lattice with L_y, but we can not determine the critical point of transition between them, due to the computational effort required to explore the lattices with $L_y = 4$ at the limit of $L_x \to \infty$.

2.5.3 Mass-imbalanced chain

For the mass-imbalanced chain, we set $t_\uparrow = 1$ as our scale energy and consider lattices with size from $L = 64$ to $L = 512$ with open boundary conditions. In order to compare our results with the results of the previous research of Sekenia *et al.* about the mass-imbalanced IHM, we explore the ground state properties of the system for an energy offset of $\Delta/t_\uparrow = 0.0 \sim 3.0$ and an imbalance parameter $t_\downarrow/t_\uparrow = 0.1 \sim 0.9$.

The dependence of the charge and excitation gap as a function of the local interaction is shown in FIGURE 2.27 for an infinite chain with $\Delta/t_\uparrow = 2.0$ and two values of imbalance parameter. For the weak coupling limit, we expect that the charge and excitation gaps be finite in the thermodynamic limit, since the ground state of IHM in this limit must be correspond to a CDW. In fact, for this limit, we observe that both gaps are finite and

equal, but decrease as a function of $U/t_\uparrow$ until a gap closing occurs. In the inset of FIGURE 2.27-(a), it is shown the gaps as a function of $1/L$ for $U/t = 4.55$. From this plot, we note that both gaps decrease linearly with the lattice size, reaching a small value that goes to zero as $L \to \infty$.

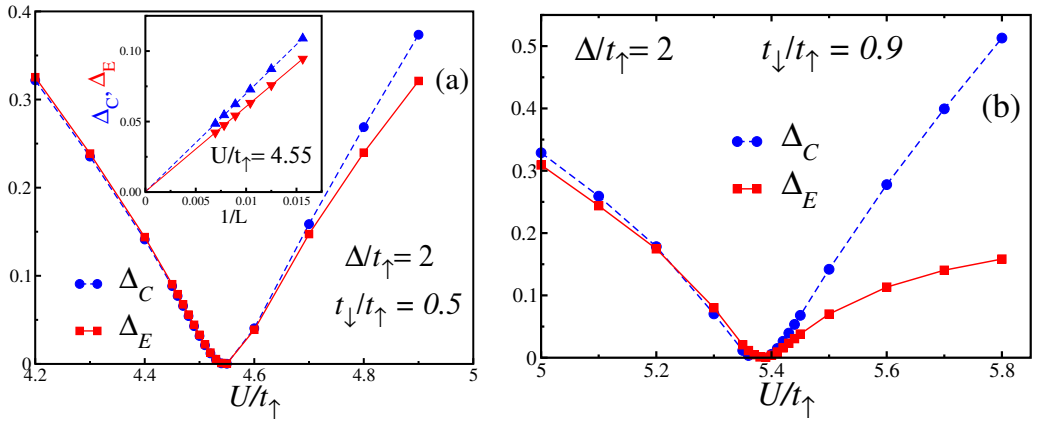

FIGURE 2.27. Charge and excitation gap in the thermodynamic limit as a function of local parameter for a lattice with $\Delta/t_\uparrow = 2.0$ and two values of imbalance parameter: (a) $t_\downarrow/t_\uparrow = 0.5$, (b) $t_\downarrow/t_\uparrow = 0.9$. The Extrapolated values of the gaps were obtained by a linear fit as a function of $1/L$, as the finite size scaling that it is shown in the inset of figure (a) for $U/t = 4.55$. The lines are visual guides. From [PGFSV21].

We observe that the gap closing takes place at $U^*/t = 4.55$ for $t_\downarrow/t_\uparrow = 0.5$ and $U^*/t = 5.38$ for $t_\downarrow/t_\uparrow = 0.9$ (see FIGURE 2.27-(b)). After the gap closing, we observe tha both gaps increase with the local interaction, but in a different rate, indicating a change in the ground state of the system with a possible quantum phase transition at $U = U^*$. This result is similar to the previous MFT calculations. But comparing the critical points reported in that research ($U^*_{MF} = 4.25$ for $t_\downarrow/t_\uparrow = 0.5$ and $U^*_{MF} = 4.81$ for $t_\downarrow/t_\uparrow = 0.9$), we note a clear difference due to the correlation considered in our approach.

In order to describe the two phases in the system, we calculate some physical quantities for $\Delta/t_\uparrow = 2.0$ and $t_\downarrow/t_\uparrow = 0.9$. On the one hand, the spin gap in the thermodynamic limit[9] as a function of local interaction is shown in FIGURE 2.28-(a). We observe that this gap decreases linearly as $U/t_\uparrow$ increase until $U = U* = 5.38t_\uparrow$, for then changes its behavior keeping almost constant for larges values of local interaction. We see this in the inset of FIGURE 2.28-(a), where the dependence of the spin gap with respect to the inverse of the lattice size is shown for $U/t_\uparrow = 5.8$. In this inset, we note that the spin gap tends to a finite value $\Delta_S/t_\uparrow = 0.153$ (dark green diamond point). As before, this feature of the phase for large values of local interaction indicates that this phase could be an antiferromagnetic insulator, according to the effective Heisenberg model for strong coupling limit of IHM.

[9]The extrapolated values was obtained by a quadratic fit of the spin gap with respect to the inverse of the lattice, a similar process to the displayed in the inset of FIGURE 2.28-(a).

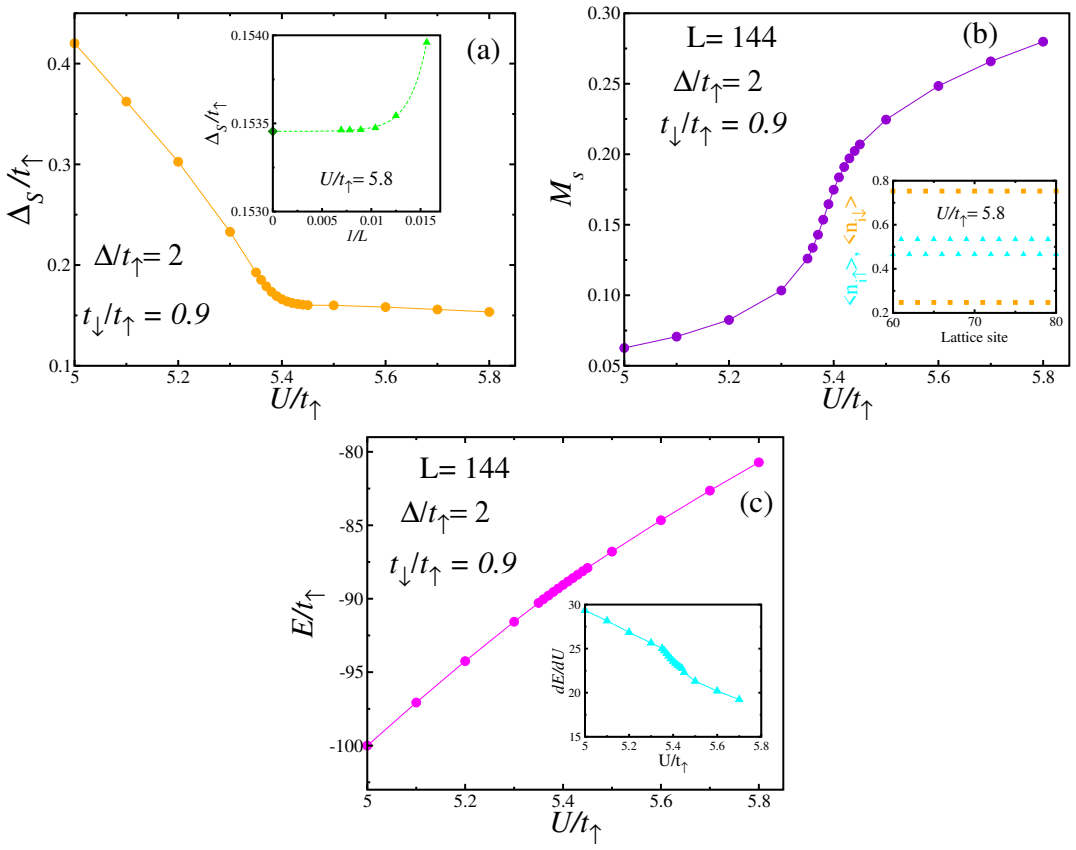

FIGURE 2.28. Physical quantities of an ionic Hubbard chain as a function of local interaction for lattices with $\Delta/t_\uparrow = 2.0$ and $t_\downarrow/t_\uparrow = 0.9$: (a) Spin gap in the thermodynamic limit, (b) staggered magnetization for a lattice with $L = 144$ sites, (c) ground state energy for a lattice with $L = 144$ sites. The inset of figure (a) shows a finite-size scaling to a quadratic polynomial of $1/L$ (dashed lines) used to obtain the extrapolated spin gap value for $U/t_\uparrow = 5.8$. The inset of figure (b) shows the spin density profile for $U/t_\uparrow = 5.8$. The inset of figure (c) shows the first derivative of the ground state energy. The solid lines are visual guides. From [PGFSV21].

We confirm the antiferromagnetic order in the system for larges values of $U/t_\uparrow$ by analyzing the staggered magnetization. This quantity as a function of local interaction is shown in the FIGURE 2.28-(b) for a lattice with $L = 144$ sites. In this plot, we observe that for small values of $U/t_\uparrow$ ($U < 5.38t_\uparrow$) the staggered magnetization is small, since the ground state is a CDW with a double occupied site in the two site unit cell. For large local interaction ($U > 5.38t_\uparrow$), the staggered magnetization increases quickly, indicating an antiferromagnetic order in the system in this region. The antiferromagnetic order for the phase with strong local interaction is shown in the inset of FIGURE 2.28-(b). Here, we observe that the spin densities $\langle n_{i,\uparrow}\rangle$, $\langle n_{i,\downarrow}\rangle$ oscillate in phase indicating a charge modulation in the lattice, but with a preference of spin up particles for even sites and spin down particles for odd sites (see orange square for site 70 in the inset, for example).

Thus, as well as the previous MFT study of the IHM with mass-imbalance, we predict that in one-dimension there are only two phases: a CDW insulator for weak interaction and an antiferromagnetic insulator with finite spin gap for strong interaction, i.e., again we do not observe the intermediate phase presented in the balanced ionic Hubbard chain. In regard with the order of the transition, we find that this transition is a continuous one, in

contrast with the weak first order transition predicted in the previous MFT calculations. We can see this from the dependence of ground state energy with respect to the local interaction that it is shown in FIGURE 2.28-(c) for a lattice with $L = 144$ sites. From this plot, we observe that the ground state energy is continuous as a function of $U/t_\uparrow$ with continuous derivative (see inset of FIGURE 2.28-(c)).

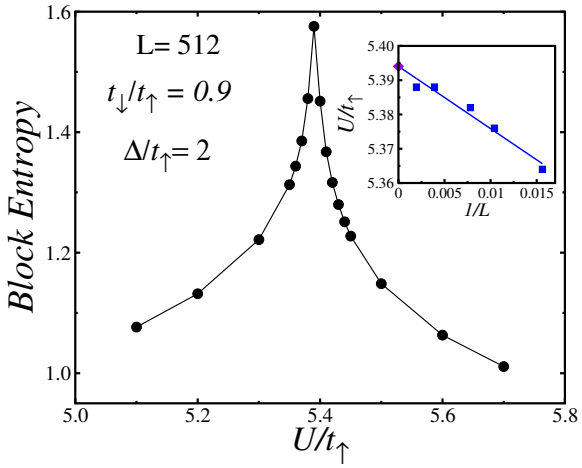

FIGURE 2.29. von Neumann block entropy as a function of local interaction for a lattice with $L = 512$ sites, $\Delta/t_\uparrow = 2.0$ and $t_\downarrow/t_\uparrow = 0.9$. The inset shows the dependence of block entropy with respect to the inverse of the lattice size. From [PGFSV21].

In order to obtain a phase diagram of the system, we calculate the von Neumann block entropy of the chain given by

$$S_A = -tr(\rho_A \log \rho_A), \tag{2.10}$$

where $\rho_A = tr_B(\rho)$, with $\rho = |\Psi\rangle \langle\Psi|$, is the reduced density matrix of the subspace A of an $A - B$ bipartite partition of the lattice[10]. This quantity is useful to determine critical points of phase transitions, even more for anisotropic systems like the IHM with mass-imbalance, where the block entropy presents a maximum related with the phase transition point [VLRK03, ON02, MAFSV10]. Indeed, as we can see in the FIGURE 2.29 for a lattice with $L = 512$ sites, $\Delta/t_\uparrow = 2.0$ and $t_\downarrow/t_\uparrow = 0.9$, the bock entropy reaches a maximum value near to the gap closing point ($U^*/t_\uparrow = 5.38$), confirming that near this point a quantum phase transition occurs. However, as we can observe in the behavior of the maximum position of block entropy with respect to the lattice size (see in the inset of the FIGURE 2.29), there is a small finite size effect which give us a correction from $U^*/t_\uparrow = 5.38$ to $U^*/t_\uparrow = 5.39$ in the critical point at thermodynamic limit (purple diamond point in the inset).

[10]In our calculation, we divided the chain by the middle.

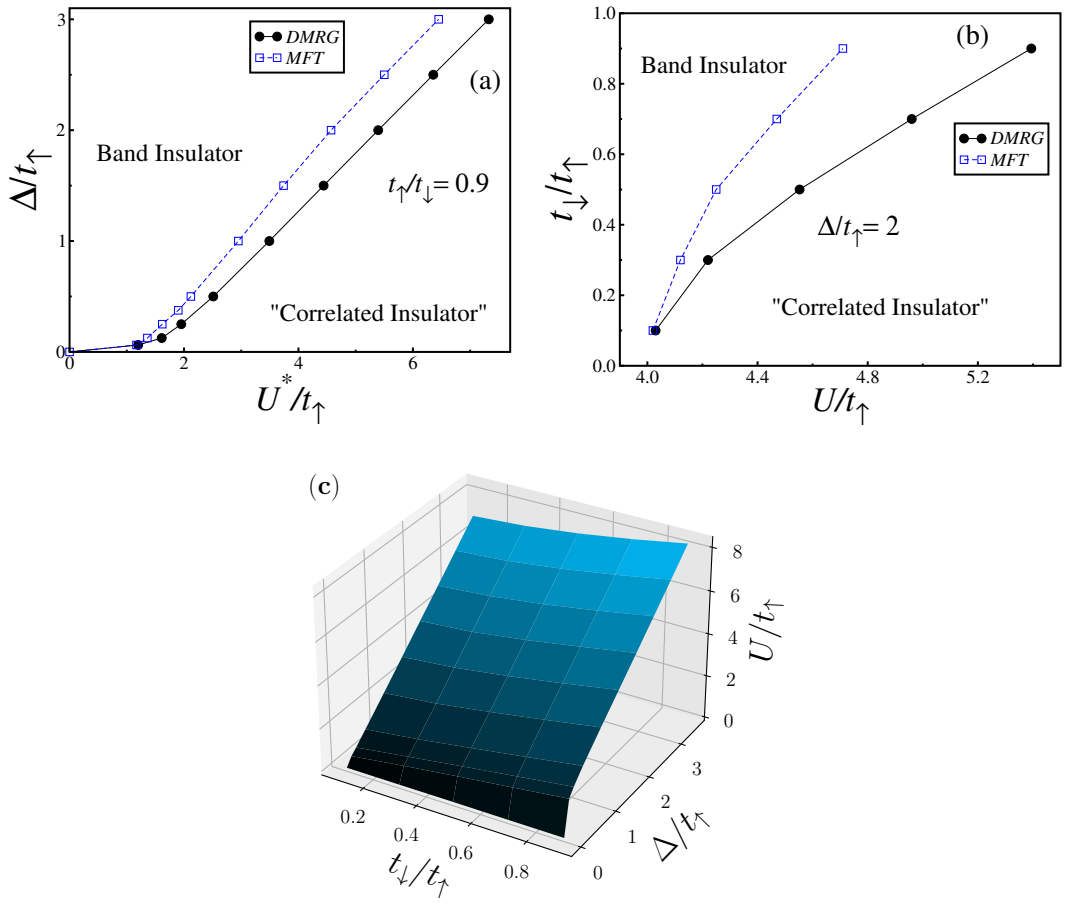

FIGURE 2.30. Phase diagram of the IHM with mass-imbalance. In figure (a) (resp. figure (b)), critical points obtained with MFT (blue empty squares, from [SBJJ17]) and DMRG (black circles corresponding to extrapoled values from maximum of entropy) are shown in the $\Delta - U^*$ plane (resp. $t_\downarrow - U^*$ plane). In figure (c), the critical point surface as a function of energy offset and imbalance parameter is shown. This surface divides the space into the CDW insulator phase (above the surface) and antiferromagnetic insulator phase (beneath the surface). From [PGFSV21].

Taking account this correction in the critical points, we obtain the phase diagram of the system for different values of energy offset and imbalance parameter. In FIGURE 2.30-(a), we show the phase diagram in the plane $\Delta - U^*$ for an imbalance parameter $t_\downarrow/t_\uparrow = 0.9$, where the critical points found by MFT and by DMRG are compared. We observe that for $\Delta/t_\uparrow$ near to zero the critical points are every tiny, for then increase quickly and follow increasing almost linearly for both methods. Although for small energy offset, the critical points of MFT are similar to the obtained with DMRG, we observe a clear difference in the critical points, where U^* is higher for the DMRG as Δ increases. This difference is due to in our DMRG calculation it is taking into account the correlation between the particles, meanwhile the mean-field theory (MFT) fundamentally neglects this correlation. Now, fixing the energy offset to $\Delta/t_\uparrow = 2.0$, we again observe a difference between the two methods. In FIGURE 2.30-(b), we see that the critical points for both methods increase as the imbalance parameter increases and just coincide at $t_\downarrow/t_\uparrow = 0.1$. Finally, we display the phase diagram space of the system in FIGURE 2.30-(c), where the surface corresponds to the critical points of the transition between the CDW phase (above the surface) and the antiferromagnetic insulator phase (beneath the surface).

In conclusion, our DMRG study of the IHM with mass-imbalance predicts a phase transition between two types of insulators without any intermediate phase like in the balanced IHM on one-dimension. Additionally, using the von Neumann in the middle of the chain, we find a difference with respect to the critical points calculated using MF. Also, we predict that the transition is a continuous one, unlike the weak first order transition reported in the previous MFT study.

Conclusions

Motivated by the controversial discussion about the physics in the intermediate region of the insulator-insulator transition of the IHM, we studied the transition in two scenarios: the IHM on narrow honeycomb lattices and the IHM with mass-imbalance in one-dimension. In order to explore those systems beyond the previous MFT and DMFT studies, we used a DMRG algorithm together with an MPS method, considering the correlation between the particles of the system in a more precise way. For the two systems of interest, we calculated several quantities related to the ground state like the spin, charge and excitation energy gaps, double occupancy, density profiles, spin-spin correlation function, staggered magnetization and von Neumann block entropy.

For the IHM model on narrow honeycomb lattices, we found that there are just two insulator phases in the system: a band insulator with CDW and an antiferromagnetic insulator, a result that is consistent with the previous DMFT study of the system [LLTL15]. Besides, we noticed that the antiferromagnetic insulator is not a Mott-insulator for the two explored lattices, unlike to the results of DMFT calculations. On the one hand, for the lattice with $L_y = 2$, we found that the spin gap is finite and almost constant as a function of local interaction for the antiferromagnetic phase, similar to the behavior predicted previously in the insulator phase of the Hubbard model on honeycomb lattice [HHLM03]. Also for this phase, we found that there is a ferromagnetic order along the top sites of the zigzag edge and antiferromagnetic order between edges, a feature similar to the one predicted in the insulator phase of the Hubbard model on honeycomb lattice [HL16]. On the other hand, for the lattice with $L_y = 4$ in the insulator phase with strong local interaction, we found that the spin gap is also finite and there is the same magnetic order in the edges of the lattice, but we were not able to explore the system in the thermodynamic limit ($L_x \to 0$), because it requires more computational power than we have. Due to this, we were capable to identify the two insulator phases of the system, but not the critical point of transition between them.

About the position of the critical points in the IHM on a narrow honeycomb lattice, those were determined by the fidelity susceptibility, a quantity that presents a maximum value around the phase transition. We found that the transition from band insulator to antiferromagnetic insulator phase occurs at $U_c = 21.3t$ for the narrowest lattice with an energy offset of $\Delta = 10t$. This point is identical to the critical point of the transition from the bond-order insulator to the Mott-insulator in the IHM in one-dimension for the same energy offset. Then, in the honeycomb with $L_y = 2$, the band insulator region is larger than the band insulator region in the one-dimensional lattice such that the intermediate region disappears. Comparing our results with the previous DMFT calculations, we noticed that there is a difference for the honeycomb lattice with $L_y = 2$, since our DMRG calculation

give $U_c = 2t$ for $\Delta = 0.4t$, while $U_c = 4t$ according to the DMFT results for that value of energy offset.

In regard to the IHM with mass-imbalance in a one-dimensional lattice, we also were able to identify a quantum phase transition from a band insulator with CDW and an antiferromagnetic insulator, without an intermediate phase. Although this results is consistent with the previous MFT study of the system, we found, by analyzing the behavior of the ground state energy as function of local interaction, that this phase transition is continuous contradicting the MFT result. Also, according to our DMRG study, the critical points determined by the maximum value of von Neumann entropy at thermodynamic limit are larger than the MFT ones, except for small values of energy offset and high values of the imbalance parameter.

As outlook of this work, we recommend implementing other numerical methods to explore the two-dimensional physics of the IHM. Numerical approaches like *Projected Entangled Pair States* (PEPS) [CPGSV21] can be suitable to simulate wide honeycomb lattices. Also, study the mass-imbalance model in narrow honeycomb lattice or in a lattice with other geometry is a possible research to the future, as well as explore the model out of the half-filling with different lattice geometries.

APPENDIX

Some Notes about the DMRG algorithm for two dimensional systems

The DMRG method was proposed by White [Whi92] in 1992 as an algorithm to study large correlated systems. Although this numerical method was designed for one dimensional lattices, the study two-dimensional systems is also possible with this algorithm, but its results are less accurate with respect to one dimension, and it requires a computational effort which grows exponentially with the width of the system [SW12]. However, the DMRG has been useful in the study of several two-dimensional systems as magnetic models where the power of this method was demonstrated studying frustrated Heisenberg model on CAVO and triangular lattices [Whi96, WC07]. Also, the DMRG algorithm was used to study doped t-J and Hubbard models where it is predicted a d-paring which is one of the phenomena observed in the high T_c cuprate superconductors[Sca01].

Quasi one dimensional map: Ladder Lattice

In order to understand why the computational effort is higher for wide lattices, let us explain how to implement the DMRG algorithm to a two-dimensional lattice through a simple example: a *ladder lattice*. As its name indicates, a ladder lattice is a narrow rectangular lattice which figure resembles to a ladder [see FIGURE 31]; a simple rectangular lattice with a wide of two sites.

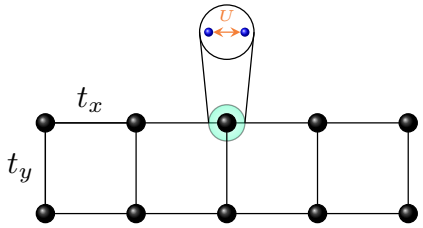

FIGURE 31. Scheme of a ladder lattice with local interactions.

Let us consider a general Hamiltonian for this type of lattice:

$$\hat{H}_{ladder} = t_x \left(\sum_{i,j} \hat{c}^{\dagger}_{i,j} \hat{c}_{i+1,j} + h.c \right) + t_y \left(\sum_{i=1}^{L} \hat{c}^{\dagger}_{i,1} \hat{c}_{i,2} + h.c \right) + \hat{U}, \tag{11}$$

where the operator $\hat{c}^{\dagger}_{i,j}$ ($\hat{c}_{i,j}$) is the creation (annihilation) operator of a particle in a lattice site i, j, with $i = 1, 2, \cdots, L$ and $j = 1, 2$, and $\hat{U}$ is an operator that includes others local or non-local operators such that the two first terms in the Hamiltonian are horizontal and vertical hopping terms, with a hopping amplitude t_x and t_y respectively, and the last term corresponds to a local or non-local interaction in the lattice.

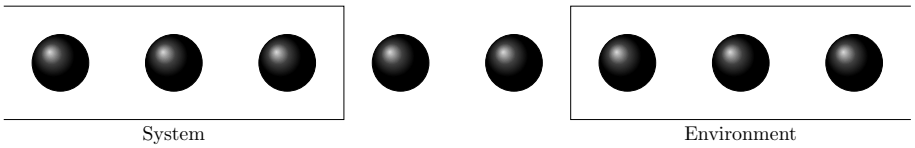

FIGURE 32. Bipartite decomposition of a one dimensional lattice used to calculate the density matrix of whole system in the DMRG algorithm.

Since the principal idea behind the DMRG algorithm is to truncate the Hilbert space by discarding the state with less statistical weight using the density matrix of the system (see FIGURE 32), it is usual to build up the Hamiltonian of a one dimensional lattice through the tensor product of two subspaces operators, sometimes called *system* and *environment* operators. In order to use the DMRG algorithm in the ladder lattice, it is enough to rewrite the ladder Hamiltonian $\hat{H}_{ladder}$ as the following product:

$$\hat{H}_{ladder} = \hat{H}_{sys} \otimes Id_L + Id_L \otimes \hat{H}_{env} + \hat{O}_{sys} \otimes \hat{O}_{env}, \tag{12}$$

being Id_L is the unity matrix of dimension L, $\hat{H}_{sys}$ and $\hat{H}_{env}$ are the Hamiltonian of the system and environment subsystems respectively, and $\hat{O}_{sys}$ and $\hat{O}_{env}$ are operators of the system and environment subsystems receptively. However, this assignment is not unique for any lattice. In the FIGURE 33 is shown two different ways to do such assignment: the map of the ladder into a one dimensional lattice is defined by labeling the sites of the original lattice and the local operators $\hat{O}_i$ are defined according to the edges of the original lattice.

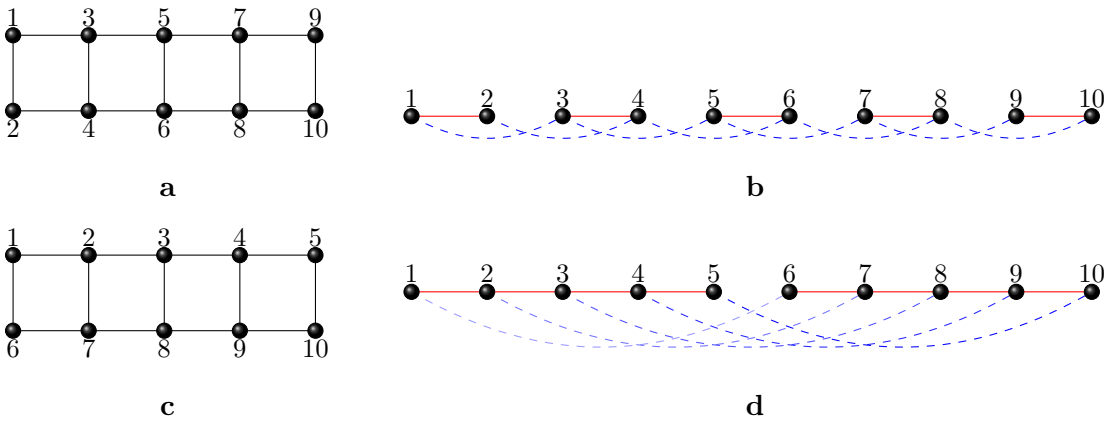

FIGURE 33. Two possible maps of a ladder lattice into an inhomogeneous chain: (**a**)-(**b**) first mapping, (**c**)-(**d**) second mapping.

In both maps of the FIGURE 33, the ladder lattice is mapped into an inhomogeneous chain with a long hopping terms and long interaction between the lattice sites for Hamiltonian with non-local interactions terms. Let us suppose that $\hat{U}$ has only local interaction operators, i.e $\hat{U} = \sum_i \hat{U}_i$. Thus, in the first map (**a**)-(**b**), the ladder Hamiltonian (11) is equivalent to the following Hamiltonian:

$$\hat{H}_{ladder} = \sum_{i=1}^{2L} \left(t_i \hat{c}_i^\dagger \hat{c}_{i+1} + t_x \hat{c}_i^\dagger \hat{c}_{i+2} + h.c \right) + \sum_{i=1}^{2L} \hat{U}_i, \tag{13}$$

where $t_i = t_y$ if and only if $i \equiv 1 \ mod \ 2$ and $t_i = 0$ in otherwise. Thus, in order to write this Hamiltonian in the form (12) we need to define the following operators for each step of the DMRG algorithm:

$$\hat{A}_{sys} = Id_{L-1} \otimes \hat{c}_L^\dagger, \qquad \hat{B}_{sys} = Id_{L-2} \otimes \hat{c}_{L-1}^\dagger \otimes Id_1, \tag{14}$$

$$\hat{A}_{env} = \hat{c}_{L+1} \otimes Id_{L-1}, \qquad \hat{B}_{env} = Id_1 \otimes \hat{c}_{L+2} \otimes Id_{L-2}. \tag{15}$$

Thus, the Hamiltonian $\hat{H}_{ladder}$ is rewrite as

$$\hat{H}_{ladder} = \hat{H}_{sys} \otimes Id_L + Id_L \otimes \hat{H}_{env} + t_L \hat{A}_{sys} \otimes \hat{A}_{env} + t_x \left(\hat{B}_{sys} \otimes \hat{A}_{env} + \hat{A}_{sys} \otimes \hat{B}_{env} \right). \tag{16}$$

The first tree terms in the last equation are usual terms in a one dimensional DMRG algorithm, and the last terms is an extra term due to the assignment. It turns out that this extra term involves a huge product between the system and environment subsystems, which is computationally expensive.

Now let us consider the second map (FIGURE 33-(**c**) and (**d**)). In this case, the ladder Hamiltonian is equivalent to the following Hamiltonian:

$$\hat{H}_{ladder} = \sum_{i=1} \left(t_i \hat{c}_i^\dagger \hat{c}_{i+1} + t_y \hat{c}_i^\dagger \hat{c}_{i+5} + h.c \right) + \sum_{i=1} \hat{U}_i, \tag{17}$$

where $t_i = t_x$ if and only if $i \neq L$ and $t_L = 0$. In contrast with the Hamiltonian of the first map, this one involves a very long hopping terms, hopping to L-th nearest neighbors. In order to write this Hamiltonian as equation (12) we need to define the following operators for each step of the DMRG algorithm:

$$\hat{A}_{sys} = Id_{L-1} \otimes \hat{c}_L^\dagger, \qquad \hat{A}_{env} = \hat{c}_{L+1} \otimes Id_{L-1}, \tag{18}$$

$$\hat{B}_{sys} = Id_{L-2} \otimes \hat{c}_{L-1}^\dagger \otimes Id_1, \qquad \hat{B}_{env} = Id_1 \otimes \hat{c}_{L+2} \otimes Id_{L-2}, \tag{19}$$

$$\hat{C}_{sys} = Id_{L-3} \otimes \hat{c}_{L-2}^\dagger \otimes Id_2, \qquad \hat{C}_{env} = Id_2 \otimes \hat{c}_{L+3} \otimes Id_{L-3}, \tag{20}$$

$$\hat{D}_{sys} = Id_{L-4} \otimes \hat{c}_{L-3}^\dagger \otimes Id_3, \qquad \hat{D}_{env} = Id_3 \otimes \hat{c}_{L+4} \otimes Id_{L-4}, \tag{21}$$

$$\hat{E}_{sys} = Id_{L-5} \otimes \hat{c}_{L-4}^\dagger \otimes Id_4, \qquad \hat{E}_{env} = Id_4 \otimes \hat{c}_{L+5} \otimes Id_{L-5}. \tag{22}$$

Thus, the Hamiltonian is rewritten as follows:

$$\begin{aligned} \hat{H}_2 = \hat{H}_{sys} \otimes Id_L + Id_L \otimes \hat{H}_{env} + t_y \Big(& \hat{E}_{sys} \otimes \hat{A}_{env} + \hat{D}_{sys} \otimes \hat{B}_{env} \\ & \hat{C}_{sys} \otimes \hat{C}_{env} + \hat{B}_{sys} \otimes \hat{D}_{env} + \hat{A}_{sys} \otimes \hat{E}_{env} \Big). \end{aligned} \tag{23}$$

This time five extra appears terms that include a huge product between the system and environment subspaces, which means a high computational effort. We must note that this second map is equivalent to a wide ladder lattice. Therefore, the computational time to work with a wide lattice principally is due to a very long hopping terms cause by the map into a one dimensional lattice.

Bibliography

[AEM+95] M. H. Anderson, J. R. Ensher, M. R. Matthews, C. E. Wieman, and E. A. Cornell. Observation of bose-einstein condensation in a dilute atomic vapor. *Science*, 269(5221):198–201, 1995. X, 6

[AMU75] Tsuneya Ando, Yukio Matsumoto, and Yasutada Uemura. Theory of hall effect in a two-dimensional electron system. *Journal of the Physical Society of Japan*, 39(2):279–288, 1975. 4

[BAR+05] M. Bartenstein, A. Altmeyer, S. Riedl, R. Geursen, S. Jochim, C. Chin, J. Hecker Denschlag, R. Grimm, A. Simoni, E. Tiesinga, C. J. Williams, and P. S. Julienne. Precise determination of ^{6}Li cold collision parameters by radio-frequency spectroscopy on weakly bound molecules. *Phys. Rev. Lett.*, 94:103201, Mar 2005. 11

[BCD+10] L. Barbiero, M. Casadei, M. Dalmonte, C. Degli Esposti Boschi, E. Ercolessi, and F. Ortolani. Phase separation and pairing regimes in the one-dimensional asymmetric hubbard model. *Phys. Rev. B*, 81:224512, Jun 2010. 18

[BCP+18] Vincent Barbé, Alessio Ciamei, Benjamin Pasquiou, Lukas Reichsöllner, Florian Schreck, Piotr S. Zuchowski, and Jeremy M. Hutson. Observation of feshbach resonances between alkali and closed-shell atoms. *Nature Physics*, 14(9):881–884, Sep 2018. 11

[BGK15] Soumen Bag, Arti Garg, and H. R. Krishnamurthy. Phase diagram of the half-filled ionic hubbard model. *Phys. Rev. B*, 91:235108, Jun 2015. 26

[BLSS07] K. Buchta, Ö. Legeza, E. Szirmai, and J. Sólyom. Mott transition and dimerization in the one-dimensional SU(n) hubbard model. *Phys. Rev. B*, 75:155108, Apr 2007. 13

[BM86] J. G. Bednorz and K. A. Muller. Possible high-tc superconductivity in the ba-la-cu-o system. *Zeitschrift ur Physik B Condensed Matter*, 64(2):189–193, Jun 1986. 5

[BPH+07] K. Bouadim, N. Paris, F. Hébert, G. G. Batrouni, and R. T. Scalettar. Metallic phase in the two-dimensional ionic hubbard model. *Phys. Rev. B*, 76:085112, Aug 2007.

[BT16] Peter Broecker and Simon Trebst. Entanglement and the fermion sign problem in auxiliary field quantum monte carlo simulations. *Phys. Rev. B*, 94:075144, Aug 2016.

[CBKG19] Anwesha Chattopadhyay, Soumen Bag, H. R. Krishnamurthy, and Arti Garg. Phase diagram of the half-filled ionic hubbard model in the limit of strong correlations. *Phys. Rev. B*, 99:155127, Apr 2019. X, XI, 26

[CG08] Wen-Ling Chan and Shi-Jian Gu. Entanglement and quantum phase transition in the asymmetric hubbard chain: density-matrix renormalization group calculations. *Journal of Physics: Condensed Matter*, 20(34):345217, aug 2008. 18

[CGJT10] Cheng Chin, Rudolf Grimm, Paul Julienne, and Eite Tiesinga. Feshbach resonances in ultracold gases. *Rev. Mod. Phys.*, 82:1225–1286, Apr 2010. 11

[CHB+85] Steven Chu, L. Hollberg, J. E. Bjorkholm, Alex Cable, and A. Ashkin. Three-dimensional viscous confinement and cooling of atoms by resonance radiation pressure. *Phys. Rev. Lett.*, 55:48–51, Jul 1985.

[CMDCT89] Y. Castin, K. Mφlmer, J. Dalibard, and C. Cohen-Tannoudji. New physical mechanisms in laser cooling. pages 2 – 7, 1989. X, 6

[CP18] Agnieszka Cichy and Andrzej Ptok. Reentrant fulde-ferrell-larkin-ovchinnikov superfluidity in the honeycomb lattice. *Phys. Rev. A*, 97:053619, May 2018. 17

[CPGSV21] J. Ignacio Cirac, David Pérez-García, Norbert Schuch, and Frank Verstraete. Matrix product states and projected entangled pair states: Concepts, symmetries, theorems. *Rev. Mod. Phys.*, 93:045003, Dec 2021. 49

[CWHW08] Shu Chen, Li Wang, Yajiang Hao, and Yupeng Wang. Intrinsic relation between ground-state fidelity and the characterization of a quantum phase transition. *Phys. Rev. A*, 77:032111, Mar 2008. 34

[CZLW10] Hui-Min Chen, Hui Zhao, Hai-Qing Lin, and Chang-Qin Wu. Bond-located spin density wave phase in the two-dimensional (2d) ionic hubbard model. *New Journal of Physics*, 12(9):093021, sep 2010. X, XI, 26

[DCG66] Jacques Des Cloizeaux and Michel Gaudin. Anisotropic linear magnetic chain. *Journal of Mathematical Physics*, 7(8):1384–1400, 1966. 18

[Deh68] H.G. Dehmelt. Radiofrequency spectroscopy of stored ions i: Storage**part ii: Spectroscopy is now scheduled to appear in volume v of this series. 3:53 – 72, 1968. X, 6

[Deh69] H.G. Dehmelt. Radiofrequency spectroscopy of stored ions ii: Spectroscopy**part i, sections 1 and 2 of this article appear in volume 3 of this series. 5:109 – 154, 1969. X, 6

[DiV00] David P. DiVincenzo. The physical implementation of quantum computation. *Fortschritte der Physik*, 48(9-11):771–783, 2000. 10

[DJ99] B. DeMarco and D. S. Jin. Onset of fermi degeneracy in a trapped atomic gas. *Science*, 285(5434):1703–1706, 1999. 11

[Ess10] Tilman Esslinger. Fermi-hubbard physics with atoms in an optical lattice. *Annual Review of Condensed Matter Physics*, 1(1):129–152, 2010.

[Far12] P. Farkašovský. Ferromagnetism in the asymmetric hubbard model. *The European Physical Journal B*, 85(8):253, Jul 2012. 18

[FBI+14] Gianluca Fiori, Francesco Bonaccorso, Giuseppe Iannaccone, Tomás Palacios, Daniel Neumaier, Alan Seabaugh, Sanjay K. Banerjee, and Luigi Colombo. Electronics based on two-dimensional materials. *Nature Nanotechnology*, 9(10):768–779, Oct 2014. 13

[Fcv08] Pavol Farkašovský. Phase diagram of the asymmetric hubbard model. *Phys. Rev. B*, 77:085110, Feb 2008. 18

[FDanLan95] Gábor Fáth, Zbigniew Domański, and Romuald Lemański. Asymmetric hubbard chain at half-filling. *Phys. Rev. B*, 52:13910–13915, Nov 1995. 18

[FF64] Peter Fulde and Richard A. Ferrell. Superconductivity in a strong spin-exchange field. *Phys. Rev.*, 135:A550–A563, Aug 1964. 17

[FG04] Serge Florens and Antoine Georges. Slave-rotor mean-field theories of strongly correlated systems and the mott transition in finite dimensions. *Phys. Rev. B*, 70:035114, Jul 2004.

[FGKS05] J. N. Fuchs, D. M. Gangardt, T. Keilmann, and G. V. Shlyapnikov. Spin waves in a one-dimensional spinor bose gas. *Phys. Rev. Lett.*, 95:150402, Oct 2005. X

[FGN99] Michele Fabrizio, Alexander O. Gogolin, and Alexander A. Nersesyan. From band insulator to mott insulator in one dimension. *Phys. Rev. Lett.*, 83:2014–2017, Sep 1999. VI, XI, 22, 24

[FK69] L. M. Falicov and J. C. Kimball. Simple model for semiconductor-metal transitions: Smb_6 and transition-metal oxides. *Phys. Rev. Lett.*, 22:997–999, May 1969. 17

[FMH+10] Hélène Feldner, Zi Yang Meng, Andreas Honecker, Daniel Cabra, Stefan Wessel, and Fakher F. Assaad. Magnetism of finite graphene samples: Mean-field theory compared with exact diagonalization and quantum monte carlo simulations. *Phys. Rev. B*, 81:115416, Mar 2010.

[FR08] J. Fernández-Rossier. Prediction of hidden multiferroic order in graphene zigzag ribbons. *Phys. Rev. B*, 77:075430, Feb 2008.

[FWGF89] Matthew P. A. Fisher, Peter B. Weichman, G. Grinstein, and Daniel S. Fisher. Boson localization and the superfluid-insulator transition. *Phys. Rev. B*, 40:546–570, Jul 1989. 9

[FWNK96a] Mitsutaka Fujita, Katsunori Wakabayashi, Kyoko Nakada, and Koichi Kusakabe. Peculiar localized state at zigzag graphite edge. *Journal of the Physical Society of Japan*, 65(7):1920–1923, 1996.

[FWNK96b] Mitsutaka Fujita, Katsunori Wakabayashi, Kyoko Nakada, and Koichi Kusakabe. Peculiar localized state at zigzag graphite edge. *Journal of the Physical Society of Japan*, 65(7):1920–1923, 1996.

[FWS20] Matthew Fishman, Steven R. White, and E. Miles Stoudenmire. The ITensor software library for tensor network calculations, 2020. 29

[GFW+06] Fabrice Gerbier, Simon Fölling, Artur Widera, Olaf Mandel, and Immanuel Bloch. Probing number squeezing of ultracold atoms across the superfluid-mott insulator transition. *Phys. Rev. Lett.*, 96:090401, Mar 2006. 12

[GIJL90] C. Gruber, J. Iwanski, J. Jedrzejewski, and P. Lemberger. Ground states of the spinless falicov-kimball model. *Phys. Rev. B*, 41:2198–2209, Feb 1990. 17

[GKR06] Arti Garg, H. R. Krishnamurthy, and Mohit Randeria. Can correlations drive a band insulator metallic? *Phys. Rev. Lett.*, 97:046403, Jul 2006. X, 26

[GKR14] Arti Garg, H. R. Krishnamurthy, and Mohit Randeria. Doping a correlated band insulator: A new route to half-metallic behavior. *Phys. Rev. Lett.*, 112:106406, Mar 2014. X

[GLST+20] Alaina Green, Hui Li, Jun Hui See Toh, Xinxin Tang, Katherine C. McCormick, Ming Li, Eite Tiesinga, Svetlana Kotochigova, and Subhadeep Gupta. Feshbach resonances in p-wave three-body recombination within fermi-fermi mixtures of open-shell ^{6}Li and closed-shell ^{173}Yb atoms. *Phys. Rev. X*, 10:031037, Aug 2020. 11

[GMJ16] I. Grusha, M. Menteshashvili, and G. I. Japaridze. Effective hamiltonian for a half-filled asymmetric ionic hubbard chain with alternating on-site interaction. *International Journal of Modern Physics B*, 30(03):1550260, 2016. 18, 23, 28

[Gre02] Mandel O. Esslinger T. et al. Greiner, M. Quantum phase transition from a superfluid to a mott insulator in a gas of ultracold atoms. *Nature.*, 415:39–44, Jan 2002. V, X, 9, 10

[GU10] SHI-JIAN GU. Fidelity approach to quantum phase transitions. *International Journal of Modern Physics B*, 24(23):4371–4458, 2010. 34

[GUJ+13] Daniel Greif, Thomas Uehlinger, Gregor Jotzu, Leticia Tarruell, and Tilman Esslinger. Short-range quantum magnetism of ultracold fermions in an optical lattice. *Science*, 340(6138):1307–1310, 2013. 18

[GWO00] Rudolf Grimm, Matthias Weidemuller, and Yurii B. Ovchinnikov. Optical dipole traps for neutral atoms. volume 42 of *Advances In Atomic, Molecular, and Optical Physics*, pages 95 – 170. Academic Press, 2000. X, 6

[HF64a] J. Hubbard and Brian Hilton Flowers. Electron correlations in narrow energy bands. ii. the degenerate band case. *Proceedings of the Royal Society of London. Series A. Mathematical and Physical Sciences*, 277(1369):237–259, 1964. 4

[HF64b] J. Hubbard and Brian Hilton Flowers. Electron correlations in narrow energy bands iii. an improved solution. *Proceedings of the Royal Society of London. Series A. Mathematical and Physical Sciences*, 281(1386):401–419, 1964. 4

[HHLM03] Toshiya Hikihara, Xiao Hu, Hsiu-Hau Lin, and Chung-Yu Mou. Ground-state properties of nanographite systems with zigzag edges. *Phys. Rev. B*, 68:035432, Jul 2003. VI, 15, 16, 48

[Hid92] Kazuo Hida. Crossover between the haldane-gap phase and the dimer phase in the spin-1/2 alternating heisenberg chain. *Phys. Rev. B*, 45:2207–2212, Feb 1992. 5

[HKGF14] Wei Han, Roland K. Kawakami, Martin Gmitra, and Jaroslav Fabian. Graphene spintronics. *Nature Nanotechnology*, 9(10):794–807, Oct 2014. 13, 16

[HL27] W. Heitler and F. London. Wechselwirkung neutraler atome und homöopolare bindung nach der quantenmechanik. *Zeitschrift für Physik*, 44(6):455–472, Jun 1927. 1

[HL16] I. Hagymási and Ö. Legeza. Entanglement, excitations, and correlation effects in narrow zigzag graphene nanoribbons. *Phys. Rev. B*, 94:165147, Oct 2016. VI, 15, 39, 48

[Hoa10] A T Hoang. Metal-insulator transitions in the half-filled ionic hubbard model. *Journal of Physics: Condensed Matter*, 22(9):095602, 2010.

[HSS71] T. W. Hänsch, I. S. Shahin, and A. L. Schawlow. High-resolution saturation spectroscopy of the sodium d lines with a pulsed tunable dye laser. *Phys. Rev. Lett.*, 27:707–710, Sep 1971. X, 6

[HT81] J. Hubbard and J. B. Torrance. Model of the neutral-ionic phase transformation. *Phys. Rev. Lett.*, 47:1750–1754, Dec 1981.

[hub63] Electron correlations in narrow energy bands. *Proceedings of the Royal Society of London A: Mathematical, Physical and Engineering Sciences*, 276(1365):238–257, 1963. 2

[HY57] Kerson Huang and C. N. Yang. Quantum-mechanical many-body problem with hard-sphere interaction. *Phys. Rev.*, 105:767–775, Feb 1957. 8

[IFT98] Masatoshi Imada, Atsushi Fujimori, and Yoshinori Tokura. Metal-insulator transitions. *Rev. Mod. Phys.*, 70:1039–1263, Oct 1998. IV, V, 4, 5, 6

[IGO+04] S. Inouye, J. Goldwin, M. L. Olsen, C. Ticknor, J. L. Bohn, and D. S. Jin. Observation of heteronuclear feshbach resonances in a mixture of bosons and fermions. *Phys. Rev. Lett.*, 93:183201, Oct 2004. 11

[JBC+98] D. Jaksch, C. Bruder, J. I. Cirac, C. W. Gardiner, and P. Zoller. Cold bosonic atoms in optical lattices. *Phys. Rev. Lett.*, 81:3108–3111, Oct 1998. X, 8

[JBC+99] D. Jaksch, H.J. Briegel, J. I. Cirac, C. W. Gardiner, and P. Zoller. Entanglement of atoms via cold controlled collisions. *Phys. Rev. Lett.*, 82:1975–1978, Mar 1999. 9

[JFG+09] Y. Jompol, C. J. B. Ford, J. P. Griffiths, I. Farrer, G. A. C. Jones, D. Anderson, D. A. Ritchie, T. W. Silk, and A. J. Schofield. Probing spin-charge separation in a tomonaga-luttinger liquid. *Science*, 325(5940):597–601, 2009. X

[JrSGn+08] Robert Jö rdens, Niels Strohmaier, Kenneth Gü nter, Henning Moritz, and Tilman Esslinger. A mott insulator of fermionic atoms in an optical lattice. *Nature*, 455(7210):204–207, Sep 2008. V, 10, 12, 13, 25

[JZC+14] Michael Jag, Matteo Zaccanti, Marko Cetina, Rianne S. Lous, Florian Schreck, Rudolf Grimm, Dmitry S. Petrov, and Jesper Levinsen. Observation of a strong atom-dimer attraction in a mass-imbalanced fermi-fermi mixture. *Phys. Rev. Lett.*, 112:075302, Feb 2014. 17

[Kar13] Naoum Karchev. Quantum critical behavior in three-dimensional one-band hubbard model at half-filling. *Annals of Physics*, 333:206–220, 2013. 13

[KD07] S. S. Kancharla and E. Dagotto. Correlated insulated phase suggests bond order between band and mott insulators in two dimensions. *Phys. Rev. Lett.*, 98:016402, Jan 2007. X, XI, 26

[KES+96] M. A. Korotin, S. Yu. Ezhov, I. V. Solovyev, V. I. Anisimov, D. I. Khomskii, and G. A. Sawatzky. Intermediate-spin state and properties of $lacoo_3$. *Phys. Rev. B*, 54:5309–5316, Aug 1996. 6

[KHI+09] Akihisa Koga, Takuji Higashiyama, Kensuke Inaba, Seiichiro Suga, and Norio Kawakami. Supersolid state in fermionic optical lattice systems. *Phys. Rev. A*, 79:013607, Jan 2009. X

[KI93] Nobuyuki Katoh and Masatoshi Imada. Phase diagram of s=1/2 antiferromagnetic heisenberg model on a dimerized square lattice. *Journal of the Physical Society of Japan*, 62(10):3728–3740, 1993. 5

[KI94] Nobuyuki Katoh and Masatoshi Imada. Phase diagram of s=1/2 quasi-one-dimensional heisenberg model with dimerized antiferromagnetic exchange. *Journal of the Physical Society of Japan*, 63(12):4529–4541, 1994. 5

[KL86] Tom Kennedy and Elliott H. Lieb. An itinerant electron model with crystalline or magnetic long range order. *Physica A: Statistical Mechanics and its Applications*, 138(1):320–358, 1986. 17

[KMM64] J. I. Krugler, C. G. Montgomery, and H. M. McConnell. Collective electronic states in molecular crystals. *The Journal of Chemical Physics*, 41(8):2421–2428, 1964. 22

[KSK96] Masatsune Kato, Kazunori Shiota, and Yoji Koike. Metal-insulator transition and spin gap in the spin-1/2 ladder system $sr_{14-x}a_xcu_{24}o_{41}$ (a: Ba and ca). *Physica C: Superconductivity*, 258(3):284–292, 1996. 5

[KTK98] Atsushi Kawamoto, Hiromi Taniguchi, and Kazushi Kanoda. Superconductor-insulator transition controlled by partial deuteration in bedt-ttf salt. *Journal of the American Chemical Society*, 120(42):10984–10985, Oct 1998. 6

[Leg98] A. J. Leggett. On the superfluid fraction of an arbitrary many-body system at t=0. *Journal of Statistical Physics*, 93(3):927–941, Nov 1998. 9

[Leo81] V. Leo. Elastic electron tunneling study of the metal-insulator transition in ttf-tcnq. *Solid State Communications*, 40(4):509–511, 1981. 5

[LGCS15] Tianhe Li, Huaiming Guo, Shu Chen, and Shun-Qing Shen. Complete phase diagram and topological properties of interacting bosons in one-dimensional superlattices. *Phys. Rev. B*, 91:134101, Apr 2015.

[Lie89] Elliott H. Lieb. Two theorems on the hubbard model. *Phys. Rev. Lett.*, 62:1201–1204, Mar 1989. 16

[LL59] L. D. Landau and E. M. Lifshitz. Chapter xvii - the theory of elastic collisions. In *Course of Theoretical Physics Vol 3: Quantum Mechanics*, pages 469 – 535. Pergamon Press, Oxford, 1959. 8

[LLTL15] Heng-Fu Lin, Hai-Di Liu, Hong-Shuai Tao, and Wu-Ming Liu. Phase transitions of the ionic hubbard model on the honeycomb lattice. *Scientific Reports*, 5(1):9810, May 2015. VII, XI, 26, 27, 48

[LM62] Elliott Lieb and Daniel Mattis. Theory of ferromagnetism and the ordering of electronic energy levels. *Phys. Rev.*, 125:164–172, Jan 1962. 5

[LO64] A. I. Larkin and Y. N. Ovchinnikov. Nonuniform state of superconductors. *Zh. Eksp. Teor. Fiz.*, 47:1136–1146, 1964. 17

[LRT+02] T. Loftus, C. A. Regal, C. Ticknor, J. L. Bohn, and D. S. Jin. Resonant control of elastic collisions in an optically trapped fermi gas of atoms. *Phys. Rev. Lett.*, 88:173201, Apr 2002. V, 10, 11

[LW68] Elliott H. Lieb and F. Y. Wu. Absence of mott transition in an exact solution of the short-range, one-band model in one dimension. *Phys. Rev. Lett.*, 20:1445–1448, Jun 1968. 5

[LW15] Ye-Hua Liu and Lei Wang. Quantum monte carlo study of mass-imbalanced hubbard models. *Phys. Rev. B*, 92:235129, Dec 2015.

[MAFSV10] J. J. Mendoza-Arenas, R. Franco, and J. Silva-Valencia. Block entropy and quantum phase transition in the anisotropic kondo necklace model. *Phys. Rev. A*, 81:062310, Jun 2010. 45

[Mat07] L. Mathey. Commensurate mixtures of ultracold atoms in one dimension. *Phys. Rev. B*, 75:144510, Apr 2007. 18

[MBG69] A. Menth, E. Buehler, and T. H. Geballe. Magnetic and semiconducting properties of smb_6. *Phys. Rev. Lett.*, 22:295–297, Feb 1969. 17

[MCFSV16] L S Murcia-Correa, R Franco, and J Silva-Valencia. Quantum phases of ab 2 fermionic chains. *Journal of Physics: Conference Series*, 687(1):012066, 2016. 22

[MCH93] J. D. Miller, R. A. Cline, and D. J. Heinzen. Far-off-resonance optical trapping of atoms. *Phys. Rev. A*, 47:R4567–R4570, Jun 1993. 8

[MDU+15] Michael Messer, Rémi Desbuquois, Thomas Uehlinger, Gregor Jotzu, Sebastian Huber, Daniel Greif, and Tilman Esslinger. Exploring competing density order in the ionic hubbard model with ultracold fermions. *Phys. Rev. Lett.*, 115:115303, Sep 2015. VI, XI, 25, 26

[MDW92] J. W. Mintmire, B. I. Dunlap, and C. T. White. Are fullerene tubules metallic? *Phys. Rev. Lett.*, 68:631–634, Feb 1992.

[ME12] S. Moukouri and E. Eidelstein. Universality class of the mott transition in two dimensions. *Phys. Rev. B*, 86:155112, Oct 2012. 13

[Mis12] Prasanta K. Misra. Chapter 13 - magnetic ordering. In Prasanta K. Misra, editor, *Physics of Condensed Matter*, pages 409 – 449. Academic Press, Boston, 2012. 1

[MJH+14] Gábor Zsolt Magda, Xiaozhan Jin, Imre Hagymási, Péter Vancsó, Zoltán Osváth, Péter Nemes-Incze, Chanyong Hwang, László P. Biró, and Levente Tapasztó. Room-temperature magnetic order on zigzag edges of narrow graphene nanoribbons. *Nature*, 514(7524):608–611, Oct 2014. V, VI, 14, 15

[MMF+18] David Mele, Sarah Mehdhbi, Dalal Fadil, Wei Wei, Abdelkarim Ouerghi, Sylvie Lepilliet, Henri Happy, and Emiliano Pallecchi. Graphene fets based on high resolution nanoribbons for hf low power applications. *Electronic Materials Letters*, 14(2):133–138, Mar 2018. 13

[MMNS04] S. R. Manmana, V. Meden, R. M. Noack, and K. Schönhammer. Quantum critical behavior of the one-dimensional ionic hubbard model. *Phys. Rev. B*, 70:155115, Oct 2004. VI, XI, 22, 23, 24, 32

[Mot49] N F Mott. The basis of the electron theory of metals, with special reference to the transition metals. *Proceedings of the Physical Society. Section A*, 62(7):416–422, jul 1949. 1, 4

[Mot56] N. F. Mott. On the transition to metallic conduction in semiconductors. *Canadian Journal of Physics*, 34(12A):1356–1368, 1956. 4

[Mot61] N. F. Mott. The transition to the metallic state. *The Philosophical Magazine: A Journal of Theoretical Experimental and Applied Physics*, 6(62):287–309, 1961. 4

[Mot90] N F Mott. Metal-insulator transitions. CRC Press, London, 1990. 5

[MP37] N F Mott and R Peierls. Discussion of the paper by de boer and verwey. *Proceedings of the Physical Society*, 49(4S):72–73, aug 1937.

[MRPM+20] Alberto Medina-Rull, Francisco Pasadas, Enrique G. Marin, Alejandro Toral-Lopez, Juan Cuesta, Andres Godoy, David JimÃ©lnez, and Francisco G. Ruiz. A graphene field-effect transistor based analogue phase shifter for high-frequency applications. *IEEE Access*, 8:209055–209063, 2020. 13

[MRR+71] D. B. McWhan, J. P. Remeika, T. M. Rice, W. F. Brinkman, J. P. Maita, and A. Menth. Electronic specific heat of metallic ti-doped v_2o_3. *Phys. Rev. Lett.*, 27:941–943, Oct 1971. 5

[MTS+00] Shigeki Miyasaka, Hidenori Takagi, Yoshiaki Sekine, Hiroki Takahashi, Nobuo Mouri, and Robert J. Cava. Metal-insulator transition and itinerant antiferromagnetism in $nis_{2-x}se_x$ pyrite. *Journal of the Physical Society of Japan*, 69(10):3166–3169, 2000. 5

[Mul54] R. S. Mulliken. Intermolecular charge-transfer forces. *Rendiconti del Seminario Matematico e Fisico di Milano*, 24(1):183–189, Dec 1954. 19

[NGM+04] K. S. Novoselov, A. K. Geim, S. V. Morozov, D. Jiang, Y. Zhang, S. V. Dubonos, I. V. Grigorieva, and A. A. Firsov. Electric field effect in atomically thin carbon films. *Science*, 306(5696):666–669, 2004. 13

[NiT86] Naoto Nagaosa and Jun ichi Takimoto. Theory of neutral-ionic transition in organic crystals. i. monte carlo simulation of modified hubbard model. *Journal of the Physical Society of Japan*, 55(8):2735–2744, 1986.

[NSM66] P L Nordio, Z G Soos, and H M McConnell. Spin excitations in ionic molecular crystals. *Annual Review of Physical Chemistry*, 17(1):237–260, 1966. 21

[NYKS96] Takashi Nishikawa, Yukio Yasui, Yoshiaki Kobayashi, and Masatoshi Sato. Thermal properties of two dimensional mott system $la_{1.17-x}sr_xvs_{3.17}$. *Journal of the Physical Society of Japan*, 65(8):2543–2547, 1996. 6

[OGRL72] D. D. Osheroff, W. J. Gully, R. C. Richardson, and D. M. Lee. New magnetic phenomena in liquid He^3 below 3 mk. *Phys. Rev. Lett.*, 29:920–923, Oct 1972. X

[ON02] Tobias J. Osborne and Michael A. Nielsen. Entanglement in a simple quantum phase transition. *Phys. Rev. A*, 66:032110, Sep 2002. 45

[OPS08] G. Orso, L. P. Pitaevskii, and S. Stringari. Equilibrium and dynamics of a trapped superfluid fermi gas with unequal masses. *Phys. Rev. A*, 77:033611, Mar 2008. 17

[ORL72] D. D. Osheroff, R. C. Richardson, and D. M. Lee. Evidence for a new phase of solid He^3. *Phys. Rev. Lett.*, 28:885–888, Apr 1972. X

[PBH+07] N. Paris, K. Bouadim, F. Hebert, G. G. Batrouni, and R. T. Scalettar. Quantum monte carlo study of an interaction-driven band-insulator–to–metal transition. *Phys. Rev. Lett.*, 98:046403, Jan 2007. XI, 26

[PGFSV21] D. C. Padilla-GonzÃ¡lez, R. Franco, and J. Silva-Valencia. Mass imbalance in the ionic hubbard model: a drmg study, 2021. VII, VIII, IX, 27, 43, 44, 45, 46

[PH16a] Diana Prychynenko and Sebastian D. Huber. Z2 slave-spin theory of a strongly correlated chern insulator. *Physica B: Condensed Matter*, 481:53 – 58, 2016. X

[PH16b] Diana Prychynenko and Sebastian D. Huber. Z2 slave-spin theory of a strongly correlated chern insulator. *Physica B: Condensed Matter*, 481:53 – 58, 2016.

[Pin53] David Pines. A collective description of electron interactions: Iv. electron interaction in metals. *Phys. Rev.*, 92:626–636, Nov 1953. 1

[PTHAH15] Francesco Parisen Toldin, Martin Hohenadler, Fakher F. Assaad, and Igor F. Herbut. Fermionic quantum criticality in honeycomb and π-flux hubbard models: Finite-size scaling of renormalization-group-invariant observables from quantum monte carlo. *Phys. Rev. B*, 91:165108, Apr 2015. 13

[QBXFQ+08] Wang Qing-Bo, Xu Xiang-Fan, Tao Qian, Wang Hong-Tao, and Xu Zhu-An. Metal—insulator transition in ca-doped sr 14-x ca x cu 24 o 41 systems probed by thermopower measurements. *Chinese Physics Letters*, 25(5):1857–1860, may 2008. 5

[RPC+87] E. L. Raab, M. Prentiss, Alex Cable, Steven Chu, and D. E. Pritchard. Trapping of neutral sodium atoms with radiation pressure. *Phys. Rev. Lett.*, 59:2631–2634, Dec 1987. 7

[RVPS15] Rinaldo Raccichini, Alberto Varzi, Stefano Passerini, and Bruno Scrosati. The role of graphene for electrochemical energy storage. *Nature Materials*, 14(3):271–279, Mar 2015. 13

[SBFB57] K. Sawada, K. A. Brueckner, N. Fukuda, and R. Brout. Correlation energy of an electron gas at high density: Plasma oscillations. *Phys. Rev.*, 108:507–514, Nov 1957. 1

[SBJJ17] Michael Sekania, Dionys Baeriswyl, Luka Jibuti, and George I. Japaridze. Mass-imbalanced ionic hubbard chain. *Phys. Rev. B*, 96:035116, Jul 2017. VII, IX, XI, 28, 29, 46

[Sca01] White S.R. Scalapino, D.J. Numerical results for the hubbard model: Implications for the high tc pairing mechanism. *Foundations of Physics.*, 31:27, Jan 2001. 50

[SCH12] Andrii Sotnikov, Daniel Cocks, and Walter Hofstetter. Advantages of mass-imbalanced ultracold fermionic mixtures for approaching quantum magnetism in optical lattices. *Phys. Rev. Lett.*, 109:065301, Aug 2012. 18

[SCL06a] Young-Woo Son, Marvin L. Cohen, and Steven G. Louie. Energy gaps in graphene nanoribbons. *Phys. Rev. Lett.*, 97:216803, Nov 2006.

[SCL06b] Young-Woo Son, Marvin L. Cohen, and Steven G. Louie. Energy gaps in graphene nanoribbons. *Phys. Rev. Lett.*, 97:216803, Nov 2006.

[SE19a] Ahmad Shahbazy and Morad Ebrahimkhas. Quantum phase transitions in the two dimensional ionic-hubbard model. *Chinese Journal of Physics*, 58:273 – 279, 2019. X

[SE19b] Ahmad Shahbazy and Morad Ebrahimkhas. Quantum phase transitions in the two dimensional ionic-hubbard model. *Chinese Journal of Physics*, 58:273–279, 2019. XI, 26

[Sen08] T. Senthil. Theory of a continuous mott transition in two dimensions. *Phys. Rev. B*, 78:045109, Jul 2008. 13

[Soo74] Z G Soos. Theory of π-molecular charge-transfer crystals. *Annual Review of Physical Chemistry*, 25(1):121–153, 1974. 19, 21

[SS49] C. G. Shull and J. Samuel Smart. Detection of antiferromagnetism by neutron diffraction. *Phys. Rev.*, 76:1256–1257, Oct 1949. X

[SS70] Paul J. Strebel and Zoltán G. Soos. Theory of charge transfer in aromatic donor-acceptor crystals. *The Journal of Chemical Physics*, 53(10):4077–4090, 1970. 19, 21, 22

[SSH79] W. P. Su, J. R. Schrieffer, and A. J. Heeger. Solitons in polyacetylene. *Phys. Rev. Lett.*, 42:1698–1701, Jun 1979.

[STN+09] F. M. Spiegelhalder, A. Trenkwalder, D. Naik, G. Hendl, F. Schreck, and R. Grimm. Collisional stability of $^{40}\mathbf{K}$ immersed in a strongly interacting fermi gas of ^{6}Li. *Phys. Rev. Lett.*, 103:223203, Nov 2009. 17

[SVFF07] J. Silva-Valencia, R. Franco, and M.S. Figueira. The one-dimensional asymmetric hubbard model at partial band filling. *Physica B: Condensed Matter*, 398(2):427–429, 2007. 18

[SW12] E.M. Stoudenmire and Steven R. White. Studying two-dimensional systems with the density matrix renormalization group. *Annual Review of Condensed Matter Physics*, 3(1):111–128, 2012. XI, 50

[SWM] C G Shull, E O Wollan, and M C Marney. Neutron diffraction studies. X, 6

[TAJN06] M. E. Torio, A. A. Aligia, G. I. Japaridze, and B. Normand. Quantum phase diagram of the generalized ionic hubbard model for abn chains. *Phys. Rev. B*, 73:115109, Mar 2006. XI, 22

[TDLB08] Levente Tapasztó, Gergely Dobrik, Philippe Lambin, and László P. Biró. Tailoring the atomic structure of graphene nanoribbons by scanning tunnelling microscope lithography. *Nature Nanotechnology*, 3(7):397–401, Jul 2008. 14

[TGL+10] T. G. Tiecke, M. R. Goosen, A. Ludewig, S. D. Gensemer, S. Kraft, S. J. J. M. F. Kokkelmans, and J. T. M. Walraven. Broad feshbach resonance in the ^{6}Li$-^{40}\mathbf{K}$ mixture. *Phys. Rev. Lett.*, 104:053202, Feb 2010. 17

[TGU+12] Leticia Tarruell, Daniel Greif, Thomas Uehlinger, Gregor Jotzu, and Tilman Esslinger. Creating, moving and merging dirac points with a fermi gas in a tunable honeycomb lattice. *Nature*, 483(7389):302–305, Mar 2012. VI, X, 16, 25

[TLN+92] J. B. Torrance, P. Lacorre, A. I. Nazzal, E. J. Ansaldo, and Ch. Niedermayer. Systematic study of insulator-metal transitions in perovskites rnio_3 (r=pr,nd,sm,eu) due to closing of charge-transfer gap. *Phys. Rev. B*, 45:8209–8212, Apr 1992. 6

[TU08] Masaki Tezuka and Masahito Ueda. Density-matrix renormalization group study of trapped imbalanced fermi condensates. *Phys. Rev. Lett.*, 100:110403, Mar 2008. 17

[TVA+08] M. Taglieber, A.-C. Voigt, T. Aoki, T. W. Hänsch, and K. Dieckmann. Quantum degenerate two-species fermi-fermi mixture coexisting with a bose-einstein condensate. *Phys. Rev. Lett.*, 100:010401, Jan 2008. 17

[TVML81] J. B. Torrance, J. E. Vazquez, J. J. Mayerle, and V. Y. Lee. Discovery of a neutral-to-ionic phase transition in organic materials. *Phys. Rev. Lett.*, 46:253–257, Jan 1981. 20

[VLRK03] G. Vidal, J. I. Latorre, E. Rico, and A. Kitaev. Entanglement in quantum critical phenomena. *Phys. Rev. Lett.*, 90:227902, Jun 2003. 45

[WA96] Steven R. White and Ian Affleck. Dimerization and incommensurate spiral spin correlations in the zigzag spin chain: Analogies to the kondo lattice. *Phys. Rev. B*, 54:9862–9869, Oct 1996. 24

[Wal93] H. Walther. Phase transitions of stored laser-cooled ions. volume 31 of *Advances In Atomic, Molecular, and Optical Physics*, pages 137–182. Academic Press, 1993. 6

[WC07] Steven R. White and A. L. Chernyshev. Neél order in square and triangular lattice heisenberg models. *Phys. Rev. Lett.*, 99:127004, Sep 2007. 50

[WD31] Alan Herries Wilson and Paul Adrien Maurice Dirac. The theory of electronic semi-conductors. *Proceedings of the Royal Society of London. Series A, Containing Papers of a Mathematical and Physical Character*, 133(822):458–491, 1931. 1

[Whi92] Steven R. White. Density matrix formulation for quantum renormalization groups. *Phys. Rev. Lett.*, 69:2863–2866, Nov 1992. 50

[Whi96] Steven R. White. Spin gaps in a frustrated heisenberg model for cav_4O_9. *Phys. Rev. Lett.*, 77:3633–3636, Oct 1996. 50

[WI13] Tsutomu Watanabe and Sumio Ishihara. Band and mott insulators and superconductivity in honeycomb-lattice ionic-hubbard model. *Journal of the Physical Society of Japan*, 82(3):034704, 2013. X

[Wil92] Venema L. Rinzler A. et al. Wilder, J. Electronic structure of atomically resolved carbon nanotubes. *Nature.*, 391:52–62, Jan 1992.

[WS13] Patrick Windpassinger and Klaus Sengstock. Engineering novel optical lattices. *Reports on Progress in Physics*, 76(8):086401, jul 2013. 6, 7

[XWX+14] Fengnian Xia, Han Wang, Di Xiao, Madan Dubey, and Ashwin Ramasubramaniam. Two-dimensional material nanophotonics. *Nature Photonics*, 8(12):899–907, Dec 2014. 13

[YPS+07] Li Yang, Cheol-Hwan Park, Young-Woo Son, Marvin L. Cohen, and Steven G. Louie. Quasiparticle energies and band gaps in graphene nanoribbons. *Phys. Rev. Lett.*, 99:186801, Nov 2007.

[ZPac06] Paolo Zanardi and Nikola Paunković. Ground state overlap and quantum phase transitions. *Phys. Rev. E*, 74:031123, Sep 2006. 34